

## **Response to the referee comments on the manuscript:**

Title: Developing and bounding ice particle mass- and area-dimension expressions for use in atmospheric models and remote sensing

By: Erfani, Ehsan; Mitchell, David

Article reference: acp-2015-739

We wish to thank the referees for their detailed and helpful comments on our paper. As you will see below we have responded to all of the comments with revisions designed to address the concerns of the referees. In the following response, the original referee comments appear in black and our responses appear in blue and are labeled “Author response:”

### **Referee comments:**

#### **Anonymous Referee #1:**

Review of “Developing and bounding ice particle mass- and area-dimension expressions for use in atmospheric models and remote sensing” by Erfani and Mitchell

Recommendation: Accept after revision of manuscript.

This paper presents self-consistent ice particle mass and projected-area dimension relationships that are not power laws, but that can be easily reduced to power laws, that are valid over a much larger range of  $D$  than are power laws. This is done through analysis of data collected by a 2-dimensional stereo probe and Cloud Particle Imager in synoptic and anvil clouds at similar temperatures, and it is shown that the developed relationships are in good agreement with  $m$ - $D$  power laws developed from recent field studies. The unique contribution of this paper is that it develops  $m$ - $D$  and  $A$ - $D$  relations that aren't power laws that cover larger ranges of particle sizes. Further, for implementation in schemes that require such power laws, the formalism can be converted to power law. As such, I feel that this paper is worthy and should be published in ACP subject to the suggested modifications below.

In terms of an historical perspective on the development of power laws, the authors reference the papers by Mitchell (1996, 2000, 2002) and Mitchell et al. (2006), and later on a series of papers by Heymsfield et al. (2004, 2007, 2010). It is important to note that many groups in addition to that of Mitchell and Heymsfield have been involved in the development of such power laws, and a more balanced list of references should be provided (e.g., Fontaine et al. 2014). It is also important to note that authors have derived power law relationships from measurements of bulk reflectivity in addition to measurements of bulk total mass (e.g., McFarquhar et al. 2007, MWR, and Locatelli and Hobbs 1974 should be referenced more early on in paper). I recommend that such studies also be referenced.

**Author response:** Thank you for introducing those papers. All of them are added to the introduction section of manuscript. Now the Introduction starts as (original manuscript, page 28518, after line 17):

“Measurements of individual ice particle mass showed that the relationships between ice particle mass and maximum dimension have the form of habit-dependent power laws (Locatelli and Hobbs, 1974; Mitchell et al., 1990; hereafter M1990). ...”

And another part of Introduction has been modified (original manuscript, page 28519, after line 17):

“...Also, McFarquhar et al. (2007) used PSDs and radar reflectivities measured during spiral descents in the stratiform regions of mesoscale convective systems to determine the power law for each spiral. In addition, the recent study by Fontaine et al. (2014) employed ice particle images and radar reflectivities to derive the temperature-dependent power exponent and prefactor of power laws for tropical anvil clouds. ...”

Why are the results from the Sierra Cooperative Pilot Project used to assess the aircraft results. Since these observations were obtained before the advent of the antishattering tips, there could be some contamination in the results. But, as Jackson and McFarquhar (2014) showed the shattering does not make a significant contribution to the mass measured by the probe, so perhaps the use of the SCPP data are ok. In any event, it would be good to have some discussions somewhere in the paper about the uncertainties associated with the probe measurements, and why those uncertainties do not affect the principal conclusions of the study.

Author response: The reason for using SCPP data is that it includes the direct measurements of individual ice particle mass. In Mitchell et al. (1990), ice particles were collected in the field during winter storms in a petri dish and then imaged under a microscope equipped with a camera. The maximum dimension of each ice particle was later measured in the lab. In addition, each ice particle was melted with a heat-lamp under the microscope, with a corresponding photo taken immediately after melting. This resulted in hemispheric water drops that were imaged in the lab to measure the diameter of the hemispheres and from that the volume and mass of each ice particle was calculated. Shattering can affect the aircraft measurements of ice particles due to aircraft high speed, but it has no significant effect on the ground-based measurements (including SCPP). Moreover, the smallest size that is measured during SCPP (~ 150  $\mu\text{m}$ ) is considerably larger than the size range associated with shattered ice artifacts ( $D < 50 \mu\text{m}$ ; Jackson et al., 2012). It is in this sense that there is no uncertainty due to shattering for the SCPP measurement. All these explanations are added to the manuscript in Sect. 2.2 (original manuscript, page 28522, starting at line 24):

“SCPP was a 3-year field study on cloud seeding funded by the Bureau of Reclamation, and for one part of that project, the shapes, maximum dimensions and masses of 4869 ice particles were determined. As described in M1990, ice particles were collected during winter storms in a petri dish and then imaged under a microscope equipped with a camera. The maximum dimension of each ice particle (i.e. diameter of a circumscribed circle around the particle) was later measured in the lab. In addition, each ice particle was melted with a heat-lamp under the microscope, with a corresponding photo taken immediately after melting. This resulted in hemispheric water drops that were imaged in the lab to measure the diameter of the hemispheres and from that the volume and mass of each ice particle was calculated. Although shattering can affect the aircraft measurements of ice particles due to the high sampling speed, it has no significant effect on the ground-based measurements. Moreover, the smallest size that is measured during SCPP (~ 150

$\mu\text{m}$ ) is considerably larger than the size range of shattered ice artifacts ( $D < 50 \mu\text{m}$ ; Jackson et al., 2012). Therefore, shattering during the SCPP measurements is not a concern. ...”

The authors state on page 28523 that the objective of their study is to develop  $m$ - $D$  and  $A$ - $D$  expressions that are representative of all ice particles for a given cloud type and temperature interval, suitable for use in climate models. I also note that the authors do talk some about measurement uncertainty. But, one question that they do not thoroughly address is variability. Past studies have shown that there is a lot of variability in derived  $m$ - $D$  and  $A$ - $D$  relations. Further, there is some variability even for a given cloud type of a fixed temperature. Given this, do the authors expect that representative relations can be found that are representative for all particles? Some discussion about variability and how the authors address such variability should be given.

Author response: The discussion on the variability of  $m$ - $D$  expression had been provided at the first paragraph of Sect. 3. The natural variability associated with ice particle mass measurements was minimized in two ways. First,  $m$  was estimated from the BL2006  $m$ - $A$  relationship for  $D > 200 \mu\text{m}$  (which represents the mean  $m$ - $A$  behavior in their dataset and thus removes much of the natural variability in  $m$ ), and second, variability was reduced by averaging the SPARTICUS PSD within each  $5^\circ\text{C}$   $T$  interval, as described in Sect. 2, producing one mean PSD of number, area and mass concentration for each  $T$  interval.

We also added more discussions: McFarquhar et al. (2007) showed that there is considerable variability in  $m$ - $D$  expression during the aircraft measurements of stratiform regions of mesoscale convective systems, and they used different  $m$ - $D$  expression for each flight. However as we show further in this section, the variability in  $m$ - $D$  relationship based on 13 flights in synoptic cirrus clouds during SPARTICUS does not exceed 32 % of the mean bin mass value, having a mean overall value of 13.48 %. Based on this low variability, we conclude that our  $m$ - $D$  expression is representative of all ice particles for the cloud type indicated (continental midlatitude synoptic or anvil cirrus clouds) and temperature interval.

Now, the first paragraph in Sect. 3 has changed (original manuscript, page 28527, starting at line 16):

“While in principle each PSD can be used to produce an  $m$ - $D$  or  $A$ - $D$  expression, in practice only the mean PSDs were used to develop the  $m$ - $D$  and  $A$ - $D$  expressions (explained in Sect. 2.3 and in the Supplement, Fig. S6). Although the averaging process reduces scatter, the coherency of the curves is somewhat surprising. The natural variability associated with ice particle mass measurements was minimized in two ways, thus facilitating the curve-fitting process. First,  $m$  was estimated from the BL2006  $m$ - $A$  relationship for  $D > 200 \mu\text{m}$  (which represents the mean  $m$ - $A$  behavior in a self-consistent way and thus removes much of the natural variability in  $m$ ), and second, variability was reduced by averaging the SPARTICUS PSD within each  $5^\circ\text{C}$   $T$  interval, as described in Sect. 2, producing one mean PSD of number, area and mass concentration for each  $T$  interval. The coherency of this data makes it amenable to curve-fitting with high

precision. McFarquhar et al. (2007) showed that there is considerable variability in  $m$ - $D$  expression during the aircraft measurements of stratiform regions of mesoscale convective systems, and they used a different  $m$ - $D$  expression for each flight. Our results differ for the reasons described above. Moreover, as we show further in this section, the variability in  $m$ - $D$  relationship based on 13 flights in synoptic cirrus clouds during SPARTICUS does not exceed 32% of the mean bin mass value, having a mean overall value of 13.48 %.”

A new paragraph was then added below this paragraph to address the review question:

“If ice particle morphology does not vary much within the cirrus clouds sampled, then our  $m$ - $D$  expressions should be representative of all ice particles for a given cloud type (continental midlatitude synoptic or anvil cirrus clouds) and temperature interval. Ice particle images from cirrus clouds tend to support this assumption, indicating high density, blocky-shaped irregular crystals with some bullet rosettes and side planes at larger sizes (e.g. Lawson et al., 2006b; Baker and Lawson, 2006b). But if there is a radical departure from this morphology genre and planar ice crystals having low aspect ratios (i.e.  $c$ -axis to  $a$ -axis ratio where  $c$ -axis is length of the prism face) dominate, our  $m$ - $D$  expressions could overestimate ice particle mass by a factor of  $\sim 3$  (Lawson, 2016).”

And we added a sentence (original manuscript, page 2852,3 line 5) and referred the reader to Sec. 3 for the discussion on variability:

“... (see Sect. 3 for the discussion of variability in  $m$ - $D$  and  $A$ - $D$  expressions).”

As noted in specific recommendations in the detailed comments below, one other recommendation I would give for this paper is to include some more detailed error or uncertainty analysis. In particular, assigning some uncertainties to the estimated mass amounts would have been beneficial. This would go beyond the uncertainty analysis that is done for the polynomial fit expressions for the  $m$ - $D$  and  $A$ - $D$  relations, but rather relate more to the uncertainties in the fundamentally measured quantities.

Author response: Similar to Fig. 6, we calculated the fractional uncertainties for the mean ice particle mass in each size bin of the measured PSDs. The pattern for the mass fractional uncertainties is similar to that for area fractional uncertainties. Mass uncertainties range between 0 and 32 % of the mean bin mass, with a mean overall value of 13.48 %. This explanation has been added to the text (original manuscript, page 28529, starting at line 16):

“... Similar to Fig. 6, we calculated the fractional uncertainties for the mean ice particle mass in each size bin of the measured PSDs (figure not shown). The pattern for the mass fractional uncertainties is similar to that for area fractional uncertainties. Mass uncertainties range between 0 and 32 % of the mean bin mass, with a mean overall fractional uncertainty of 13.48 %.”

Detailed comments:

Abstract line 10. The authors claim that field measurements of individual particle  $m$  are used from the 2DS/CPI. There are no measurements of mass from these probes. Further, the measurements of mass that are used to derive  $m$ - $D$  relations come from integrated measurements of masses of several particles combined rather than from measurements of mass of single particles (this is correctly stated on page 28520, line 14).

Author response: It is right that no measurements of mass exists from 2D-S and CPI probes, but the field measurements mentioned in line 10 refer to SCPP data in which each ice particle was imaged for the measurement of maximum dimension, and then was the ice particle melted and the diameter of the resulting hemispheric water drop was measured to calculate the actual mass. We added this explanation in Sect. 2.2 regarding the description of SCPP data. Also, we mentioned in line 10 (abstract) that this ground measurement is during a cloud seeding field campaign. We also clarified in line 11 that  $A$  and  $D$  are provided by measurements whereas  $m$  is estimated. So now, this part of abstract has changed to (original manuscript, page 28518, starting at line 10):

“... This was done by combining ground measurements of individual ice particle  $m$  and  $D$  formed at temperature  $T < -20$  °C during a cloud seeding field campaign with 2-dimensional stereo (2D-S) and Cloud Particle Imager (CPI) probe measurements of  $D$  and  $A$ , and estimates of  $m$ , in synoptic and anvil ice clouds at similar temperatures. ...”

And the first paragraph in Sect. 2.2 is modified (original manuscript, page 28522, starting at line 24):

“SCPP was a 3-year field study on cloud seeding funded by the Bureau of Reclamation, and for one part of that project, the shapes, maximum dimensions and masses of 4869 ice particles were determined. As described in M1990, ice particles were collected during winter storms in a petri dish and then imaged under a microscope equipped with a camera. The maximum dimension of each ice particle (i.e. diameter of a circumscribed circle around the particle) was later measured in the lab. In addition, each ice particle was melted with a heat-lamp under the microscope, with a corresponding photo taken immediately after melting. This resulted in hemispheric water drops that were imaged in the lab to measure the diameter of the hemispheres and from that the volume and mass of each ice particle was calculated. ...”

Page 28522, line 15. It is stated that the CPI data are used for sizes less than 100 micrometers. But, is there any diameter below which the CPI data are not used? For example, McFarquhar et al. (2013) showed that it was difficult to extract any information from CPI images for particles with  $D$  smaller than 35 micrometers.

Author response: As explained in McFarquhar et al. (2013), a widely-accepted lower limit is not available for CPI, and it might not be possible to determine the shape of particles that are smaller than a threshold. They showed that it was difficult to extract useful information from CPI images for particles with  $D < 35$   $\mu\text{m}$ . We used CPI data for sizes between 20  $\mu\text{m}$  and 100  $\mu\text{m}$ , and we

modified the text (original manuscript, Page 28522, line 15) to address this size range. The reason for this had been explained in the last paragraph in Sect. 2.4. We also cited McFarquhar et al. (2013) and changed the last paragraph in Sect. 2.4 (original manuscript, page 28527, starting at line 9):

McFarquhar et al. (2013) discussed that a widely-accepted lower limit is not available for the CPI, and they found that it was difficult to extract useful shape information from CPI images for particles with  $D < 35 \mu\text{m}$  for mixed-phase arctic clouds. However, in our study, shape is not a concern for the CPI size range we are using ( $20 \mu\text{m} < D < 100 \mu\text{m}$ ) since we assume hexagonal column geometry and only require length and width measurements, which are estimated for these sizes from a data processing algorithm developed at SPEC, Inc.

Page 28522, line 19. How is the CPI mass estimated?

Author response: The CPI mass is estimated from CPI projected area and aspect ratio by the method that we introduced in Appendix B. The text is modified to address the appropriate sections (original manuscript, page 28522, starting at line 17):

“... For other temperature ranges of synoptic clouds and for all temperature ranges of anvil clouds, estimated 2D-S mass (see Sect. 2.3) is used for size greater than  $200 \mu\text{m}$  and estimated CPI mass (see Sect. 2.4 and Appendix B) for size less than  $100 \mu\text{m}$ . ...”

Page 28522, line 25. How is maximum dimension defined? It is important to note that past studies have defined maximum dimension differently so it is important that the exact definition of maximum dimension (or methodology used to compute maximum dimension) be given.

Author response: Ice particle maximum dimension is measured as the diameter of a circumscribed circle around an ice particle. Mitchell et al. (1990) provided image of each ice particle under microscope, and measured ice particle maximum dimension as diameter of circumscribed circle. This clarification is added to the text (original manuscript, page 28522, starting at line 24):

“SCPP was a 3-year field study on cloud seeding funded by the Bureau of Reclamation, and for one part of that project, the shapes, maximum dimensions and masses of 4869 ice particles were determined. As described in M1990, ice particles were collected during winter storms in a petri dish and then imaged under a microscope equipped with a camera. The maximum dimension of each ice particle (i.e. diameter of a circumscribed circle around the particle) was later measured in the lab. ...”

Page 28523, line 21: Are particles from the smallest size bin in the 2DS used in the analysis? Jensen et al. (2013) reported that the 2DS may overestimate concentrations of particles with  $D < 15$  micrometers due to a poorly defined depth of field. Further, the sample volume for such sized



particles is very small so only a few counted particles can dominate the concentrations. Further, for the larger particles that occur on the edges of the photodiode, how much does reconstruction of partially imaged particles affect the estimated areas (and hence impact the calculated masses)? For what fraction of particles is reconstruction used?

Author response: Since we used CPI data for the size range smaller than 100  $\mu\text{m}$ , the former problem regarding the smallest size bin in the 2DS does not affect the calculations of various  $m$ - $D$  and  $A$ - $D$  relationships. We cited Jensen et al. (2013) and explained their findings regarding the smallest size range (original manuscript, page 28523, starting at line 22):

“... The data in the smallest size bin (5-15  $\mu\text{m}$ ) should be used with caution, because Jensen et al. (2013) showed that the largest uncertainty in depth of field for this size bin results in an overestimation of number concentration for particles in the smallest size bin. Since we used CPI data for the size range smaller than 100  $\mu\text{m}$ , the aforementioned problem does not affect the calculations of  $m$ - $D$  and  $A$ - $D$  relationships. ...”

Regarding the larger particles, no reconstruction was performed, and all particles that are not entirely inside the photodiode array were excluded from the data (“all-in” criteria). This process is described in the text (original manuscript, page 28524, starting at line 20):

“The original 2D-S data used in this study had been processed by the Stratton Park Engineering Company (SPEC), Inc. using the M1 technique for measuring ice particle length and area (see Appendix A in Lawson, 2011). However, the M1 method does not insure that the ice particle is completely imaged within the sample volume (i.e. that no portion is beyond the photodiode array). ... To overcome these drawbacks, the 2D-S data used here were processed using the newly developed M7 method that insures that the ice particles are completely imaged within the sample volume (“all-in” criteria). ...”

Page 28524, lines 6-11: It might be worthwhile also referencing the paper of Jackson et al. (2012) who found that the application of habit specific  $m$ - $D$  relations applied to size/shape distributions measured during the ISDAC field campaign gave better agreement with the bulk measured masses than did application of the Baker et al. (2006) approach to the measured size distributions.

Author response: This reference has been added in this paragraph (original manuscript, page 28524, starting at line 9):

“...But if there is a radical departure from this morphology genre and planar ice crystals having low aspect ratios (i.e.  $c$ -axis to  $a$ -axis ratio where  $c$ -axis is length of the prism face) dominate, our  $m$ - $D$  expressions could overestimate ice particle mass by a factor of  $\sim 3$  (Lawson, 2016). Such may be the case for Arctic mixed phase clouds, where Jackson et al. (2012) showed that the application of habit-specific  $m$ - $D$  relationships applied to size/shape distributions in arctic stratocumulus clouds during Indirect and Semi-Direct Aerosol Campaign (ISDAC) over North Slope of Alaska had better agreement with the measured IWC (mean difference is  $\sim 50\%$ ) than did the application of the BL2006 approach to the measured size distributions (mean difference is  $\sim 100\%$ ).”

Page 28524, lines 25-29: There is a limitation to this technique in that the probe sample volume will fall off rapidly with particle size for the entire in technique meaning that very few completely imaged particles will be available for the analysis. This limitation should be specifically stated. Second, what specifically is the “most accurate estimate for maximum dimension” and how is it obtained. Presumably this is very different than the length along the direction of travel which is very different than some of the definitions of maximum dimension that have been used in the literature. Some further comments on both of these points are warranted.

Author response: We added a supplement that is provided by SPEC Inc. to compare the M1 and M7 methods. Although the sample volume decreases by using M7 method, such decrease is not considerable. Figures S1 and S3 show number concentration and area concentration as functions of maximum dimension for cases of synoptic and anvil cirrus clouds, respectively. It is seen that M1 and M7 methods agree well for both number concentration and area concentration, and larger difference between M1 and M7 methods is observed for larger particles ( $D > 300 \mu\text{m}$ ). Moreover, the comparison of M1 and M7 methods for PSD number concentration and extinction is displayed in Figs. S2 and S4. The difference in sample area between M1 and M7 methods does not exceed 5 % and 13 % for synoptic and anvil cirrus clouds, respectively. The difference for projected area is more pronounced in anvil than in synoptic cirrus clouds due to the existence of slightly larger ice particles in anvil clouds that have a greater chance of intersecting the edges of the 2D-S field of view. This explanation is added to the text (original manuscript, page 28524, starting at line 29):

“... Although the sample volume decreases by using M7 method, such decrease is not determinant. It is shown in the supplement (Figs S1 and S2) that M1 and M7 methods agree well for both number concentration and area concentration, with a larger difference between the M1 and M7 methods observed for larger particles ( $D > 300 \mu\text{m}$ ). Moreover, the difference in PSD projected area between M1 and M7 methods does not exceed 5 % and 13 % for synoptic and anvil cirrus clouds, respectively (see Appendix A for a detailed discussion on the comparison between M1 and M7 methods). ...“

Regarding the measurement method of maximum dimension, the diameter of circumscribed circle around the particle is measured as maximum dimension in M7 method. This length is different than the length along the direction of travel (L1 that is used in M1 method). This is explained in Appendix A with more details. The definition of maximum dimension and how it is different than other studies and reference to Appendix A has been added to this part of text (original manuscript, page 28524, starting at line 26):

“... To overcome these drawbacks, the 2D-S data used here were processed using the newly developed M7 method that insures that the ice particles are completely imaged within the sample volume (“all-in” criteria), and this method uses the most accurate estimate for maximum dimension (diameter of circumscribed circle around the particle, see Appendix A). ...”

And Appendix A explains them with more details (original manuscript, page 28544, starting at line 15):

“There are various methods to process 2D-S data, such as M1, M2, M4, and M7 methods (Lawson, 2011). Explanation and comparison of all these methods are beyond the scope of this paper. The M1 method was originally used in this study, but the newly developed M7 method



was replaced for two main reasons. First, the M1 and M7 methods differ on the measurement of particle dimensions, as is shown in Fig. A1. The horizontal direction represents the direction of particle travel into the 2D-S probe and is sometimes referred to as the time dimension. The M1 method uses maximum dimension along the direction of travel (length scale  $LI$ ) as the maximum dimension, whereas the M7 method uses the maximum dimension of the particle 2D image as the diameter of circumscribed circle around the particle (length scale  $MaxLength$ ). Therefore, M7 method provides a more realistic measurement of maximum dimension, compared to many other studies that used  $LI$ . Length scale  $L4$  in Fig. A1 is determined from the maximum number of shadowed photodiodes (vertical array) at any given instant.

Second, the M1 and M7 methods are distinct in the treatment of particles that intersect the edges of the 2D-S field of view. Using the M1 method, all particles are included in the measurement of projected area and number concentration, even particles that intersect the edges of the 2D-S field of view, and in those cases their maximum dimension and projected area is approximated. When using the M7 method, only particles that are completely inside the 2D-S field of view (“all-in” particles) are included. This provides an accurate measurement of projected area and maximum dimension for all particles. Although the sample volume decreases by using M7 method, such a decrease is not significant. Figures S1 and S3 show number concentration and area concentration as functions of maximum dimension for cases of synoptic and anvil cirrus clouds, respectively. It is seen that the M1 and M7 methods agree well for both number concentration and area concentration, with a larger difference between the M1 and M7 methods observed for larger particles ( $D > 300 \mu\text{m}$ ). Moreover, the comparison of the M1 and M7 methods for the PSD number concentration and extinction is displayed in Figs. S2 and S4. The difference in PSD projected area between the M1 and M7 methods does not exceed 5 % and 13 % for synoptic and anvil cirrus clouds, respectively. Such difference in projected area is more pronounced in anvil than in synoptic cirrus due to slightly larger ice particles in anvil clouds that have a greater chance of intersecting the edges of the 2D-S field of view.”

Page 28525, lines 3-7: This averaging procedure over temperature intervals will mean that your contributions from PSDs with larger mass contents will dominate. In their classic study, Marshall and Palmer (1948) averaged PSDs with similar rainrates so that different mass contents would not dominate the comparisons.

Author response: Although the averaging over temperature intervals results in a larger contribution from PSDs with larger  $IWC$ , we show that variability in temperature-dependent  $m-D$  expressions does not exceed 32 % and has a mean value of 13.48 % (see Sect. 3). Therefore, the contribution from PSDs with larger  $IWC$  is not determinative. Moreover, the objective of this study is to develop  $m-D$  and  $A-D$  expressions for a given temperature interval and cloud type, suitable for use in climate models. Therefore, the  $m-D$  and  $A-D$  expressions for similar precipitation rates will not serve the objective of this study.

Page 28525, lines 14 and 15: Can a more quantitative description of relatively be given?

Author response: We assume that cloud extinction and median mass size are relatively invariant with time when the cloud extinction and median mass size do not exceed 2 times their mean and

are not less than 0.4 times their mean in a 60-second time period. This quantitative description has been added to the manuscript (original manuscript, page 28525, starting at line 13):

“... Moreover, the PSD selection process identified cloud regions (cloud extinction  $> 0.1 \text{ Km}^{-1}$ ) where cloud extinction and median mass size were relatively stable (i.e. in a 60-second time period, the cloud extinction and median mass size should not exceed 2 times their mean and should not be less than 0.4 times their mean), making it unlikely that liquid water was present. ...”

Page 28526, line 26: This assumption about hexagonal column geometry seems to be very different than past studies that have assumed small particles are typically quasispheres such as droxtals, Gaussian random spheres, Chebyshev particles or budding bucky balls. Can you justify this assumption? How important is this assumption to your final results?

Author response: Um and McFarquhar (2009) studied the radiative properties of small ice particles by assuming idealized shapes of droxtals, Gaussian random spheres, Chebyshev particles and budding bucky balls. They investigated particles with  $D < 50 \mu\text{m}$  and area ratio between 0.69 and 0.85, and they calculated ice particle mass from dimension. The purpose of our study is to estimate the mass of small ice particles from processed CPI data that contains measurements of ice particle projected area, length and width. We developed a method that utilizes all three of these properties to estimate ice particle mass. For the size-range we considered (20 to 100  $\mu\text{m}$ ), length-to-width ratios were generally  $< 1.5$ , confirming the presence of high-density ice particles, and for such aspect ratios, hexagonal columns appear to be as good a surrogate of small particle morphology as other shapes for estimating ice particle mass. They also provide a convenient means of using the aspect ratio estimates.

This explanation has been added to the text (original manuscript, page 28526, starting at line 25):

“This new methodology assumes that ice particles with size less than 100  $\mu\text{m}$  exhibit hexagonal column geometry. Such a geometrical assumption seems reasonable based on observations for sizes smaller than 100  $\mu\text{m}$  (see Lawson et al., 2006, their Figs. 4 and 5). While other authors have approximated small (e.g.  $D < 50 \mu\text{m}$ ) ice crystals as droxtals, Gaussian random spheres, Chebyshev particles and budding bucky balls (e.g. Um and McFarquhar, 2009), our study estimates the mass of small ice particles from processed CPI data that contains measurements of ice particle projected area, length and width. We developed a method that utilizes all three of these properties to estimate ice particle mass. For the size-range we considered (20 to 100  $\mu\text{m}$ ), the mean length-to-width ratio was  $1.41 \pm 0.26$ , confirming the dominance of high-density ice particles, and for such aspect ratios, hexagonal columns appear to be as good a surrogate of small particle morphology as the other shapes noted above for estimating ice particle mass. They also provide a convenient means of using the aspect ratio estimates. As shown in Appendix B, for an aspect ratio of 1.0, the difference in ice mass between the spherical and hexagonal column assumption is 4%.”

Page 28527, line 4-5: I am a bit unclear on what is meant by not using any mass estimation technique for the size range of 100-200 micrometers. Does this mean that these particles are not considered in your calculation?

Author response: Yes. Although the assumption of small ice particles as hexagonal column is reasonable for  $D < 100 \mu\text{m}$ , it overestimates the mass for ice particles with  $100 \mu\text{m} < D < 200 \mu\text{m}$ . This is due to the fact that ice crystals in this size range begin to develop branches or extensions, becoming more complex and less compact (Bailey and Hallett, 2004, 2009). In other words, ice particles in this size range have less density than particles with  $D < 100 \mu\text{m}$ . Since the BL2006  $m$ - $A$  expression and the assumption of small ice particles as hexagonal column are not valid for  $100 \mu\text{m} < D < 200 \mu\text{m}$ , we did not use any mass estimation for this size range. The exception is for  $-65 \text{ }^\circ\text{C} < T \leq -55 \text{ }^\circ\text{C}$ , where we used the BL2006  $m$ - $A$  method to estimate mass from CPI projected area for  $D$  between 100 and 200  $\mu\text{m}$ , because the number of size bins available for  $D > 200 \mu\text{m}$  is limited (See Fig. 4, where it shows that data for this coldest temperature interval is available only for  $D < 600 \mu\text{m}$ ). This is the most accurate approach for this size interval for  $T \leq -55 \text{ }^\circ\text{C}$ , which is critical for determining  $m$ - $D$  expressions for these colder temperature intervals. This is explained in the 3<sup>rd</sup> paragraph under Sec. 2.4.

Page 28529, line 9: How useful are temperature-dependent curves? In a model scheme typically a single  $m$ - $D$  relation is adopted, so how useful is it to have curves as functions of temperature?

Author response:

Fontaine et al. (2014) found that it is not proper to employ a single temperature-independent  $m$ - $D$  expression for all clouds, because such an expression neglects the considerable natural variability of mass as a function of dimension. We showed that it is sufficient to categorize  $m$ - $D$  expressions into three temperature intervals for a given cloud (see Table 1, and Fig. 4). Such classification is practical for modeling purposes. This explanation has been added to the text (original manuscript, page 28528, starting at line 21):

“... Fontaine et al. (2014) found that it is not proper to employ a single temperature-independent  $m$ - $D$  expression for all clouds, because such expression neglects the considerable natural variability of mass as a function of dimension. We showed that it is sufficient to categorize  $m$ - $D$  expressions into three temperature intervals for a given cloud. Such classification is practical for modeling purposes. ...”

Page 28532, line 17: It is worth noting that agreement will always appear good on a logarithmic scale. How good does the agreement have to be in order to be considered good?

Author response: We calculated the percent difference on the normal scale, and not on a logarithmic scale. In other words, it is calculated as  $100 \times (m_{\text{SCPP}} - m_{\text{SPARTICUS}}) / [(m_{\text{SCPP}} + m_{\text{SPARTICUS}}) / 2]$  for each size bin. In this sense, the calculated mean percent difference of 28% shows a good agreement. We modified the text (original manuscript, page 28532, starting at line 12):

“Getting still more quantitative, the percent difference of the SCPP cold habit mean mass for a given size interval was compared with the corresponding ice particle mass from the SPARTICUS curve fit. In other words, the percent difference is calculated as  $100 \times (m_{\text{SCPP}} - m_{\text{SPARTICUS}}) / [(m_{\text{SCPP}} + m_{\text{SPARTICUS}}) / 2]$  for each size bin (figure not shown). Percent differences are less than 53% in all size bins, and the mean percent difference for all size-bins was 28%. Note that percent difference is calculated on the normal scale, and not on the logarithmic scale. Given the natural variability observed for ice particle masses, this level of agreement is considered good. ...”

Page 28536, line 24: Can you be more quantitative on what you mean by “valid over a limited range of D”. This would help those wishing to apply such relationships.

Author response: There is no quantitative size range in this case since the range of D is subjective and is determined by the error that a particular user is willing to tolerate. Errors encountered when using m-D and A-D power laws relative to this new approach are shown in Figs. 12, 13 and 14 (black and blue curves) regarding the calculation of N,  $D_e$  and  $V_m$ . These figures illustrate the increased accuracy obtained by matching the power laws to the PSD moment(s) of interest. Examples illustrating how m-D power laws are valid over limited D ranges are given in Fig. 1 and are discussed in Sect. 1.

The text in Sect. 6.1 (original manuscript, page 28536, starting at line 24) has been modified:

“While these relationships are commonly used in climate models, it is sometimes not recognized that such power laws are only valid over a limited range of D (examples include Fig. 1 and also Table 1 in Mitchell 1996). ...”

And the text in Sect. 1 (original manuscript, page 28519, starting at line 17) has been modified:

“... But these approaches implicitly assume that the m-D relationship conforms to a single size-independent power law, whereas Table 1 in Mitchell (1996) indicates that it often takes two or even three m-D power laws to describe a given m-D relationship over all relevant sizes. For example, Mitchell (1996) determined three power laws for hexagonal columns for three size ranges:  $30 \mu\text{m} < D \leq 100 \mu\text{m}$ ,  $100 \mu\text{m} < D \leq 300 \mu\text{m}$ , and  $300 \mu\text{m} < D$ . Cotton et al. (2012 ; hereafter C2012) have developed a bulk IWC approach that yields two m-D power laws that better describe the observations, assuming an exponent of 3 for the smallest ice particle sizes ( $D < 70 \mu\text{m}$ ). ...”

## Anonymous Referee #2:

Review on "Developing and bounding ice particle mass- and area-dimension expressions for use in atmospheric models and remote sensing" submitted to Atmospheric Chemistry and Physics by E. Erfani and D. L. Mitchell

The paper describes a level more complex and better fit to  $m$ - $D$  and  $A$ - $D$  relationships than the traditional power law relationships, and then the paper presents an accommodation on how the more complex relations can be used in climate and cloud models without requiring all too expensive computation.

The reviewer is especially impressed on the quality of the writing, and the thoroughness and completeness of the arguments. While we may have differences in writing style and different preferences for expressing error or representing measurements, the paper comes across as well edited and prepared. Also clearly the topic is relevant and makes an important line-item to list of potential improvements in climate modeling.

Recommendation is publication after revision addressing the following suggestions:

The reviewer's main concern in the paper in its current form is how the natural variability is represented, and how approximations are justified. The stated purpose of the paper is to "develop  $m$ - $D$  and  $A$ - $D$  expressions that are representative of all ice particles for a given cloud type and temperature interval, suitable for use in climate models." (28523/3-5) The goal is to get past the natural variation in ice crystal ensemble properties to an average parameterization suitable for representing ice crystal properties in  $25 \times 25 \text{ km}^2$  grid boxes in just 2 coefficients. Natural variation could be seen as a nuisance or unimportant noise. The reviewer would prefer to see it portrayed and dealt with more, while others might argue it's outside the scope of the paper. The reviewer argues that seeing the natural variation in figures and laid out more clearly in text strengthens the paper in that it helps the reader understand and trust the results more than if it goes un-portrayed and unsaid.

Author response: We added a "supplement" to the paper that contains a two-panel figure that shows  $m$ - $D$  and  $A$ - $D$  expressions and data points for all PSDs without the temperature dependence (Fig. S5). Also shown in this figure is mean and standard deviation in each size bin. In this way, the natural variability of  $m$ - $D$  and  $A$ - $D$  expressions is presented. This figure is now mentioned at the first paragraph of Sect. 3 along with the discussion on the variability of  $m$ - $D$  expression. The natural variability associated with ice particle mass measurements was minimized in two ways. First,  $m$  was estimated from the BL2006  $m$ - $A$  relationship for  $D > 200 \mu\text{m}$  (which represents the mean  $m$ - $A$  behavior in a self-consistent way and thus removes much of the natural variability in  $m$ ), and second, variability was reduced by averaging the SPARTICUS PSD within each  $5 \text{ }^\circ\text{C}$   $T$  interval, as described in Sect. 2, producing one mean PSD of number, area and mass concentration for each  $T$  interval.

We also added more discussions: McFarquhar et al. (2007) showed that there is considerable variability in  $m$ - $D$  expression during the aircraft measurements of stratiform regions of mesoscale convective systems, and they used different  $m$ - $D$  expression for each flight. However, as we show further in this section, the standard deviation in  $m$ - $D$  relationship based on 13 flights

in synoptic cirrus clouds during SPARTICUS does not exceed 32 % of the mean bin mass value, having a mean overall value of 13.48 %.

Now, the first paragraph in Sect. 3 has changed (original manuscript, page 28527, starting at line 16):

“Figure S5 shows  $m$ - $D$  and  $A$ - $D$  expressions and data points for all PSDs for all temperatures considered here. Also shown in this figure is mean and standard deviation in each size bin. In this way, the natural variability of the  $m$ - $D$  and  $A$ - $D$  PSD data is presented. While in principle each PSD can be used to produce an  $m$ - $D$  or  $A$ - $D$  expression, in practice only the mean PSDs in 5 °C temperature intervals were used to develop the  $m$ - $D$  and  $A$ - $D$  expressions (explained in Sect. 2.3 and in the Supplement, Fig. S6). Although the averaging process reduces scatter, the coherency of the curves in Fig. S6 is somewhat surprising. The natural variability associated with ice particle mass measurements was minimized in two ways, thus facilitating the curve-fitting process. First,  $m$  was estimated from the BL2006  $m$ - $A$  relationship for  $D > 200 \mu\text{m}$  (which represents the mean  $m$ - $A$  behavior in a self-consistent way and thus removes much of the natural variability in  $m$ ), and second, variability was reduced by averaging the SPARTICUS PSD within each 5 °C  $T$  interval, as described in Sect. 2, producing one mean PSD of number, area and mass concentration for each  $T$  interval. The latter can be seen by comparing Figs. S5 and S6. The coherency of this data makes it amenable to curve-fitting with high precision. McFarquhar et al. (2007) showed that there is considerable variability in the  $m$ - $D$  expression during aircraft measurements of stratiform regions of mesoscale convective systems, and they used different  $m$ - $D$  expression for each flight. However, as we show further in this section, the variability in  $m$ - $D$  relationship based on 13 flights in synoptic cirrus clouds during SPARTICUS does not exceed 32 % of the mean bin mass value, having a mean overall value of 13.48 %.”

And we added a sentence (original manuscript, page 28523, line 5) and referred the reader to Sec. 3 for the discussion on variability:

“... (see Sect. 3 for the discussion of variability in  $m$ - $D$  and  $A$ - $D$  expressions).”

28527/18, Suggested is a two-panel figure showing something similar to Figure 5, but with data points from each temperature range in Tables 1 and 2 on  $m$ - $D$  and  $A$ - $D$  axes. The idea being to show the scatter.

Author response: A two-panel figure is added that shows  $A$ - $D$  and  $m$ - $D$  data points averaged for PSDs in 5 °C temperature intervals (Fig. S6). This is actually the figure that was not shown in the original manuscript, but was explained in this part. To avoid the repetitive explanations, we refer to the previous comment immediately above. The manuscript has also been modified to refer to this figure (original manuscript, page 28527, starting at line 16) as described in the previous comment.



28528/19, Says greater accuracy can be made by fitting to temperature intervals. But the fits appear so similar in Figure 4. Could the authors please comment on a fit without the temperature dependence, and quantify the improvement in splitting up into temperature regimes? How could a climate model smoothly vary between the fits once a temperature boundary is crossed?

Author response: We agree that the fits in Fig. 4 are similar, and the regression equations for the A-D and m-D plots in Fig. S5, based on all temperatures, are now included for those who would prefer temperature-independent relationships. While the  $R^2$  for these curve fits (0.9924 and 0.9954, respectively) is similar to those in Tables 1 and 2, the actual values predicted by the three temperature-dependent fits does render more accurate A and m estimates, as shown in Figs. 4 and S6. Qualitative improvements in accuracy can be estimated from the figures while quantitative improvements can be calculated via Tables 1 and 2. Since indeed the fits are similar, a climate model can use these fits without using any smoothing function when crossing temperature boundaries. In fact, this m-D/A-D scheme has already been used in CAM5, as described in Eidhammer et al. (2016, submitted to J. Climate).

These explanations have been added to manuscript (original manuscript, page 28528, starting at line 21):

“...While the temperature-dependent A-D and m-D fits are similar, and the  $R^2$  values for the temperature-independent A-D and m-D fits in Fig. S5 (0.9924 and 0.9954, respectively, based on all temperatures) are similar to those in Tables 1 and 2, the actual values predicted by these temperature-dependent fits does render more accurate A and m estimates, as shown in Figs. 4 and S6. Since the fits are similar, a climate model can use these fits without using any smoothing function when crossing temperature boundaries. In fact, this m-D/A-D scheme has been used in a GCM, as described in Eidhammer et al. (2016). ...”

28524/26-30, The "all-in" criteria limits the sample volume for the larger ice crystals measured by the 2D-S. That is, a 1mm ice crystal has a smaller chance of appearing all-in vs. a 0.2 mm crystal. If this limitation in volume sample rate is accounted for, it should be stated.

Author response: We added a supplement document that has been provided by SPEC Inc. to compare the M1 and M7 methods, and it addresses this issue. Although the sample volume decreases by using the M7 method, such a decrease is not considerable. Figures S1 and S3 show number concentration and area concentration as functions of maximum dimension for cases of synoptic and anvil cirrus clouds, respectively. It is seen that the M1 and M7 methods agree well for both number concentration and area concentration, and the larger difference between the M1 and M7 methods is observed for larger particles ( $D > 300 \mu\text{m}$ ). Moreover, the comparison of the M1 and M7 methods for the PSD number concentration and extinction is displayed in Figs. S2 and S4. The difference in sample area between M1 and M7 methods does not exceed 5 % and 13 % for synoptic and anvil cirrus clouds, respectively. In other words, the difference for projected area is more pronounced in anvil than in synoptic cirrus clouds due to the existence of slightly larger ice particles in anvil clouds that have a greater chance of intersecting the edges of the 2D-

S field of view. This explanation is added to the text (original manuscript, page 28524, starting at line 29):

“... Although the sample volume decreases by using the M7 method, such a decrease is not significant. It is shown in the supplement (Figs S1 and S2) that the M1 and M7 methods agree well for both number concentration and area concentration, with the largest difference between the M1 and M7 methods observed for larger particles ( $D > 300 \mu\text{m}$ ). Moreover, the difference in PSD projected area (i.e. extinction) between the M1 and M7 methods does not exceed 5 % and 13 % for synoptic and anvil cirrus clouds, respectively (see Appendix A for detailed discussion on the comparison between M1 and M7 methods). ...”

And Appendix A has been modified (original manuscript, page 28544, starting at line 8):

“...Although the sample volume decreases by using M7 method, such a decrease is not significant. Figures S1 and S3 show number concentration and area concentration as functions of maximum dimension for cases of synoptic and anvil cirrus clouds, respectively. It is seen that the M1 and M7 methods agree well for both number concentration and area concentration, with a larger difference between the M1 and M7 methods observed for larger particles ( $D > 300 \mu\text{m}$ ). Moreover, the comparison of the M1 and M7 methods for the PSD number concentration and extinction is displayed in Figs. S2 and S4. The difference in PSD projected area (i.e. extinction) between the M1 and M7 methods does not exceed 5 % and 13 % for synoptic and anvil cirrus clouds, respectively. Such difference in projected area is more pronounced in anvil than in synoptic cirrus due to slightly larger ice particles in anvil clouds that have a greater chance of intersecting the edges of the 2D-S field of view. ”

28543/10-13, The reviewer invites the authors to speculate on how broadly this fit might be applied to other similar clouds such as tropical or subtropical anvil cirrus, or perhaps arctic cirrus. The fact is many parameterization studies such as Brown and Francis 1996 are applied (extrapolated) outside their valid regime in models and other studies (Heymsfield et al. 2010). The synoptic and anvil cloud fits in this paper aren't so different. How different could the fits to ice particle data from other clouds be? Or where might the ice appear so different these parameterizations would be clearly inappropriate to use? Any insight would be appreciated.

Author response: A study by Lawson (2016) has recently been conducted to address this exact question, as the BL2006 m-A power law has been demonstrated to not work well for Arctic clouds. Therefore a similar m-A study was conducted but this time using planar ice crystals having relatively low aspect ratios ( $\ll 1$ ). Citing this study, we have added a new paragraph to Section 3 (shown below) to address this important question:

If ice particle morphology does not vary much within the cirrus clouds sampled, then our  $m$ - $D$  expressions should be representative of all ice particles for a given cloud type (continental midlatitude synoptic or anvil cirrus clouds) and temperature interval. Ice particle images from various types of cirrus clouds tend to support this assumption, indicating high density, blocky-shaped irregular crystals with some bullet rosettes and side planes at larger sizes (e.g. Lawson et al., 2006b; Baker and Lawson, 2006b). But if there is a radical departure from this morphology genre and planar ice crystals having low aspect ratios (i.e. c-axis to a-axis ratio where c-axis is length of the prism face) dominate, our m- $D$  expressions could overestimate ice particle mass by

a factor of  $\sim 3$  (Lawson, 2016). Such reasoning may explain findings from Arctic mixed phase clouds, where Jackson et al. (2012) showed that the application of habit-specific  $m$ - $D$  relationships applied to size/shape distributions in arctic stratocumulus clouds during Indirect and Semi-Direct Aerosol Campaign (ISDAC) over North Slope of Alaska had better agreement with the measured IWC (mean difference is  $\sim 50\%$ ) than did the application of the BL2006 approach to the measured size distributions (mean difference is  $\sim 100\%$ ). Similar findings from Arctic mixed phase clouds are reported in Avramov et al. (2011).

The manuscript has been modified to reflect all these changes (original manuscript, page 28528, before line 1):

“If ice particle morphology does not vary much within the ice clouds sampled, then our  $m$ - $D$  expressions should be representative of all ice particles for a given cloud type (continental midlatitude synoptic or anvil cirrus clouds) and temperature interval. Ice particle images from various types of cirrus clouds tend to support this assumption, indicating high density, blocky-shaped irregular crystals with some bullet rosettes and side planes at larger sizes (e.g. Lawson et al., 2006b; Baker and Lawson, 2006b). But if there is a radical departure from this morphology genre and planar ice crystals having low aspect ratios (i.e. c-axis to a-axis ratio where c-axis is length of the prism face) dominate, our  $m$ - $D$  expressions could overestimate ice particle mass by a factor of  $\sim 3$  (Lawson, 2016). Such reasoning may explain findings from Arctic mixed phase clouds, where Jackson et al. (2012) showed that the application of habit-specific  $m$ - $D$  relationships applied to size/shape distributions in arctic stratocumulus clouds during Indirect and Semi-Direct Aerosol Campaign (ISDAC) over North Slope of Alaska had better agreement with the measured IWC (mean difference is  $\sim 50\%$ ) than did the application of the BL2006 approach to the measured size distributions (mean difference is  $\sim 100\%$ ). Similar findings from Arctic mixed phase clouds are reported in Avramov et al. (2011).”

The manuscript has also been modified to address the Conclusions (original manuscript, page 28543, starting at line 10):

“This study was focused only on mid-latitude continental ice clouds, and not on marine anvil or synoptic cirrus, orographic cirrus and/or Arctic ice clouds. Application of BL2006 (which is based on a subset of SCPP data from mid-latitude continental clouds) to tropical anvil clouds produced IWC with only  $\sim 18\%$  difference compared to measured bulk IWC (Lawson et al. 2010). However, use of BL2006 in arctic mixed phase clouds leads to IWC  $\sim 100\%$  larger than measured bulk IWC (Jackson et al. 2012). Additional research is required to apply and test the approach introduced in this study in different environments.”

28544/21-22, The reviewer invites the authors to quantify in some way how much their columnar representation of small ice crystals is more accurate than the traditional spherical ice assumption.

Author response: We thank the reviewer for this suggestion; An explanation has been added to the end of Appendix B (original manuscript, page 28546, after line 18):

“One benefit of the hexagonal column assumption is consideration of ice particle aspect ratio. The spherical ice assumption means that the aspect ratio is unity. Assuming that ice particles are spherical, their mass can be calculated as a function of projected area (e.g.

$m_{sphere} = \rho_i \frac{4}{3\sqrt{\pi}} A_{sphere}^{3/2}$ ). We calculated the percent difference of mass between the spherical and hexagonal column assumptions (where column aspect ratio = 1.0), and this value is ~ 4%.”

This issue was brought up by the other referee, and this point is now addressed in the text (original manuscript, page 28526, starting at line 25):

“This new methodology assumes that ice particles with size less than 100  $\mu\text{m}$  exhibit hexagonal column geometry. Such a geometrical assumption seems reasonable based on observations for sizes smaller than 100  $\mu\text{m}$  (see Lawson et al., 2006, their Figs. 4 and 5). While other authors have approximated small (e.g.  $D < 50 \mu\text{m}$ ) ice crystals as “droxtals”, Gaussian random spheres, Chebyshev particles and budding bucky balls (e.g. Um and McFarquhar, 2009), our study estimates the mass of small ice particles from processed CPI data that contains measurements of ice particle projected area, length and width. We developed a method that utilizes all three of these properties to estimate ice particle mass. For the size-range we considered (20 to 100  $\mu\text{m}$ ), the mean length-to-width ratio was  $1.41 \pm 0.26$ , confirming the dominance of high-density ice particles, and for such aspect ratios, hexagonal columns appear to be as good a surrogate of small particle morphology as the other shapes noted above for estimating ice particle mass. They also provide a convenient means of using the aspect ratio estimates. As shown in Appendix B, for an aspect ratio of 1.0, the difference in ice mass between the spherical and hexagonal column assumption is 4%.”

Tables 1 and 2, How were the temperature ranges -40 to -20, -55 to -40, and -65 to -55 chosen, with their uneven intervals? Was there a similarity criteria that led to putting the 5C temperature intervals together sometimes, and not other times?

Author response: First, we calculated values of mean dimension, mass, and projected area for each 5  $^{\circ}\text{C}$  T interval, and provided plots of m-D and A-D expressions for each 5  $^{\circ}\text{C}$  T interval. We then observed that m-D and A-D expressions for 5  $^{\circ}\text{C}$  T intervals have negligible differences within the larger temperature ranges of  $-40^{\circ}\text{C} < T < -20^{\circ}\text{C}$ ,  $-55^{\circ}\text{C} < T < -40^{\circ}\text{C}$ , and  $-65^{\circ}\text{C} < T < -55^{\circ}\text{C}$ . In order to keep m-D and A-D expressions as simple as possible without losing accuracy, we did not provide Tables 1 and 2 for each 5  $^{\circ}\text{C}$  T interval. However for uncertainty calculations, we kept the 5  $^{\circ}\text{C}$  T interval, because such similarity criteria is not observed for uncertainty and variability. This explanation has been added to the manuscript (original manuscript, page 28528, starting at line 16):

“Values of mean dimension, mass, and projected area were first calculated for each 5  $^{\circ}\text{C}$  T interval, and plots of m-D and A-D expressions were provided for each 5  $^{\circ}\text{C}$  T interval (Fig. S6). It was then observed that m-D and A-D expressions for 5  $^{\circ}\text{C}$  T intervals have negligible differences within the larger temperature ranges of  $-40^{\circ}\text{C} < T < -20^{\circ}\text{C}$ ,  $-55^{\circ}\text{C} < T < -40^{\circ}\text{C}$ , and  $-65^{\circ}\text{C} < T < -55^{\circ}\text{C}$ . In order to keep m-D and A-D expressions as simple as possible without losing accuracy, the coefficients of polynomial fits are not provided for each 5  $^{\circ}\text{C}$  T interval. Instead, the mean PSDs were grouped into the above mentioned three temperature categories and 2<sup>nd</sup> order polynomial curve fits were calculated for each category as shown in Tables 1 and 2. ...”

Figure A1 lacks orientation for the reader. Suggested is adding axes to show flow direction, diode array direction and diode array width. Why are there two ice particle shadowgraphs shown? What's the difference between them? Why is L4 in the right figure so much smaller than its crystal?

Author response: All the orientations and directions (e.g. axes, flow direction, photodiode array direction and width) have been added to Figure A1. Two ice particles are shown to give the reader an idea of how different length scales (L1, L4, and MaxLength) for different ice particle shapes are measured and calculated by 2D-S and its respective software. L4 is not the particle "height" range (projected along the vertical photodiode array) during its entire transit time through the sample volume; rather it is a measure of particle width at a given instant. Moreover, L4 is the maximum value of all these time-slices or widths measured. This latter point may be better illustrated by the ice particle on the left. This clarification about L4 has been added to Appendix A (original manuscript, page 28543, starting at line 25):

"... Note that length scale L4 in Fig. A1 is not the particle "height" range (projected along the vertical photodiode array) during its entire transit time through the sample volume; rather it is a measure of particle width at a given instant. Moreover, L4 is the maximum value of all these time-slices (i.e. widths) measured."

Also added to Appendix A is the clarification of two ice particles with different shapes (original manuscript, page 28543, starting at line 18):

"...First, the M1 and M7 methods differ on the measurement of particle dimensions, as is shown in Fig. A1. Two ice particles with different shapes are shown to give the reader an idea of how the different length scales (L1, L4, and MaxLength) for different ice particle shapes are measured and calculated by the 2D-S and its respective software. ..."

Figure B1 and the discussion in Appendix B1 on planes P1, P2 and P3. The reviewer is at a complete loss how these planes and the columnar crystal in the CPI sample volume are oriented. By far the best help would be a helpful drawing or figure. Suggested is adding orientation information to Figure B1. Show the axes, the planes, and the instrument sample volume.

Author response: The axes, planes, flow direction and photodiode array have been added to Figure B1. Also provided is 3 extra panels that show how the hexagonal column is projected, when its c-axis is parallel to P1, P2, or P3. Figure B1 caption has been modified to:

"Figure B1. a) 3-D geometry of a hexagonal prism, representative of small ice crystals. Assuming that the direction of view (beam direction) is along the x-axis, P1 is orthogonal to x-axis, P2 is orthogonal to y-axis, and P3 is orthogonal to z axis. Also shown is the projection of a hexagonal prism for three extremes, when its c-axis is parallel to b) P1, c) P2, and d) P3. See text for the definition of various symbols."

28528/21 resulted -> resulting

Author response: "resulted" has been changed to "resulting".

28545/16 Formula should be  $3^{3/2} a^2 / 8$ , if the reviewer understands the variable meaning correctly

Author response: Thank you for noticing to this typo. We corrected this, and checked other derivations. All other calculations were correct.

The paper has just enough symbols, it may be appropriate to add a variable index.

Author response: We added the list of variables as Appendix C (original manuscript, page 28547, starting at line 8):

### “Appendix C: List of symbols

$a$	maximum dimension across the basal face of a hexagonal crystal
$a_v$	prefactor in fall speed-dimension power law
$A$	projected area
$\langle A \rangle$	average projected area of a hexagonal crystal for all orientations
$A_{b,max}$	area of the basal face of a hexagonal crystal
$A_{p,max}$	area of the prism face of a hexagonal crystal
$A_r$	area ratio
$A_t$	total PSD projected area
$b_v$	exponent in fall speed-dimension power law
$c$	length along the prism face of a hexagonal crystal
$D$	maximum dimension of ice particle
$D_o$	characteristic dimension of the ice PSD
$\overline{D}$	mean maximum dimension of a PSD
$D_A$	median area dimension
$D_e$	effective diameter
$D_i$	dimension of interest
$D_m$	median mass dimension
$D_N$	number concentration dimension
$D_Z$	reflectivity dimension
$g$	gravitational constant
IWC	ice water content
$m$	mass of ice particle
$N$	number concentration
$N_o$	prefactor of a gamma PSD
PSD	particle size distribution
$R$	relative ratio of mass to area
$R^2$	coefficient of determination
$T$	temperature
$V$	terminal fall speed of ice particle



$V_h$	volume of a hexagonal crystal
$V_m$	mass-weighted terminal fall speed
$Z$	radar reflectivity
$X$	Best number
$\alpha$	prefactor in mass-dimension power law
$\beta$	exponent in mass-dimension power law
$\gamma$	prefactor in projected area-dimension power law
$\delta$	exponent in projected area-dimension power law
$\Gamma$	gamma function
$\varepsilon$	apparent aspect ratio
$\zeta$	true aspect ratio
$\eta$	dynamic viscosity of air
$\lambda$	slope parameter of a gamma PSD
$\nu$	dispersion parameter of a gamma PSD
$\sigma$	standard deviation
$\rho_{air}$	density of air
$\rho_i$	bulk density of ice"

1

2 **Developing and Bounding Ice Particle Mass- and Area-**  
3 **dimension Expressions For Use in Atmospheric Models and**  
4 **Remote Sensing**

5

6

7 **E. Erfani<sup>1,2</sup> and D. L. Mitchell<sup>1</sup>**

8

9 [1] {Desert Research Institute, Reno, Nevada, USA }

10 [2] {Graduate Program in Atmospheric Sciences, University of Nevada, Reno, Nevada, USA }

11

12 Correspondence to: Ehsan Erfani ([Ehsan@nevada.unr.edu](mailto:Ehsan@nevada.unr.edu))

13

1 **Abstract**

2 Ice particle mass- and projected area-dimension ( $m$ - $D$  and  $A$ - $D$ ) power laws are commonly used  
3 in the treatment of ice cloud microphysical and optical properties and the remote sensing of ice  
4 cloud properties. Although there has long been evidence that a single  $m$ - $D$  or  $A$ - $D$  power law is  
5 often not valid over all ice particle sizes, few studies have addressed this fact. This study  
6 develops self-consistent  $m$ - $D$  and  $A$ - $D$  expressions that are not power laws, but can easily be  
7 reduced to power laws for the ice particle size (maximum dimension or  $D$ ) range of interest, and  
8 they are valid over a much larger  $D$  range than power laws. This was done by combining ground  
9 field measurements of individual ice particle  $m$  and  $D$  formed at temperature  $T < -20$  °C during a  
10 cloud seeding field campaign ~~Sierra Cooperative Pilot Project (SCPP)~~ with 2-dimensional stereo  
11 (2D-S) and Cloud Particle Imager (CPI) probe measurements ~~(or estimates)~~ of  $D$ , and  $A$ , and  
12 estimates of  $m$ , in synoptic and anvil ice clouds at similar temperatures. The resulting  $m$ - $D$  and  
13  $A$ - $D$  expressions are functions of temperature and cloud type (synoptic vs. anvil), and are in good  
14 agreement with  $m$ - $D$  power laws developed from recent field studies considering the same  
15 temperature range ( $-60$  °C  $< T < -20$  °C).

16

## 1 1 Introduction

2 [Measurements of individual ice particle mass have shown](#) that the relationships between ice  
3 [particle mass and maximum dimension have the form of habit-dependent power laws \(Locatelli](#)  
4 [and Hobbs, 1974; Mitchell et al., 1990; hereafter M1990\)](#). The treatment of ice particle projected  
5 area and mass is fundamental for the prediction of ice cloud microphysical and radiative  
6 properties in cloud models at all scales. For example, Mitchell (1988) showed how treating ice  
7 particles as spheres in a steady-state snow growth model resulted in poor agreement between the  
8 observed and model predicted height-dependent evolution of ice particle size distributions  
9 (PSDs), relative to PSDs predicted using a non-Euclidian ice particle mass-dimension  
10 (henceforth  $m$ - $D$ , where  $D$  is maximum dimension) power law relationship. Moreover, ice  
11 particle  $m$ - $D$  and projected area-dimension (henceforth  $A$ - $D$ ) relationships are used to predict ice  
12 particle fall velocities (e.g. Mitchell, 1996; Heymsfield and Westbrook, 2010). Ice cloud optical  
13 properties have also been formulated in terms of ice particle  $m$ - $D$  and  $A$ - $D$  power laws, as  
14 described in Mitchell (1996), Mitchell et al. (2006) and Mitchell (2000, 2002). The ice PSD  
15 effective diameter ( $D_e$ ), used in other ice optical property schemes (e.g. Fu, 1996; Fu et al., 1998;  
16 Yang et al., 2005), is also based on the ratio of PSD mass to PSD projected area (e.g. Foot, 1988;  
17 Mitchell, 2002). From this, it is apparent that  $m$ - $D$  and  $A$ - $D$  expressions have the potential to  
18 integrate microphysical and radiative processes in cloud models in a self-consistent manner.

19 In addition to the treatment of microphysical and radiative processes in cloud models,  $m$ - $D$  and  
20  $A$ - $D$  expressions constitute critical a priori information used to retrieve cloud properties in  
21 ground- and satellite-based remote sensing. For example, uncertainties (standard deviations or  $\sigma$ )  
22 associated with  $m$ - $D$  and  $A$ - $D$  expressions strongly contribute to uncertainties in  $D_e$  and ice water  
23 content (IWC) retrievals that range from 60% to 68% and from 135% to 175%, respectively,  
24 relative to their mean values (Zhao et al., 2011). Reducing the uncertainty of  $m$ - $D$  and  $A$ - $D$   
25 expressions would reduce the uncertainties associated with these and other cloud property  
26 retrievals.

27 Research over the last decade has used aircraft measurements of bulk IWC and the ice PSD to  
28 develop best estimates of the  $m$ - $D$  power law relationship (e.g. Heymsfield et al., 2004;  
29 Heymsfield et al., 2007; Heymsfield et al., 2010; hereafter H2010). [Also, McFarquhar et al.](#)  
30 [\(2007\) used PSDs and radar reflectivities measured during spiral descents in the stratiform](#)

1 regions of mesoscale convective systems to determine the power law for each spiral. In addition,  
2 the recent study by Fontaine et al. (2014) employed ice particle images and radar reflectivities to  
3 derive the temperature-dependent power exponent and prefactor of power laws for tropical anvil  
4 clouds. But these approaches implicitly assumes that the  $m$ - $D$  relationship conforms to a single  
5 size-independent power law, whereas Table 1 in Mitchell (1996) indicates that it often  
6 takes two or even three  $m$ - $D$  power laws to describe a given  $m$ - $D$  relationship over all relevant  
7 sizes. For example, Mitchell (1996) determined three power laws for hexagonal columns for  
8 three size ranges:  $30 \mu\text{m} < D < 100 \mu\text{m}$ ,  $100 \mu\text{m} < D < 300 \mu\text{m}$ , and  $D > 300 \mu\text{m}$ . However, the  
9 H2010  $m$ - $D$  is valid only for  $D > 50 \mu\text{m}$ . Cotton et al. (2012 ; hereafter C2012) have developed a  
10 bulk IWC approach that yields two  $m$ - $D$  power laws that better describe the observations,  
11 assuming an exponent of 3 for the smallest ice particle sizes ( $D < 70 \mu\text{m}$ ). These  $m$ - $D$   
12 relationships consisting of two or three power laws are shown in Fig. 1 where it is seen that the  
13 dependence of  $m$  on  $D$  in log-log space is non-linear. Note that the C2012 relationship is based  
14 on all ice particle shapes present at the time of sampling whereas four relationships are for  
15 specific ice crystal habits, based on Table 1 in Mitchell (1996). The popular Brown and Francis  
16 (1995)  $m$ - $D$  power law, also based on all ice particle shapes present at the time of sampling, is  
17 also shown in Fig. 1 where it exceeds the mass of an ice sphere (the upper mass limit) when  $D <$   
18  $97 \mu\text{m}$ . Many investigators have assumed ice spheres for  $D < 97 \mu\text{m}$  when applying the Brown-  
19 Francis relationship, but this may introduce some error based on the findings of C2012. Clearly,  
20 the Brown-Francis relationship is not valid over all sizes and two  $m$ - $D$  relationships are needed  
21 to address the smaller sizes. In summary, these relationships imply that the  $m$ - $D$  relationship has  
22 some curvature in log-log space and a key objective of this study is to parameterize this  
23 curvature for a mixture of ice particle shapes commonly found in ice clouds.

24 Another main objective of this study is to provide the climate modeling and the ice cloud remote  
25 sensing community with a method for calculating representative ice particle masses and  
26 projected areas in ice clouds at sizes relevant to cirrus clouds in terms of temperature regime and  
27 cloud type (synoptic vs. anvil cirrus), including uncertainty estimates. To date, no direct  
28 measurements of individual ice particle masses have been made from an aircraft, so direct in situ  
29 measurements of size-resolved ice particle mass and dimension are not available. Given this  
30 limitation, a system is developed that attempts to make optimal use of the measurements that

Formatted: Font: Not Italic

1 currently exist. Thus, this study is not proposing a solution to this problem, but is proposing an  
2 improvement for describing the  $m$ - $D$  and  $A$ - $D$  relationships in cirrus clouds.

3 Section 2 of this study discusses the data and method, with the first subsection providing a brief  
4 overview of the general approach adopted for estimating  $m$ - $D$  expressions in cirrus clouds, and  
5 with the other subsections explaining ground-based measurements of individual ice particle  
6 masses and various aircraft in-situ measurements and their processing methods. Sections 3 and 4  
7 then provide more details, with Sect. 3 describing how aircraft and ground-based measurements  
8 were used to develop  $m$ - $D$  and  $A$ - $D$  relationships. In Sect. 4, the aircraft results are compared  
9 against the results from a cloud seeding program called the Sierra Cooperative Pilot Project  
10 (SCPP), described in [M1990 Mitchell et al. \(1990; hereafter M1990\)](#). In Sect. 5, a method for  
11 reducing these  $m$ - $D$  and  $A$ - $D$  expressions into  $m$ - $D$  and  $A$ - $D$  power law relationships over a  
12 limited size range is described, along with uncertainty estimates for the prefactor and exponent  
13 of these power law expressions. Section 6 provides a method for applying the polynomial fits to  
14 two-moment cloud microphysical schemes where an appropriate power law expression (derived  
15 from a polynomial fit) can be applied over the ice particle size range of interest. This section also  
16 describes the impact this scheme is likely to have on ice microphysical schemes that assume that  
17 ice particles are spherical. Summary and concluding remarks are given in Sect. 7.

18

## 19 **2 Data and Methods**

### 20 **2.1 Parameterization approach – general description**

21 To address the challenges described above, a non-standard approach was taken that combines  
22 aircraft measurements and estimates of ice particle projected area and mass, respectively, with  
23 single ice particle field measurements of mass and maximum dimension. The aircraft  
24 measurements were made during the Small Particle In Cirrus (SPARTICUS) field campaign  
25 (Mace et al., 2009), funded through the Atmospheric Systems Research (ASR) program by the  
26 Department of Energy (DOE), which took place during January-June 2010 over the continental  
27 U.S. (see Fig. 2 in Mishra et al., 2014 for the map of flight locations), from which 13 synoptic  
28 cirrus flights and 9 anvil cirrus flights were selected; these are listed in Table 1 of Mishra et al.



1 (2014). The 2-dimensional Stereo (2D-S) probe (Lawson et al., 2006a; Lawson, 2011) and Cloud  
2 Particle Imager (CPI) probe (Lawson et al., 2001) were onboard the aircraft, and were used in  
3 this study for the PSD measurements. In general, ice particle mass is estimated from the  
4 SPARTICUS measurements of ice particle projected area, as described in more detail below,  
5 giving an ice particle size range appropriate for ice clouds colder than about -20 °C. Ground-  
6 based measurements of  $m$  and  $D$  from SCPP corresponding to ice crystals that formed between -  
7 20 °C and -40 °C are then compared with the 2D-S estimates of  $m$  and  $D$  sampled between -20  
8 °C and -40 °C, and are found to be in relatively good agreement as discussed in Sec. 3. Due to  
9 this agreement, we postulate that the  $m$ - $D$  expression derived from the 2D-S probe data should be  
10 reasonable over this temperature range. We further postulate that ice particle mass estimates at  
11 colder temperatures, based on 2D-S probe ice particle projected area measurements, should be  
12 reasonable provided that the ice particle shape composition of the PSD does not significantly  
13 change at these colder temperatures. Moreover, we assume that a similar shape composition for  
14 anvil cirrus for a given temperature range relative to the shape composition in synoptic cirrus  
15 from -40 °C to -20 °C justifies using the 2D-S probe mass estimates (based on area  
16 measurements) for these anvil cirrus. As a proxy for ice particle shape, we use the mean area  
17 ratio ( $A_r$ ) for a given ice particle size-bin, where the  $A_r$  is the measured particle area divided by  
18 area of the circle defined by the particle's maximum dimension. This assumption extends this  $m$ -  
19  $D$  parameterization down to -55 °C. More details about this approach will now be given.

20 SCPP (see Sect. 2.2) provides unique direct measurements of mass for ice particles, with many  
21 SCPP ice particles having ice particle shapes similar to those found in cirrus clouds. Therefore,  
22 we used this data subset for size greater than 100  $\mu\text{m}$  and CPI data (see Sect. 2.4) for size ~~less~~  
23 ~~than~~ between 20  $\mu\text{m}$  and 100  $\mu\text{m}$ . Only those SCPP ice particles having formation temperatures  
24 between -20 °C and -40 °C (based on observed habits) were selected. For other temperature  
25 ranges of synoptic clouds and for all temperature ranges of anvil clouds, estimated 2D-S (see  
26 Sect. 2.3) mass is used for size greater than 200  $\mu\text{m}$  and estimated CPI mass (see Sect. 2.4 and  
27 Appendix B) for size less than 100  $\mu\text{m}$ . Since direct measurement of projected area is available  
28 for both 2D-S and CPI data, 2D-S area is used for size greater than 200  $\mu\text{m}$  and CPI area is used  
29 for size less than 200  $\mu\text{m}$  for all temperature ranges. Additional details are given below.

## 1 2.2 SCPP measurements

2 SCPP was a 3-year field study [on cloud seeding](#) funded by the Bureau of Reclamation, [and for](#)  
3 [one part of that project](#), ~~where~~ the shapes, maximum dimensions and masses of 4869 ice particles  
4 were determined. [As described in M1990, ice particles were collected during winter storms in a](#)  
5 [petri dish and then imaged under a microscope equipped with a camera. The maximum](#)  
6 [dimension of each ice particle \(i.e. diameter of a circumscribed circle around the particle\) was](#)  
7 [later measured in the lab. In addition, each ice particle was melted with a heat-lamp under the](#)  
8 [microscope, with a corresponding photo taken immediately after melting. This resulted in](#)  
9 [hemispheric water drops that were imaged later in the lab to measure the diameter of the](#)  
10 [hemispheres and from that the volume and mass of each ice particle was calculated. M1990](#)  
11 ~~[provided image of each ice particle by microscope, and measured ice particle maximum](#)~~  
12 ~~[dimension as diameter of circumscribed circle. Then, each particle was melted and the resulting](#)~~  
13 ~~[hemispheric water drop was imaged to measure the diameter of hemisphere, and from that the](#)~~  
14 ~~[mass of ice particle was calculated. Although shattering can affect the aircraft measurements of](#)~~  
15 ~~[ice particles due to the aircraft high sampling speed, it has no significant effect on the ground-](#)~~  
16 ~~[based measurements. Moreover, the smallest size that is measured during SCPP \(~ 150  \$\mu\text{m}\$ \) is](#)~~  
17 ~~[considerably larger than the size range of that shattered ice artifactsing is significant \( \$D < 50\$](#)~~   
18  ~~[\$\mu\text{m}\$ ; Jackson et al., 2012\). Therefore, there is no uncertainty due to shattering for during the](#)~~  
19 ~~[SCPP measurements is not a concern.](#)~~ While greater magnification was used to photograph the  
20 ice particles during the last year, for purposes of measuring ice particle size and mass, the lower  
21 magnification (25 $\times$ ) was sufficient. In this study, we consider those ice particles measured during  
22 the SCPP that have shapes initially formed between -20 and -40  $^{\circ}\text{C}$ . Moreover, the objective of  
23 M1990 was to develop *m-D* power laws for specific ice particle habits or shape categories (e.g.  
24 rimed column aggregates), whereas the objective of this study is to develop *m-D* and *A-D*  
25 expressions that are representative of all ice particles for a given cloud type and temperature  
26 interval, suitable for use in climate models [\(see Sect. 3 for the discussion of variability in \*m-D\*](#)  
27 [and \*A-D\* expressions\).](#)

28 Such field observations, conducted during winter storms in the Sierra Nevada Mountains,  
29 provided measurements for each individual ice particle sampled, including date and time,  
30 maximum dimension, mass, shape (if identifiable), crude level of riming (light, moderate,

1 heavily rimed, or graupel), and temperature range that produces the observed ice particle shape.  
2 Software was created to extract any combination of ice particle shapes. For the winter storms  
3 sampled, most of the cold habit ice crystals are expected to originate between -20 and -40 °C,  
4 although cloud tops colder than -40 °C are possible. Ice particle shapes associated with  $T < -20$   
5 °C that were measured during this field study include short columns (aspect ratios were  $< 2$ ) and  
6 combinations thereof, side planes and their aggregates, bullets, bullet rosettes and aggregates  
7 thereof, and combinations of any of these crystal types.

### 8 **2.3 2D-S probe**

9 PSDs were sampled using the 2D-S probe, which measures the size-resolved concentrations of  
10 ice particle number and projected area. A total of 193 synoptic ice cloud PSDs and 115 anvil  
11 cirrus PSDs were sampled and analyzed. Ice particle concentrations were measured down to 10  
12  $\mu\text{m}$  (5-15  $\mu\text{m}$  size bin) and up to 1280  $\mu\text{m}$  in ice particle length. The data in the smallest size bin  
13 (5-15  $\mu\text{m}$ ) should be used with caution, because Jensen et al. (2013) showed that the largest  
14 uncertainty in depth of field for this size bin results in an overestimation of number concentration  
15 for particles in the smallest size bin. Since we used CPI data for the size range smaller than 100  
16  $\mu\text{m}$ , the aforementioned problem does not affect the calculations of  $m-D$  and  $A-D$  relationships.

17 Ice particle mass is not directly measured, but is estimated using a power law that relates ice  
18 particle projected area to mass (Baker and Lawson, 2006a; hereafter BL2006). This relationship  
19 was developed from a subset of ice particles (865 particles) measured during SCPP. Using image  
20 analysis software, the projected area of ice particles in this subset was calculated from their  
21 photographed magnified images. The BL2006 study found that ice particle projected area was a  
22 more reliable predictor of particle mass than was maximum dimension. Their  $m-A$  power law  
23 was derived from many types of ice particle habits or shapes, and of the 550 identifiable ice  
24 particles, 36% were moderately or heavily rimed. This  $m-A$  power law is now commonly used to  
25 estimate size-resolved mass concentrations from 2D-S probe measurements of projected area.  
26 Integrating these mass concentrations over the PSD, the PSD IWC is determined.

27 One might ask how broadly the results of this study for mid-latitude continental clouds can be  
28 applied to other clouds such as tropical anvil, or arctic clouds. Although this is beyond the scope  
29 of this paper and can be the subject of future studies, some insights can be implied from previous

1 ~~studies. Since our study and also BL2006 use the same field campaign (SCCP) in mid-latitude~~  
2 ~~continental region, it is helpful to mention the results of using BL2006 method for other cloud~~  
3 ~~types. IWCs based on BL2006, determined by integration over PSDs, in this way have been~~  
4 compared to IWCs directly measured by the Counterflow Virtual Impactor (CVI) probe during  
5 the Tropical Composition, Cloud and Climate Coupling (TC4) field campaign (Lawson et al.,  
6 2010), where the 2D-S and CVI probes were co-located on the same aircraft with identical  
7 sampling times. A regression line relating the 2D-S and CVI IWC measurements had a  
8 coefficient of determination ( $R^2$ ) of 0.88, with 2D-S IWCs being 82% of CVI IWCs on average.  
9 ~~Moreover, Jackson et al. (2012) showed that the application of habit specific  $m-D$  relationships~~  
10 ~~applied to size/shape distributions in arctic stratocumulus clouds during Indirect and Semi-Direct~~  
11 ~~Aerosol Campaign (ISDAC) over North Slope of Alaska had better agreement with the measured~~  
12 ~~IWC (mean difference is  $\sim 50\%$ ) than did the application of the BL2006 approach to the~~  
13 ~~measured size distributions (mean difference is  $\sim 100\%$ ).~~

14 The methodology for extracting  $m-D$  expressions from 2D-S probe data was first described in  
15 Mitchell et al. (2010), and is briefly described here. The mean ice particle mass is calculated for  
16 each size-bin of the 2D-S probe by dividing the mass concentration in the bin by the measured  
17 number concentration ( $N$ ) in the bin. In this way the mean bin mass is related to bin midpoint  
18 size for each size-bin of the 2D-S probe. The relationship between  $m$  and  $D$  can then be  
19 characterized by plotting mean bin mass against bin midpoint size and fitting the data to an  
20 equation of  $m$  and  $D$ . This was done for the SPARTICUS 2D-S data as described below.

21 The processing of the 2D-S probe SPARTICUS data is described in Mishra et al. (2014). The  
22 original 2D-S data used in this study had been processed by the Stratton Park Engineering  
23 Company (SPEC), Inc. using the M1 technique for measuring ice particle length and area (see  
24 Appendix A in Lawson, 2011). However, the M1 method does not insure that the ice particle is  
25 completely imaged within the sample volume (i.e. that no portion is beyond the photodiode  
26 array), and it uses the length parameter along the direction of travel ( $L_I$ ; see Appendix A) for  
27 maximum dimension. To overcome these drawbacks, the 2D-S data used here were processed  
28 using the newly developed M7 method that insures that the ice particles are completely imaged  
29 within the sample volume (“all-in” criteria), and this method uses the most accurate estimate for  
30 maximum dimension (diameter of circumscribed circle, see Appendix A). Although the sample

1 ~~volume decreases by using the M7 method, such a decrease is not significant determinant. It is~~  
2 ~~shown in the supplement (Figs S1 and S3) that the M1 and M7 methods agree well for both~~  
3 ~~number concentration and area concentration, and with the largest difference between the M1~~  
4 ~~and M7 methods is observed for larger particles ( $D > 300 \mu\text{m}$ ). Moreover, the difference in PSD~~  
5 ~~projected sample area (i.e. extinction) between the M1 and M7 methods does not exceed 5 % and~~  
6 ~~13 % for synoptic and anvil cirrus clouds, respectively (Figs. S2 and S4; see Appendix A for a~~  
7 ~~detailed discussion on the comparison between M1 and M7 methods).~~ The 2D-S data were then  
8 further processed to insure that ice particle mass and projected area did not exceed that of an ice  
9 sphere having a diameter equal to the ice particle maximum dimension.

10 PSDs for each cloud type (synoptic or anvil) were partitioned into temperature intervals of 5 °C  
11 and the PSDs within each temperature interval were averaged to produce 9 mean PSDs (one for  
12 each  $T$ -interval) for synoptic and 9 mean PSDs for anvil ice clouds. This covered a temperature  
13 range of -20° to -65 °C for both synoptic and anvil ice clouds. ~~Although the averaging over~~  
14 ~~temperature intervals results in larger contribution from PSDs with larger IWC, we show that~~  
15 ~~variability in temperature dependent  $m-D$  expressions does not exceed 32 % and has a mean~~  
16 ~~value of 13.48 % (see Sect. 3). Therefore, the contribution from PSDs with larger IWC is not~~  
17 ~~determinative.~~

18 While ice clouds at temperatures warmer than -38 °C might be mixed phase (containing both  
19 liquid water and ice), all PSDs were examined for the presence of liquid water using a  
20 combination of Forward Scattering Spectrometer Probe (FSSP), CPI and 2D-S probes and  
21 relative humidity measurements using the Diode Laser Hygrometer (DLH-) probe. Only PSDs  
22 not associated with evidence of liquid water were used in this analysis as described in Mishra et  
23 al. (2014). Moreover, the PSD selection process identified cloud regions (cloud extinction  $> 0.1$   
24  $\text{Km}^{-1}$ ) where cloud extinction and median mass size were relatively stable (i.e. relatively  
25 invariant with time in a 60-second time period, the cloud extinction and median mass size should  
26 not exceed 2 times their mean and should not be less than 0.4 times their mean), making it  
27 unlikely that liquid water was present. On the other hand, it is possible that some ice particles  
28 sampled were rimed if riming occurred at levels above the level being sampled (considered  
29 unlikely for these temperatures). The number of PSDs found in each temperature interval is  
30 shown for synoptic and anvil ice clouds in Fig. 2.

1 There is an out-of-focus problem affecting the 2D-S measurements of projected area, specifically  
2 for ice particle sizes less than 200  $\mu\text{m}$ . For this size range, many images are out-of-focus with  
3 artificial holes in the middle, so that particles have an appearance similar to doughnuts, and the  
4 projected area of these images is overestimated (Korolev, 2007). Therefore, we used the 2D-S  
5 M7 projected area for ice particle sizes larger than 200  $\mu\text{m}$ , and the CPI projected area for sizes  
6 smaller than 200  $\mu\text{m}$  (see next subsection).

## 7 **2.4 CPI probe**

8 The CPI probe provides digital images of particles that pass through the sample volume at  
9 speeds up to 200  $\text{m s}^{-1}$ . The images were processed via CPIview software to determine ice  
10 particle length, width, projected area, perimeter, and crystal habits, with the resolution of 2.3  $\mu\text{m}$ ,  
11 and for particles in the size range of 10-2000  $\mu\text{m}$  (Lawson et al., 2001). The majority of the CPI  
12 images are in-focus, and a few of them that are out-of-focus are resized smaller using Korolev  
13 focus correction (Korolev et al., 1998). For this reason, CPI projected area is more reliable  
14 compared to the 2D-S for ice particle size less than 200  $\mu\text{m}$  and we used CPI projected area for  
15 sizes less than 200  $\mu\text{m}$ . A discontinuity in projected area is observed between the 2D-S using M1  
16 processing and the CPI for  $D \approx 200 \mu\text{m}$ , with 2D-S area being larger than CPI area by a factor of  
17  $1.54 \pm 0.18$ . There are three factors that contribute to this discrepancy; first, 2D-S M1 for larger  
18 sizes can still be out-of-focus, though less than that for smaller sizes; second, it seems that 2D-S  
19 overestimates size with errors being 10-30%, even when they are in-focus; third, there are  
20 inherent differences between CPI and 2D-S, since they are two different instruments that use two  
21 different measurement techniques. Using the M7 data processing, the 2D-S area is larger than  
22 CPI area by a factor of  $1.30 \pm 0.15$ , showing that M7 and CPI are more self-consistent than M1  
23 and CPI. The number of ice particles imaged by the CPI that were used in this study is 224,719.  
24 Hence, the CPI sampling statistics in each size bin is quite good.

25 The CPI probe does not measure ice particle mass and the BL2006 *m-A* method is not justified  
26 for sizes smaller than 150  $\mu\text{m}$ , because it was derived from a subset of SCPP data with ice  
27 particles having sizes generally greater than  $\sim$  150  $\mu\text{m}$ . Therefore, we developed~~suggest~~ a  
28 methodology (see Appendix B) to estimate mass from the CPI measurements of projected area  
29 and aspect ratio. This new methodology assumes that ice particles with size less than 100  $\mu\text{m}$

1 exhibit hexagonal column geometry. Such a geometrical assumption seems reasonable based on  
2 observations for sizes smaller than 100  $\mu\text{m}$  (see Lawson et al., 2006b, their Figs. 4 and 5). While  
3 other authors have approximated small (e.g.  $D < 50 \mu\text{m}$ ) ice crystals as “droxtals”, Gaussian  
4 random spheres, Chebyshev particles and budding bucky balls (e.g. Um and McFarquhar, 2009),  
5 our study estimates the mass of small ice particles from processed CPI data that contains  
6 measurements of ice particle projected area, length and width. We developed a method that  
7 utilizes all three of these properties to estimate ice particle mass. For the size-range we  
8 considered (20 to 100  $\mu\text{m}$ ), the mean length-to-width ratios were generally  $\leq 1.41 \pm 0.265$ ,  
9 confirming the presence dominance of high-density ice particles, and for such aspect ratios,  
10 hexagonal columns appear to be as good a surrogate of small particle morphology as the other  
11 shapes noted above for estimating ice particle mass. They also provide a convenient means of  
12 using the aspect ratio estimates. As shown in Appendix B, for an aspect ratio of 1.0, the  
13 difference in ice mass between the spherical and hexagonal column assumption is 4%.

14 Um and McFarquhar (2009) studied the radiative properties of small ice particles by assuming  
15 idealized shapes of droxtals, Gaussian random spheres, Chebyshev particles and budding bucky  
16 balls. They investigated particles with  $D < 50 \mu\text{m}$  and area ratio between 0.69 and 0.85, and they  
17 calculated ice particle mass from dimension. However, the purpose of our study is to estimate the  
18 mass of small ice particles from projected area, as Baker and Lawson (2006) showed that  $m-A$   
19 expression is more accurate than  $m-D$  relationship. Moreover, radiative properties of ice particles  
20 (e.g. asymmetry parameter) is strongly dependent on the particle shape (Um and McFarquhar,  
21 2009), whereas estimation of mass and calculation of  $m-D$  expression (as is done in our study) is  
22 shape independent as long as various particle shapes have the same mass ratio. Hexagonal  
23 column geometry but it overestimates the mass for particles with size range of 100-200  $\mu\text{m}$ . This  
24 is not surprising, since this is the size range where ice crystals begin to develop branches or  
25 extensions, becoming more complex and less compact (Bailey and Hallett, 2004; 2009). In other  
26 words, ice particles in this size range have loweress density than particles with  $D < 100 \mu\text{m}$ .  
27 Since the BL2006  $m-A$  expression and the assumption of small ice particles as hexagonal column  
28 approximation for ice particle mass are not valid for  $100 \mu\text{m} < D < 200 \mu\text{m}$ . For this reason, we  
29 used the estimated CPI mass for sizes less than 100  $\mu\text{m}$ , and we did not use any mass estimation  
30 for size range of 100-200  $\mu\text{m}$ . The exception is for  $-65 \text{ }^\circ\text{C} < T \leq -55 \text{ }^\circ\text{C}$ , where we used the  
31 BL2006  $m-A$  method to estimate mass from CPI projected area for  $D$  between 100 and 200  $\mu\text{m}$ .



1 because the number of size bins available for  $D > 200 \mu\text{m}$  is limited (See Fig. 4, where it shows  
2 that data for this coldest temperature interval is available only for  $D < 600 \mu\text{m}$ ). This appears to  
3 be the most accurate approach for this size interval for  $T < -55 \text{ }^\circ\text{C}$ , which is critical for  
4 determining  $m$ - $D$  expressions for these colder temperature intervals. McFarquhar et al. (2013)  
5 discussed that a widely-accepted lower limit is not available for CPI, and it might not be possible  
6 to determine the shape of particles that are smaller than a threshold. They showed that it was  
7 difficult to extract useful information from CPI images for particles with  $D < 35 \mu\text{m}$  for mixed-  
8 phase arctic clouds. In our study, CPI data is used for  $20 \mu\text{m} < D < 100 \mu\text{m}$ . The variables in the  
9 smallest bin-size (10-20  $\mu\text{m}$ ) are not included in our analysis, due to large values of area- and  
10 mass- ratios for this bin-size, indicating ice spheres. Although small particles can be spherical,  
11 there is an abrupt change in both the area- and mass-ratio from 1<sup>st</sup> size-bin to the 2<sup>nd</sup> size-bin; but  
12 for other bin transitions, there is no abrupt change. This might be a size-resolution limitation of  
13 the optics that tends to make the images for the smallest size-bin appear quasi-spherical.

14  
15 McFarquhar et al. (2013) discussed that a widely-accepted lower limit is not available for the  
16 CPI, and they found that it was difficult to extract useful shape information from CPI images for  
17 particles with  $D < 35 \mu\text{m}$  for mixed-phase arctic clouds. However, in our study, shape is not a  
18 concern for the CPI size range we are using ( $20 \mu\text{m} < D < 100 \mu\text{m}$ ) since we assume hexagonal  
19 column geometry and only require length and width measurements, which are estimated for these  
20 sizes from a data processing algorithm developed at SPEC, Inc.

### 23 3 Mass and area relationships

24 Figure S5 shows  $m$ - $D$  and  $A$ - $D$  expressions and data points for all PSDs for all  
25 temperatures ~~dependence~~ considered here. Also shown in this figure is mean and standard  
26 deviation in each size bin. In this way, the natural variability of the  $m$ - $D$  and  $A$ - $D$  PSD  
27 expressions data is presented. While in principle each PSD can be used to produce an  $m$ - $D$  or  $A$ - $D$   
28 expression, in practice only the mean PSDs in  $5 \text{ }^\circ\text{C}$  temperature intervals were used to develop

Formatted: Font: Italic

Formatted: Font: Italic

1 the  $m$ - $D$  and  $A$ - $D$  expressions (explained in Sect. 2.3 and in the Supplement; Fig. S6 figure not  
2 shown). Although the averaging process reduces scatter, the coherency of the curves in Fig. S6 is  
3 somewhat surprising. The natural variability associated with ice particle mass measurements was  
4 minimized in two ways, thus facilitating the curve-fitting process. First,  $m$  was estimated from  
5 the BL2006  $m$ - $A$  relationship for  $D > 200 \mu\text{m}$  (which represents the mean  $m$ - $A$  behavior in a self-  
6 consistent way and thus removes much of the natural variability in  $m$ ), and second, variability  
7 was reduced by averaging the SPARTICUS PSD within each  $5^\circ\text{C}$   $T$  interval, as described in  
8 Sect. 2, producing one mean PSD of number, area and mass concentration for each  $T$  interval.  
9 The latter can be seen in by comparing Figs. S5 and S6. The coherency of this data makes it  
10 amenable to curve-fitting with high precision. McFarquhar et al. (2007) showed that there is  
11 considerable variability in the  $m$ - $D$  expression during the aircraft measurements of stratiform  
12 regions of mesoscale convective systems, and they used a different  $m$ - $D$  expression for each  
13 flight. The variability in our study differs for the reasons stated above. Moreover~~However~~, as we  
14 show further in this section, the variability in  $m$ - $D$  relationship based on 13 flights in synoptic  
15 cirrus clouds during SPARTICUS does not exceed 32-% of the mean bin mass value, having a  
16 mean overall value of 13.48 %.

17 If ice particle morphology does not vary much within the ice cirrus clouds sampled, then Based  
18 on this low variability, we conclude that our  $m$ - $D$  expressions should be is representative of all  
19 ice particles for a given cloud type (continental midlatitude synoptic or anvil cirrus clouds) and  
20 temperature interval. Ice particle images from various types of cirrus clouds tend to support this  
21 assumption, indicating high density, blocky-shaped irregular crystals with some bullet rosettes  
22 and side planes at larger sizes (e.g. Lawson et al. and Baker, 2006b; Baker and Lawson, 2006b).  
23 But if there is a radical departure from this morphology genre and planar ice crystals having low  
24 aspect ratios (i.e. c-axis to a-axis ratio where c-axis is length of the prism face) dominate, our  $m$ -  
25  $D$  expressions could overestimate ice particle mass by a factor of  $\sim 3$  (Lawson, 2016). Such  
26 reasoning may explain findings from Arctic mixed phase clouds, where Jackson et al. (2012)  
27 showed that the application of habit-specific  $m$ - $D$  relationships applied to size/shape distributions  
28 in arctic stratocumulus clouds during Indirect and Semi-Direct Aerosol Campaign (ISDAC) over  
29 North Slope of Alaska had better agreement with the measured IWC (mean difference is  $\sim 50\%$ )  
30 than did the application of the BL2006 approach to the measured size distributions (mean

1 [difference is ~ 100%\). Similar findings from Arctic mixed phase clouds are reported in](#)  
2 [Avramov et al. \(2011, 2022\).](#)

3  
4 A curve fit based on SPARTICUS synoptic mean PSDs for  $-40\text{ }^{\circ}\text{C} \leq T \leq -20\text{ }^{\circ}\text{C}$  is shown in Fig. 3  
5 by the blue curve. This result differs markedly from previous studies where the relationship  
6 between  $\log(m)$  and  $\log(D)$  is linear, rather than a slowly varying curve as shown here. This  
7 finding is due to extending the range of ice particle size to smaller sizes, which was made  
8 possible by using data from the CPI probe. The  $m$ - $D$  line corresponding to ice spheres is shown  
9 for reference since for a given  $D$ , the ice particle mass cannot exceed this value. Also shown is  
10 the curve fit for ice particle mass based on SCPP and CPI  $m$ - $D$  measurements and estimates,  
11 respectively (the black curve). This SCPP data is described in detail in Sec. 4.1, but here it is  
12 sufficient to say that the 827  $m$ - $D$  measurements (with ice particle shapes corresponding to this  
13 temperature range) were grouped into size-intervals and the mean values within each size-  
14 interval are plotted in Fig. 3 (purple filled circles). The close agreement between the blue and  
15 black curves indicates that ice particle masses derived from 2D-S data are adequate surrogates  
16 for the SCPP  $m$ - $D$  measurements. This agreement, mentioned in Sec. 2.1, forms part of the  
17 rationale for this study as described in that section.

18 [Values of mean dimension, mass, and projected area were first calculated for each  \$5\text{ }^{\circ}\text{C}\$   \$T\$](#)   
19 [interval, and plots of  \$m\$ - \$D\$  and  \$A\$ - \$D\$  expressions were provided for each  \$5\text{ }^{\circ}\text{C}\$   \$T\$  interval \(Fig. S6\).](#)  
20 [It was then observed that  \$m\$ - \$D\$  and  \$A\$ - \$D\$  expressions for  \$5\text{ }^{\circ}\text{C}\$   \$T\$  intervals have negligible](#)  
21 [differences within the larger temperature ranges of  \$-40\text{ }^{\circ}\text{C} < T < -20\text{ }^{\circ}\text{C}\$ ,  \$-55\text{ }^{\circ}\text{C} < T < -40\text{ }^{\circ}\text{C}\$ , and](#)  
22  [\$-65\text{ }^{\circ}\text{C} < T < -55\text{ }^{\circ}\text{C}\$ . In order to keep  \$m\$ - \$D\$  and  \$A\$ - \$D\$  expressions as simple as possible without](#)  
23 [losing accuracy, the coefficients of polynomial fits are not provided for each  \$5\text{ }^{\circ}\text{C}\$   \$T\$  interval. To](#)  
24 [minimize variance, the mean PSDs were determined for each of grouped into the above](#)  
25 [mentioned three temperature categories and 2<sup>nd</sup> order polynomial curve fits were calculated for](#)  
26 [each category as shown in Tables 1 and 2. Table 1. The “goodness of fit” is given by the  \$R^2\$  in](#)  
27 [these tables, Table 1, and the number of mean data points used is also indicated.](#)

28 [Values of  \$R^2\$  regarding synoptic  \$m\$ - \$D\$  and  \$m\$ - \$A\$  curve fits for all temperatures \(Fig. S6\) is equal](#)  
29 [to 0.9954 and 0.9924, respectively, which is smaller than  \$R^2\$  for synoptic  \$m\$ - \$D\$  and  \$m\$ - \$A\$  curve fits](#)

1 ~~for each specific temperature range in Tables 1 and 2, respectively. Therefore, G~~ greater accuracy  
2 is obtained by using the fit equation for a specific temperature interval rather than using the fit  
3 equation corresponding to all temperatures sampled. ~~While the temperature-dependent A-D and~~  
4 ~~m-D fits are similar, and the  $R^2$  values for the temperature-independent A-D and m-D fits in Fig.~~  
5 ~~S5 (0.9924 and 0.9954, respectively, based on all temperatures) are similar to those in Tables 1~~  
6 ~~and 2, the actual values predicted by these temperature-dependent fits does render more accurate~~  
7 ~~A and m estimates, as shown in Figs. 4 and S6. Since the fits are similar, a climate model can~~  
8 ~~use these fits without using any smoothing function when crossing temperature boundaries. In~~  
9 ~~fact, this m-D/A-D scheme has been used in a GCM, as described in Eidhammer et al. (2016).~~

Formatted: Font: Italic

Formatted: Font: Times, Italic, Superscript

10  
11 ~~Fontaine et al. (2014) found that it is not proper to employ a single temperature-independent  $m-D$~~   
12 ~~expression for all clouds, because such expression neglects the considerable natural variability of~~  
13 ~~mass as a function of dimension. We showed that it is sufficient to categorize  $m-D$  and  $A-D$~~   
14 ~~expressions into three temperature ranges for a given cloud. Within each of these temperature~~  
15 ~~ranges, negligible differences are observed between  $m-D$  and  $A-D$  expressions corresponding~~  
16 ~~to provided for 5 °C T intervals. Such classification is practical for modeling purposes. The~~  
17 ~~resulting ~~temperature-dependent~~ curve fits are depicted in Fig. 4, where it is shown that for  $T <$~~   
18 ~~-55 °C, the  $m-D$  curves are considerably different for both synoptic and anvil cirrus relative to~~  
19 ~~the warmer temperature intervals. Such feature cannot be seen in temperature-independent  $m-D$~~   
20 ~~and  $A-D$  expressions (Fig. S5). One might ask how a climate model could vary smoothly~~  
21 ~~between the curve fits once a temperature boundary is passed. One way can be defining a short~~  
22 ~~transform range (e.g. 2 to 5 °C) and linearly interpolating the values of  $m$  and  $A$  in this range.~~

23 It is also seen ~~from Fig. 4~~ that the mean dependence of ice particle mass on particle size is not  
24 predicted to vary substantially between ice clouds of different type (i.e. synoptic vs. anvil) for a  
25 given temperature regime. The latter differs from the results of H2010, where they showed that  
26  $m-D$  power laws for anvil ice clouds yield masses about a factor of two larger than for synoptic  
27 ice clouds. It is possible that the similarity in  $m-D$  expressions found here regarding synoptic and  
28 anvil ice clouds is an artifact if ice particle ~~masses/volumes (for bulk ice)~~ for a given  $A$  are quite  
29 different between ~~these~~ cloud types.

1 The 2<sup>nd</sup> order polynomial  $A$ - $D$  curve fits were provided in a similar way that  $m$ - $D$  curve fits were  
 2 obtained, and are shown in [Table 2](#). An example of the mean PSD data and the  
 3 polynomial  $A$ - $D$  curve fit is shown in Fig. 5 for  $-40\text{ }^{\circ}\text{C} < T \leq -20\text{ }^{\circ}\text{C}$ . Again the PSD averaging  
 4 process greatly reduces the spread in area for a given size. More scatter is seen at the largest  
 5 sizes since the size bins here are populated by relatively few ice particles. The line for ice  
 6 spheres indicates the maximum possible projected area for a given  $D$ . For each temperature  
 7 interval, fractional uncertainties for each 2D-S size-bin were calculated as shown in Fig. 6 only  
 8 for the temperature intervals having three or more PSDs. Fractional uncertainties are expressed  
 9 as the  $\sigma$  of projected area divided by the mean projected area for each size-bin midpoint.  
 10 Uncertainties are highly variable and range between 0% and 28% of the mean bin  $A$  value,  
 11 having a mean overall value of 11.0%. Uncertainties tend to be zero for  $D = 10\text{ }\mu\text{m}$  since  
 12 particles in this size bin (5-15  $\mu\text{m}$ ) generally shadow only one pixel in both vertical and time  
 13 (horizontal) dimensions. Similar to Fig. 6, we calculated the fractional uncertainties for the mean  
 14 ice particle mass in each size bin of the measured PSDs (figure not shown). The pattern for the  
 15 mass fractional uncertainties is similar to that for area fractional uncertainties. Mass uncertainties  
 16 range between 0 and 32 % of the mean bin mass, with a mean overall fractional uncertainty mass  
 17 of 13.48 %.

18 It is important to know whether the measured ice particle area and masses are internally  
 19 consistent here since ice cloud properties like  $D_e$  and the mass-weighted fall speed ( $V_m$ ) depend  
 20 on the ice particle  $m/A$  ratio. The maximum value of the  $m/A$  ratio is given by an ice sphere. Thus  
 21 a test for internal consistency is to calculate relative  $m/A$ , which is defined as:

$$R = \frac{\left(\frac{m}{A}\right)_{particle}}{\left(\frac{m}{A}\right)_{sphere}}. \quad (1)$$

22 See Appendix C for the definition of all symbols. This ratio should not exceed a value of 1.0.  
 23 The data used to produce Tables 1 and 2 were tested in this way and this ratio never exceeded a  
 24 value of 1.0. However, when curve fits provided only by 2D-S probe are used, this ratio  
 25 exceeded the value of 1.0 for size less than 20  $\mu\text{m}$  where  $A$  measurements are poorest. An  
 26 example is shown in Fig. 7 for  $-40\text{ }^{\circ}\text{C} < T \leq -20\text{ }^{\circ}\text{C}$ . As shown by Heymsfield et al. (2002) and

1 others, this ratio should increase with decreasing ice particle size, which is also demonstrated  
2 here.

## 3 4 **4 Comparison of curve fits with SCPP measurements of single ice particle mass**

### 5 **4.1 SCPP measurements of ice particle masses characteristic of cold ice clouds**

6 The  $m$ - $D$  expressions in [Table 1](#), based on CPI and 2D-S measurements, are valid to the  
7 extent that the BL2006  $m$ - $A$  relationship is valid at those temperatures and sizes. Testing of the  
8  $m$ - $D$  expression for  $-40\text{ °C} < T \leq -20\text{ °C}$  by using ice particle masses from habits formed in this  
9 same temperature range is pursued in this section.

Formatted: Font: Not Italic, Check spelling and grammar

10 The  $m$ - $D$  relationships developed in the last section are void of uncertainty estimates, which are  
11 needed in remote sensing for estimating the uncertainties of retrieved cloud properties. To  
12 estimate the uncertainty ( $\sigma$ ) associated with the curve fits in [Table 1](#), the field  
13 measurements described in M1990 are used.

Formatted: Font: Not Italic, Check spelling and grammar

14 The distribution of ice particle masses with respect to size is shown in Fig. 8 for the cold-  
15 temperature habits in the SCPP measurements. The laboratory experiments of Bailey and Hallett  
16 (2004; 2009) found that at significant or substantial supersaturations with respect to ice, bullet  
17 rosettes dominate between  $-70\text{ °C}$  and  $-40\text{ °C}$  while complex plate-like crystals (e.g. side planes)  
18 dominate between  $-40\text{ °C}$  and  $-20\text{ °C}$ . At very low supersaturations near ice saturation,  
19 hexagonal columns with aspect ratios near unity were common for  $-70\text{ °C} < T < -20\text{ °C}$ . The  
20 results in Fig. 8 are generally consistent with the laboratory results, with side planes dominating  
21 over bullet rosettes, although short columns were most abundant which suggests low  
22 supersaturations were common in these clouds for  $T < -20\text{ °C}$ . Indeed, low supersaturations  
23 appear to be common in clouds where  $T < -20\text{ °C}$  (C2012). While hexagonal columns are  
24 generally not the dominant ice particle shape for  $T < -20\text{ °C}$ , compact irregular ice particles are  
25 very common and often dominate  $N$  at smaller sizes (Korolev and Isaac, 2003; Lawson et al.,  
26 2006b; [Baker and Lawson, 2006b](#); C2012). The similarity between the hexagonal column  $m$ - $D$   
27 expression and the C2012  $m$ - $D$  expression in Fig. 1 suggests short hexagonal columns may serve  
28 as a proxy for compact irregular ice. Ice particles classified as unrimed having these shapes were

1 used in Fig. 8, although some light riming is possible. The three main categories of ice particle  
2 shape are color-coded in Fig. 8, with columnar ice particles more common at small-to-  
3 intermediate sizes, side plane type ice particles more common at intermediate-to-large sizes, and  
4 bullet rosettes more common at intermediate sizes. The  $m$ - $D$  curve fit, based on CPI and SCPP  
5 measurements, is from [Table 1](#) for synoptic ice clouds for  $-40\text{ }^{\circ}\text{C} < T \leq -20\text{ }^{\circ}\text{C}$ .

Formatted: Font: Not Italic, Check spelling and grammar

6 Also shown are the recently published  $m$ - $D$  power law relationships of C2012 and H2010 that  
7 were obtained from synoptic ( $-60\text{ }^{\circ}\text{C} < T < -20\text{ }^{\circ}\text{C}$ ) and from both synoptic and anvil ( $-60\text{ }^{\circ}\text{C} < T$   
8  $< 0\text{ }^{\circ}\text{C}$ ) ice clouds, respectively. These relationships are plotted over the size range used to  
9 produce them. The C2012 relationship consists of two lines and follows the curve fit remarkably  
10 well for  $D > 100\text{ }\mu\text{m}$ , with differences never exceeding 50%. The H2010 relationship consists of  
11 a single line and also approximates the curve fit well, except for  $D < 100\text{ }\mu\text{m}$  and  $D > 1000\text{ }\mu\text{m}$   
12 where differences can reach about 100%.

13 [Figure 9](#) shows a polynomial curve fit based on mass estimates from the 2D-S (M7  
14 processing) and CPI probes for sizes greater than  $200\text{ }\mu\text{m}$  and less than  $100\text{ }\mu\text{m}$ , respectively.  
15 Also shown is SCPP data where the ice particle measurements were binned into size intervals of  
16  $100\text{ }\mu\text{m}$  between  $100$  and  $1000\text{ }\mu\text{m}$ , with subsequent intervals of  $200$ ,  $200$ ,  $400$ ,  $600$ ,  $600$  and  
17  $1000\text{ }\mu\text{m}$  (up to  $4\text{ mm}$ ) at larger sizes to provide adequate sampling statistics. The  $\sigma$  within each  
18 size interval was calculated for  $m$  and  $D$  as shown by the vertical and horizontal red bars,  
19 respectively. The intersection point marks the mean value for  $m$  and  $D$  in each interval. The  $m$ - $D$   
20 curve fit for SPARTICUS synoptic ice clouds for  $-40\text{ }^{\circ}\text{C} < T \leq -20\text{ }^{\circ}\text{C}$  is extrapolated to  $4\text{ mm}$  in  
21 Fig. 9 for comparison with the masses and sizes of these 827 ice particles sampled during SCPP.  
22 In this way, the SPARTICUS measurements roughly coincide with the temperatures of origin of  
23 these SCPP cold-habit ice particles. Although the BL2006  $m$ - $A$  expression was derived from a  
24 subset (865 ice particles) of the 3-year SCPP field study (4869 ice particles), a detailed  
25 comparison of the subset of 827 cold-habit ice particles used here and the BL2006 subset  
26 revealed that only 17.5% of the ice particles were common to both subsets. Thus, a comparison  
27 of an  $m$ - $D$  expression based on SPARTICUS data (derived from the BL2006  $m$ - $A$  expression)  
28 with the cold-habit  $m$ - $D$  measurements from SCPP is still a meaningful comparison. It is seen in  
29 Fig. 9 that the SPARTICUS curve fit is well within the  $\sigma$  values of SCPP mass for all size  
30 intervals and is often close to the mean  $m$  values, except for the largest size-bin having a



1 relatively small sample size. The same is true for the C2012  $m$ - $D$  expression when it is extended  
2 to larger ice particle sizes.

3 Getting still more quantitative, the percent difference of the SCPP cold habit mean mass for a  
4 given size interval was compared with the corresponding ice particle mass from the  
5 SPARTICUS curve fit. In other words, the percent difference is calculated as

6  $100 \times (m_{\text{SCPP}} - m_{\text{SPARTICUS}}) / [(m_{\text{SCPP}} + m_{\text{SPARTICUS}}) / 2]$  for each size bin (figure not shown). Percent

7 differences are less than 53% in all size bins, and the mean percent difference for all size-bins

8 was 28%. Note that percent difference is calculated on the normal scale, and not on the

9 logarithmic scale. Given the natural variability observed for ice particle masses, this level of

10 agreement is considered good. Moreover, the  $m$ - $D$  expressions from two completely independent

11 studies, C2012 and H2010, conform closely to the SPARTICUS curve fit and the mean cold-

12 habit (i.e. SCPP)  $m$  values. The convergence in agreement of the SPARTICUS curve fit with the

13 cold-habit SCPP  $m$ - $D$  measurements, the C2012 study and the H2010 study suggest that the

14 SPARTICUS  $m$ - $D$  curve fit is a reasonable representation of ice particle mass over the particle

15 size range considered here. It uses the BL2006  $m$ - $A$  relationship to estimate  $m$  for  $D \geq 200 \mu\text{m}$

16 and our CPI  $m$ - $A$  method for  $D \leq 100 \mu\text{m}$ , and its agreement with the SCPP cold-habit  $m$ - $D$

17 measurements validates its use up to 4 mm for  $-40 \text{ }^\circ\text{C} < T \leq -20 \text{ }^\circ\text{C}$ .

## 18 4.2 Extension to colder temperatures

19 As postulated in Sect. 2, given a validated  $m$ - $D$  expression from SPARTICUS and SCPP data

20 between  $-40$  and  $-20 \text{ }^\circ\text{C}$ , this methodology of obtaining  $m$ - $D$  expressions from SPARTICUS data

21 should be appropriate at colder temperatures if ice particle shape does not significantly change.

22 Here we use the ice particle  $A_r$  as a proxy for ice particle shape. The mean ice particle  $A_r$  for each

23 size-bin is shown for each  $5 \text{ }^\circ\text{C}$  temperature interval in Figs. 10 and 11 for synoptic and anvil

24 cirrus, respectively. Values of  $A_r$  are similar among all temperature intervals excepting those for

25  $T \leq -55 \text{ }^\circ\text{C}$ . For  $D > 60 \mu\text{m}$ , these two coldest intervals exhibit  $A_r$  less than that for  $T > -55 \text{ }^\circ\text{C}$  in

26 both synoptic and anvil ice clouds.

27 For purposes of calculating PSD  $A$ ,  $m$ , and radar reflectivity ( $Z$ ), the  $A_r$  changes at these larger

28 sizes are considered more critical than the  $A_r$  changes at smaller sizes. It is therefore argued that

Field Code Changed

1 for these applications, the noted methodology of obtaining  $m$ - $D$  and  $A$ - $D$  expressions from  
 2 SPARTICUS data should be appropriate at colder temperatures down to  $-55$  °C. For  $T \leq -55$  °C,  
 3 it appears that ice particle shape changes, and it is possible that the ice particle geometry changes  
 4 in such a way that the BL2006  $m$ - $A$  expression is no longer valid. For example, if the BL2006  $m$ -  
 5  $A$  expression implicitly assumes relatively compact ice particles growing in 3 dimensions, and  
 6 the ice particle shape changes to planar crystals with 2-dimensional growth dominating, then the  
 7 BL2006  $m$ - $A$  expression may perform poorly. We report  $m$ - $D$  results for these coldest  
 8 temperatures (Table 1), but with the caveat that these  $m$ - $D$  expressions are highly uncertain.  
 9 Additional research is needed to test these results. Moreover, this study addresses only mid-  
 10 latitude synoptic and anvil ice clouds over land, and results may have been different if marine  
 11 anvil cirrus, orographic cirrus and/or Arctic ice clouds were considered.

12

### 13 5 Uncertainties in $m$ - $D$ and $A$ - $D$ expressions

14 Conventional  $m$ - $D$  and  $A$ - $D$  expressions use power law relationships of the form:

$$m = \alpha D^\beta \quad (2)$$

$$A = \gamma D^\delta \quad (3)$$

Field Code Changed

15 to estimate ice particle mass and projected area, where  $\alpha$ ,  $\beta$ ,  $\gamma$  and  $\delta$  are constants. This study  
 16 indicates that these terms should not be constants over all ice particle sizes, but that they can be  
 17 approximated as constants over a range of particle size with good accuracy. The 2<sup>nd</sup> order  
 18 polynomials used in this study have the form:

$$\ln x = a_0 + a_1 \ln D + a_2 (\ln D)^2 \quad (4)$$

19 where  $x$  is either  $m$  or  $A$ , and  $a_0$ ,  $a_1$  and  $a_2$  are constants. Differentiating Eq. (4) with respect to  
 20  $\ln(D)$  gives the slope of this curve which is  $\beta$  for the mass case:

$$\frac{\partial(\ln m)}{\partial(\ln D)} = \beta = a_1 + 2a_2 \ln D \quad (5)$$

1 Thus,  $\beta$  is a function of  $D$ , and for a given  $D$ ,  $\alpha$  can be solved for by equating the  $m$ - $D$  power law  
2 (Eq. 2) with polynomial fit (Eq. 4):

$$\alpha = \frac{\exp[a_0 + a_1 \ln D + a_2 (\ln D)^2]}{D^\beta}. \quad (6)$$

3 The same approach is used to solve for  $\delta$  and  $\gamma$  for a given  $D$ . Uncertainties for the  $m$ - $D$  and  $A$ - $D$   
4 polynomial fit expressions can be characterized by estimating  $\sigma$  for  $\alpha$  and  $\gamma$  using field  
5 observations of  $m$  and  $A$ , and estimating  $\sigma$  for  $\beta$  and  $\delta$  using selected values of  $D$  in the fit  
6 equations. This is possible due to the relatively low uncertainty in  $\beta$  and  $\delta$ , as described below.

### 7 **5.1 Uncertainties in the exponent of power law expressions**

8 Values of  $\beta$  and  $\delta$  are evaluated at five ice particle sizes and for all temperature intervals sampled  
9 for synoptic and anvil ice clouds, and are shown in Tables 3-6. For the two coldest temperature  
10 intervals, values are not shown for the two largest size categories since PSD did not extend to  
11 these sizes at these temperatures. The mean and  $\sigma$  for  $\beta$  are calculated for each of the five ice  
12 particle sizes selected. Then, the mean uncertainty is expressed as a percent for the fraction mean  
13  $\sigma/\text{mean } \beta$  that is averaged over all 5 selected sizes. This mean fractional uncertainty is the final  
14 uncertainty estimate for  $\beta$  and  $\delta$  that can be applied for any size and temperature range. A key  
15 finding is that mean uncertainties for  $\beta$  do not exceed 9.1% and mean uncertainties for  $\delta$  do not  
16 exceed 8.5%. This indicates that most of the scatter in measurements of ice particle mass and  
17 area can be attributed to uncertainties in  $\alpha$  and  $\gamma$ , respectively.

18 Another interesting feature of Tables 3-6 is the evolution of  $\beta$  and  $\delta$  with size. At the smallest  
19 sizes, ice particles tend to be quasi-spherical or isometric (Korolev and Isaac, 2003), with  $\beta$  and  $\delta$   
20 approaching values of 3 and 2, respectively, with decreasing size. As ice particles grow in size,  
21 they become more complex, often displaying branches in 3 dimensions (e.g. bullet rosettes and  
22 side planes). This produces less mass per unit length, and  $\beta$  and  $\delta$  decrease. In Tables 5 and 6,  $\delta$   
23 is slightly greater than 2.00 (the maximum theoretical value) at the smallest size for some  
24 temperature intervals. This is likely due to inaccuracies in CPI projected area measurements at  
25 small sizes and an artifact of the curve-fitting process.

## 1 5.2 Uncertainties in prefactors of power law expressions

2 Figure 9 shows  $\sigma$  for SCPP  $m$  for each size interval. Since changes in  $\beta$  account for a relatively  
3 small portion of this uncertainty, to a first approximation we can attribute all this uncertainty to  
4  $\alpha$ . The percent uncertainty averaged over all sizes is calculated as the mean value of the  
5 fractional uncertainty of each size interval ( $\sigma/\text{size-bin mean value}$ ), and is equal to  $\pm 54.4\%$  for  
6 the mass  $\sigma$  values in Fig. 9. This is our estimate for the mean fractional  $\sigma$  for  $\alpha$  for all ice clouds.

7 A similar analysis is needed for ice particle projected area, and for that we turn to the fractional  
8 uncertainty calculations shown in Fig. 6. The mean percent uncertainty for  $\gamma$  based on Fig. 6 is  $\pm$   
9 11.2%.

10 These mean  $\sigma$  values for  $\alpha$  and  $\gamma$  should be representative  $\sigma$  estimates for the  $m$ - $D$  and  $A$ - $D$   
11 expressions reported in this paper. Moreover, these uncertainties should be useful in  
12 characterizing the uncertainties of retrieved ice cloud properties in various retrieval algorithms.

13

## 14 6 Application to cloud modeling

### 15 6.1 Methodology

16 In regional and global climate models, the microphysical factors most affecting the cloud  
17 radiative forcing and feedback from ice clouds are the ice water path (IWP), the  $D_e$  and the  $V_m$ .  
18 While ice cloud optical properties are a strong function of  $D_e$ , the ice cloud lifetime, coverage  
19 and IWP are strong functions of  $V_m$  (Sanderson et al., 2008; Mitchell et al., 2008). Both  $D_e$  and  
20  $V_m$  primarily depend on the ice particle  $m/A$  ratio. In many climate models, the  $D_e$  estimated for  
21 the prediction of ice optical properties is not the  $D_e$  predicted from the cloud microphysics,  
22 introducing an inconsistency between the microphysics and radiation modules of the climate  
23 model (Baran, 2012). Moreover,  $V_m$  and  $D_e$  are generally not treated consistently in terms of the  
24  $m/A$  ratio in nearly all cloud, weather prediction and climate models. Rather,  $V_m$  is generally  
25 predicted from a power law of the form  $V = a_v D_o^{b_v}$  where  $a_v$  and  $b_v$  are constants and  $D_o$  is a  
26 characteristic dimension of the ice PSD (e.g. Morrison and Gettelman, 2008). This can result in  
27 non-physical behavior that substantially affects the cloud radiative forcing.

Field Code Changed

Field Code Changed

1 These model inconsistencies can be easily rectified by recognizing that ice microphysical and  
2 optical properties rest on some fundamental assumptions regarding  $m$  and  $A$ ; namely the  $m$ - $D$  and  
3  $A$ - $D$  power laws (Eqs. 2 and 3). By applying these relationships consistently throughout a climate  
4 model (e.g. to predict both  $D_e$  and  $V_m$ ), self-consistency can be achieved.

5 While these relationships are commonly used in climate models, it is sometimes not recognized  
6 that such power laws are only valid over a limited range of  $D$ . ~~(examples include Fig. 1 and For~~  
7 ~~the specific ranges of various power laws, see Sect. 1 and also Table 1 in Mitchell 1996).~~ To  
8 address this by using 2<sup>nd</sup> order polynomials poses a conundrum since many physical processes  
9 are analytically expressed by integrating  $m$ - $D$  and  $A$ - $D$  power laws over the PSD. Thus, using 2<sup>nd</sup>  
10 order polynomial fits may pose a quantum leap in model complexity. To avoid this problem, we  
11 propose the following treatment of  $m$ - $D$  and  $A$ - $D$  expressions.

12 To make this treatment practical for climate modeling, a procedure was developed that assumes  
13 advanced approximate knowledge of the PSD dimension of interest ( $D_i$ ). For example, if the ice  
14 cloud microphysical properties and processes being calculated are most relevant to the PSD mass  
15 moment (i.e. IWC), then the median mass dimension ( $D_m$ ; the particle size dividing the PSD  
16 mass into equal parts) is the  $D_i$ . Fortunately, 2-moment microphysical schemes in climate models  
17 provide such knowledge since the slope parameter ( $\lambda$ ) of the PSD is predicted. The  $m$ - $D$   
18 exponent  $\beta$  is generally near 2 for  $D > 150 \mu\text{m}$  (see ~~Table 3~~ Table 3 and 4) and tends to be  $\sim 2.7$   
19 for  $D \sim 50 \mu\text{m}$ . Thus,  $D_m$  can be approximated using an exact expression from Mitchell (1991):

$$D_m = \frac{\beta + \nu + 0.67}{\lambda} \quad (7)$$

20 where it assumes that a gamma function describes the PSD, given as:

$$N(D) = N_o D^\nu \exp(-\lambda D) \quad (8)$$

21 and  $\nu$  is the PSD dispersion parameter (often assumed to be constant) and  $N_o$  depends on  $N$  or the  
22 IWC. Similarly, ~~Table 5~~ Table 5 and 6 show  $\delta$  is near 1.7 for  $D > 150 \mu\text{m}$  and is close to 2.0 for  $D$   
23  $\sim 50 \mu\text{m}$ . If the PSD area moment is most relevant to model calculations (e.g. ice optical  
24 properties), then  $D_i$  is the median area dimension ( $D_A$ ):

Formatted: Font: (Default) Times New Roman

Formatted: Font: (Default) Times New Roman, Not Italic,  
Check spelling and grammar

Formatted: Font: Not Italic, Check spelling and grammar

$$D_A = \frac{\delta + \nu + 0.67}{\lambda}. \quad (9)$$

1 Moreover, if the PSD radar reflectivity moment is most relevant to model calculations, then  $D_i$  is  
 2 the median radar reflectivity dimension ( $D_Z$ ):

$$D_Z = \frac{2\beta + \nu + 0.67}{\lambda}. \quad (10)$$

3 When addressing ice nucleation, either the mean size ( $\bar{D}$ ) or the median number concentration  
 4 dimension ( $D_N$ ) may be used:

$$D_N = \frac{\nu + 0.67}{\lambda}. \quad (11)$$

5 Because  $\beta$  and  $\delta$  vary slowly with respect to  $D$ ,  $D_i$  can be well approximated for a given  
 6 temperature regime by evaluating  $\beta$  and  $\delta$  at  $D = 500 \mu\text{m}$ , and then solving for  $D_i$ . An iterative  
 7 procedure can yield exact solutions for  $\beta$ ,  $\delta$ ,  $\alpha$ ,  $\gamma$ , and  $D_i$  using the following steps: (a)  $\beta$ ,  $\delta$ ,  $\alpha$ ,  $\gamma$   
 8 are evaluated at  $D = 500 \mu\text{m}$  using Eqs. (5)(5) and (6)(6). (b)  $D_i$  is calculated as indicated above,  
 9 along with any PSD properties of interest such as  $D_e$  or  $V_m$ . (c)  $\beta$ ,  $\delta$ ,  $\alpha$ ,  $\gamma$  are recalculated based on  
 10  $D_i$  and the appropriate curve fit. (d) These updated values are then used to recalculate  $D_i$ , along  
 11 with any PSD properties of interest. A single iteration yields  $D_A$ ,  $D_m$ ,  $\delta$  and  $\beta$  within 0.5%, 1.5%,  
 12 0.6% and 1.9% of their exact values, respectively. Thus, only one iteration is needed for most  
 13 applications since changes in  $D_i$  are primarily due to changes in  $\lambda$ .

14 Calculating  $D_i$  is a means of approximating the size range relevant to the ice properties or  
 15 processes being determined. To calculate  $D_i$ ,  $\lambda$  must be supplied by the cloud resolving model. In  
 16 the Community Atmosphere Model version 5 (CAM5; Gettelman et al., 2010),  $\lambda$  is obtained  
 17 from the ratio  $IWC/N$  where the PSD is expressed as a gamma function, as shown by Eq. (8)(8).  
 18 Solving for  $\lambda$ ,

$$\lambda = \left[ \frac{\alpha \Gamma(\beta + \nu + 1) N}{\Gamma(\nu + 1) IWC} \right]^{\frac{1}{\beta}} \quad (12)$$

1 where  $\Gamma$  denotes the gamma function. Although the dependence of  $\lambda$  on  $\alpha$  and  $\beta$  complicates  
2 matters, Eq. (12)(42) can be solved iteratively using the following steps: (a)  $\lambda$  is initially  
3 estimated by evaluating  $\alpha$ ,  $\beta$ ,  $\gamma$  and  $\delta$  at  $D = 500 \mu\text{m}$  for a given  $N$  and IWC using Eqs. (5)(5),  
4 (6)(6), and (12)(42). (b) These values of  $\lambda$ ,  $\delta$  and  $\beta$  are then used to calculate  $D_i$  as described  
5 above. (c) The revised  $D_i$  value is then used in Eqs. (5)(5) and (6)(6) to generate revised values  
6 for  $\beta$ ,  $\alpha$ ,  $\delta$ , and  $\gamma$ , which are then used in Eq. (12)(42) to revise  $\lambda$ . (d) This revised  $\lambda$  revises  $D_i$ ,  
7 and the cycle repeats but entering at step (c); subsequent iteration involves only steps (c) and (d).  
8 For solving Eq. (12)(42),  $D_i$  is equal to  $D_m$  since the derivation of Eq. (12)(42) reveals that  $\alpha$  and  
9  $\beta$  are associated with the IWC PSD moment. Again, this approach is feasible since changes in  $\lambda$   
10 primarily result from changes in  $N$  and IWC. The  $\lambda$  produced from a single iteration has an error  
11 of 1.2% when  $\bar{D} = 14 \mu\text{m}$  (in the size regime where errors are greatest).

12 Alternatively,  $\lambda$  can be obtained using a look-up table (LUT) that relates  $\lambda$  to  $N$  and IWC for all  
13 relevant combinations of  $\alpha$  and  $\beta$ . The LUT can be produced through the iterative process  
14 described above.

15 While the resulting  $m$ - $D$  or  $A$ - $D$  power law is only valid over a limited size range, since it is  
16 centered on  $D_i$ , it should be sufficiently accurate for calculating various ice microphysical  
17 properties (some used to calculate optical properties) such as IWC,  $D_e$ ,  $V_m$ ,  $Z$  or ice nucleation  
18 rates. This also allows many microphysical rates and quantities to be represented analytically in a  
19 simple way since power law expressions are easily integrated over the PSD, and are thus  
20 compatible with climate model architectures. In this way, the  $m$ - $D$  and  $A$ - $D$  power laws become a  
21 function of the  $\lambda$ . This should significantly improve the accuracy of predicting cloud  
22 microphysical and radiative properties and cloud radiative forcing in general, and also unify  
23 microphysical and radiative processes under a common treatment of ice particle area and mass. It  
24 is noteworthy that a common data set is used to derive these  $m$ - $D$  and  $A$ - $D$  expressions, making  
25 them self-consistent (generally not achieved in past studies).

## 26 **6.2 Impact on calculations of ice particle $N$ , $D_e$ , and $V_m$**

27 First in this subsection, these quantities are calculated in the standard way, assuming constant  
28 values of  $\alpha$ ,  $\beta$ ,  $\gamma$  and  $\delta$ , and then they are calculated using the methodology explained in Sect. 6.1,



1 where  $\alpha$ ,  $\beta$ ,  $\gamma$  and  $\delta$  exhibit a weak dependence on  $D$ . An exponential PSD is assumed ( $\nu = 0$ ), and  
2  $\alpha$ ,  $\beta$ ,  $\gamma$  and  $\delta$  are based on the warmest temperature regime ( $-40\text{ °C} < T \leq -20\text{ °C}$ ).

3  $N$  can be calculated by manipulating Eq. (12)(12). Figure 12 shows the calculation of  $N$   
4 as a function of the  $\bar{D}$  for constant  $\alpha$  and  $\beta$  (black line), variable  $\alpha$  and  $\beta$  (blue curve), and  $\alpha$  and  $\beta$   
5 based on C2012 (purple line). Note that  $\bar{D} = (\nu + 1) / \lambda$ . Also shown is the dependence of  $N$   
6 on  $\bar{D}$  when the CAM5 values of  $\alpha$  and  $\beta$  for cloud ice are used (CAM5 assumes ice spheres  
7 having a density of  $0.5\text{ g cm}^{-3}$ ). The differences in  $N$  for constant, variable, and C2012  $\alpha$  and  $\beta$   
8 are within about a factor of 2, and the discontinuity in the C2012 curve is due to an abrupt  
9 change in the  $m$ - $D$  expression at  $D = 70\text{ }\mu\text{m}$ . This discontinuity highlights the drawback of using  
10 multiple  $m$ - $D$  or  $A$ - $D$  power laws in climate models and the need for a single  $m$ - $D$  or  $A$ - $D$  curve  
11 fit. There is a large underestimation for  $N$  (relative to other curves shown) calculated using the  
12 CAM5 values of  $\alpha$  and  $\beta$ . This underscores the danger of representing ice particles as spheres in  
13 climate models.

14 Based on Foot (1988) and Mitchell (2002),  $D_e$  is defined as:

$$D_e = \frac{3IWC}{2\rho_i A_t} \quad (13)$$

15 where  $A_t$  is the total PSD projected area and  $\rho_i$  is bulk density of ice. Most climate models use  
16  $D_e$  to predict ice cloud optical properties. Assuming an analytical PSD given by Eq. (8)(8) and  
17 applying Eqs. (2)(2) and (3)(3),  $D_e$  is given as:

$$D_e = \frac{3\alpha\Gamma(\beta + \nu + 1)}{2\rho_i\gamma\Gamma(\delta + \nu + 1)} \lambda^{\delta - \beta}. \quad (14)$$

18 From Eq. (14)(14), it is clear that  $D_e$  strongly depends on  $\alpha$ ,  $\beta$ ,  $\gamma$  and  $\delta$ . When calculating  $D_e$  for  
19 variable values of  $\alpha$ ,  $\beta$ ,  $\gamma$  and  $\delta$ ,  $\alpha$  and  $\beta$  were determined from  $D_m$  (associated with IWC) while  $\gamma$   
20 and  $\delta$  were determined from  $D_A$  (associated with PSD projected area). Figure 13 shows  
21 that significant differences exist between  $D_e$  based on constant and variable values of  $\alpha$ ,  $\beta$ ,  $\gamma$  and  
22  $\delta$ , especially at  $\bar{D} < 50\text{ }\mu\text{m}$  and  $\bar{D} > 500\text{ }\mu\text{m}$ ; and at these size ranges,  $D_e$  based on constant  $\alpha$ ,

Field Code Changed

Formatted: Font: Not Italic

1  $\beta$ ,  $\gamma$  and  $\delta$  is greater than  $D_e$  based on variable ones. Also shown is  $D_e$  based on  $\alpha$ ,  $\beta$ ,  $\gamma$  and  $\delta$   
2 values assumed for cloud ice in CAM5, which shows dramatic overestimation compared to two  
3 other methods, and these changes are greatest when  $\bar{D} > 100 \mu\text{m}$ .

4  $V$  is another property that depends on the  $m/A$  ratio. The method of Heymsfield and Westbrook  
5 (2010) is sometimes used to predict  $V$  where  $V$  is predicted from the Best number ( $X$ ), defined as:

$$X = \frac{\rho_{air}}{\eta^2} \frac{8mg}{\pi A_r^{0.5}} \quad (15)$$

6 where  $\rho_{air}$  is the density of air,  $\eta$  is the dynamic viscosity, and  $g$  is the gravitational constant. The  
7 PSD  $V_m$  was calculated from  $D_m$  using the Heymsfield-Westbrook scheme, where  $\alpha$ ,  $\beta$ ,  $\gamma$  and  $\delta$   
8 may be fixed or variable. [Figure 14](#) denotes that considerable differences can exist for  
9  $V_m$  at  $\bar{D} < 20 \mu\text{m}$  and  $\bar{D} > 500 \mu\text{m}$ , depending on whether  $V_m$  was based on fixed or variable  
10 values of  $\alpha$ ,  $\beta$ ,  $\gamma$  and  $\delta$ . Note that  $V_m$  based on constant  $\alpha$ ,  $\beta$ ,  $\gamma$  and  $\delta$  is greater than  $V_m$  based on  
11 variable ones. In addition,  $V_m$  was calculated for the fixed values of  $\alpha$ ,  $\beta$ ,  $\gamma$  and  $\delta$  used in CAM5  
12 for cloud ice. In this case, errors in  $V_m$  are much greater (with greatest error seen at  $\bar{D} > 100$   
13  $\mu\text{m}$ ), again underscoring potential errors that may result by assuming spheres for ice particles.

Formatted: Font: Not Italic

14

## 15 7 Conclusions and Summary

16 The findings presented here constitute a fundamental shift in our way of representing ice particle  
17 mass and projected area in atmospheric models and remote sensing algorithms. Rather than  
18 having a multitude of  $m-D$  and  $A-D$  power law expressions for different ice particle shapes, size  
19 ranges, temperature regimes and/or cloud types, several 2<sup>nd</sup> order polynomial fits may suffice for  
20 ice clouds at different temperature intervals, perhaps only 3 for each cloud type (see Fig. 4).  
21 From these fit equations, any number of  $m-D$  and  $A-D$  power law expressions can be derived to  
22 address the ice particle size range of interest.

23 The  $m-D$  curves developed here appear representative of ice particle masses in ice clouds for  $T <$   
24  $-20 \text{ }^\circ\text{C}$  since they are in good conformity with  $m-D$  power laws developed under similar  
25 conditions in recent studies as shown in Figs. 8 and 9. Moreover, they conform well to the

1 masses of ice particle shapes commonly found between -20 and -40 °C, although measured at  
2 ground level during SCPP.

3 Ice particle projected area was directly measured using the 2D-S and CPI probes during  
4 SPARTICUS. The mass of ice particles originating between -20 °C and -40 °C was directly  
5 measured for synoptic ice clouds (i.e. SCPP data); otherwise it was calculated from projected  
6 area using the BL2006  $m$ - $A$  relationship for  $D > 200 \mu\text{m}$  or it was calculated from CPI  
7 measurements for  $D < 100 \mu\text{m}$  using our new method (see Appendix B). Since the SCPP  $m$ - $D$   
8 measurements were consistent with the 2D-S  $m$ - $D$  estimates between -20 and -40 °C, the  
9 resulting  $m$ - $D$  and  $A$ - $D$  expressions were essentially developed from the same SPARTICUS data  
10 set, containing 158 PSDs for synoptic ice clouds and 107 PSDs for anvil ice clouds. Therefore,  
11 the  $m$ - $D$  and  $A$ - $D$  expressions should be self-consistent, as confirmed in Fig. 7. Three  
12 temperature regimes were defined such that, within a given regime, the variance in  $m$  or  $A$  for a  
13 given  $D$  was minimal, and a couple of  $m$ - $D$  and  $A$ - $D$  2<sup>nd</sup> order polynomial fits was determined for  
14 each temperature regime and for each cloud type; synoptic and anvil. The  $m$ - $D$  and  $A$ - $D$   
15 expressions for synoptic and anvil ice clouds were very similar within each temperature regime.

16 A methodology was developed for extracting  $m$ - $D$  and  $A$ - $D$  power laws from these 2<sup>nd</sup> order  
17 polynomial fits that are appropriate to the ice particle size range (e.g. PSD moments) of interest.  
18 In this way, these polynomial fits can easily be applied to cloud and climate models without  
19 much interference in model architecture (since many of these models have their cloud  
20 microphysics formulated in terms of these  $m$ - $D$  and  $A$ - $D$  power laws). The prefactor and  
21 exponent for these power laws vary slowly with  $D$ , and significantly greater accuracy can be  
22 achieved when calculating cloud properties from these fit equations relative to power laws  
23 having a fixed prefactor and exponent. Treating ice particles as spheres in cloud models was  
24 shown to produce large microphysical errors.

25 Remote sensing algorithms that retrieve cloud properties strongly depend on  $m$ - $D$  and  $A$ - $D$  power  
26 laws, with confidence levels for the retrieved cloud property often largely determined by the  
27 uncertainty associated with these power laws (e.g. Delanoë and Hogan, 2010). This study has  
28 quantified these uncertainties and has found that most of the uncertainty lies in the prefactor.  
29 Application of these  $m$ - $D$  and  $A$ - $D$  uncertainties to the remote sensing of ice cloud properties will

1 likely improve the confidence of such retrievals. This study was focused only on mid-latitude  
2 continental ice clouds, and not on marine anvil or synoptic cirrus, orographic cirrus and/or Arctic  
3 ice clouds. Application of BL2006 (which is based on a subset of SCPP data from mid-latitude  
4 continental clouds) to tropical anvil clouds produced IWC with only ~ 18% difference compared  
5 to measured bulk IWC (Lawson et al. 2010). However, use of BL2006 in arctic mixed phase  
6 clouds leads to IWC ~ 100% larger than measured bulk IWC (Jackson et al. 2012). The results  
7 might be different for these clouds, and aAdditional research is required to apply and test the  
8 approach introduced in this study in different environments.

9

10

## 11 Appendix A: Comparison between M1 and M7 methods for 2D-S probe

12 There are various methods to process 2D-S data, such as M1, M2, M4, and M7 methods  
13 (Lawson, 2011). Explanation and comparison of all these methods are beyond the scope of this  
14 paper. The M1 method was originally used in this study, but the newly developed M7 method  
15 ~~was replaced~~ the M1 method for two main reasons. First, the M1 and M7 methods differ on the  
16 measurement of particle dimensions, as is shown in Fig. A1. Two ice particles with different  
17 shapes are shown to give the reader an idea of how the different length scales (L1, L4, and  
18 MaxLength) for different ice particle shapes are measured and calculated by the 2D-S and its  
19 respective software. The horizontal direction represents the direction of particle travel into the  
20 2D-S probe and is sometimes referred to as the time dimension. The M1 method ~~calculates~~uses  
21 maximum dimension as the dimension along the direction of travel (length scale  $L1$ ) ~~as the~~  
22 ~~maximum dimension~~, whereas the M7 method ~~calculates~~uses the maximum dimension of the  
23 particle 2D image as the diameter of a circumscribed circle (length scale  $MaxLength$ ). Therefore,  
24 M7 method provides a more realistic measurement of maximum dimension, compared to many  
25 other studies that used  $L1$ . Note that length scale  $L4$  in Fig. A1 is not the particle “height” range  
26 (projected along the vertical photodiode array) during its entire transit time through the sample  
27 volume; rather it is a measure of particle width at a given instant. Moreover,  $L4$  is the maximum  
28 value of all these time-slices (i.e. widths) measured. Note that Length scale  $L4$  in Fig. A1 is not  
29 exactly the projected dimension along the vertical photodiode array. Indeed, is determined from

Formatted: Font color: Auto

Formatted: Font color: Auto

Formatted: Font color: Auto

1 ~~the maximum number of shadowed photodiodes (vertical array) at any given instant is used to~~  
2 ~~derive  $L_1$  as the measure of particle width.~~

Formatted: Font color: Auto

3  
4 Second, the M1 and M7 methods are distinct in the treatment of particles that intersect the edges  
5 of the 2D-S field of view. Using the M1 method, all particles are included in the measurement of  
6 projected area and number concentration, even particles that intersect the edges of the 2D-S field  
7 of view, and in those cases their maximum dimension and projected area is approximated. When  
8 using the M7 method, only particles that are completely inside the 2D-S field of view (“all-in”  
9 particles) are included. This provides an accurate measurement of projected area and maximum  
10 dimension for all particles. ~~Although the sample volume decreases by using M7 method, such a~~  
11 ~~decrease is not significant. Figures S1 and S3 show number concentration and area concentration~~  
12 ~~as functions of maximum dimension for cases of synoptic and anvil cirrus clouds, respectively. It~~  
13 ~~is seen that the M1 and M7 methods agree well for both number concentration and area~~  
14 ~~concentration, with a and larger difference between the M1 and M7 methods is observed for~~  
15 ~~larger particles ( $D > 300 \mu\text{m}$ ). Moreover, the comparison of the M1 and M7 methods for the PSD~~  
16 ~~number concentration and extinction is displayed in Figs. S2 and S4. The difference in~~  
17 ~~sample PSD projected area (i.e. extinction) between the M1 and M7 methods does not exceed 5~~  
18 ~~% and 13 % for synoptic and anvil cirrus clouds, respectively. In other words, the difference~~  
19 ~~for projected area is more pronounced in anvil than in synoptic cirrus due to the existence of~~  
20 ~~slightly larger ice particles in anvil clouds that have a greater chance of intersecting the edges of~~  
21 ~~the 2D-S field of view.~~

## 23 **Appendix B: Calculation of ice particle mass from CPI measurements of projected** 24 **area and aspect ratio**

25 There is no direct measurement of ice particle mass by the CPI probe. Moreover, the BL2006  $m$ -  
26  $A$  relationship is based on ice particles larger than  $\sim 150 \mu\text{m}$ . Therefore, we developed a new  
27 method for estimating mass based on CPI measurements of ice particle projected area, length and  
28 width. It is assumed that when  $10 \mu\text{m} < D < 100 \mu\text{m}$ , all ice crystals are hexagonal columns. The

1 apparent aspect ratio ( $\epsilon$ ), defined as the CPI measured mean length-to-width ratio for a given  
 2 size-interval, is generally between 1 and 2 in this size range and the ice crystals are known to be  
 3 relatively dense (more mass per maximum dimension), making this shape assumption a  
 4 reasonable approximation (Korolev and Isaac, 2003; Lawson et al., 2006b; C2012). This is  
 5 considerably more accurate than assuming ice particles to be spherical.

6 Figure B1.a shows the geometrical features of a hexagonal prism that has eight faces: two basal  
 7 faces with hexagonal shape and six prism faces with rectangular shape. The axis along the prism  
 8 face is defined as the  $c$ -axis and the maximum dimension across the basal face is defined as the  
 9  $a$ -axis. The true aspect ratio ( $\zeta$ ) of a hexagonal column is defined as  $\frac{c}{a}$  (Lamb and Verlinde,  
 10 2011; Pruppacher and Klett, 1998). Since the CPI provides 2-D images,  $\zeta$  and  $\epsilon$  can be different  
 11 due to crystal orientation. As far as we know, there is no preferred orientation for small ice  
 12 crystals entering the CPI probe sample volume. Therefore, we assume random orientation and  
 13 develop a method to estimate  $\zeta$  from  $\epsilon$  as described here.

14 Consider three planes in the 3-D space: one plane orthogonal to the direction of view or beam  
 15 direction (hereafter called P1; Fig. B1.a), and two planes orthogonal to the first plane in  
 16 alignment with the direction of view (hereafter called P2 and P3). When the  $c$ -axis is parallel to  
 17 P1, all orientations of a hexagonal column yield the projected area equal to area of the prism face  
 18 ( $A_{p,max}$ ), as shown in Fig. B1.b. However, when the  $c$ -axis is parallel to P2 or P3, the maximum  
 19 and minimum projected areas correspond to  $A_{p,max}$  and the area of the basal face ( $A_{b,max}$ ),  
 20 respectively (Figs. B1.c and B1.d). Therefore, for both P2 and P3, the average hexagonal column  
 21 projected area corresponds to the average projected area of these two extremes;  
 22  $(A_{p,max} + A_{b,max})/2$ . Thus, the average projected area for all orientations  $\langle A \rangle$  can be estimated as  
 23 the average of the mean projected area in three planes:

$$\langle A \rangle \approx \frac{1}{3} \left( A_{p,max} + \frac{A_{p,max} + A_{b,max}}{2} + \frac{A_{p,max} + A_{b,max}}{2} \right). \quad (B1)$$

24 Since  $A_{p,max}$  is equal to  $ac$  (area of rectangle), and  $A_{b,max}$  is equal to  $3^{\frac{3}{2}}a^2/8$  (area of hexagon):

$$\langle A \rangle \approx \frac{1}{3} \left( 2ac + \frac{3^{\frac{3}{2}} a^2}{8} \right). \quad (\text{B2})$$

1 Noting that  $c = \zeta a$ , we can write:

$$\langle A \rangle \approx \frac{1}{3} \left( 2\zeta a^2 + \frac{3^{\frac{3}{2}} a^2}{8} \right). \quad (\text{B3})$$

2 Expanding on the insight from Eq. (B1),  $\zeta$  can be estimated from  $\varepsilon$ . In the P1 plane,  $\varepsilon$  is equal to  
 3  $\zeta$ . However, for P2 and P3, there are two extremes:  $\varepsilon = \zeta$  when  $A = A_{p,\max}$ , and  $\varepsilon = 1$  when  
 4  $A = A_{p,\min}$ . So, the crystal orientation and apparent aspect ratio representing P2 and P3 will be  
 5 the average of these two extremes  $(\zeta + 1)/2$ . The overall value for  $\varepsilon$  should equal the average  
 6 apparent aspect ratio corresponding to all three planes. Therefore,  $\varepsilon$  is equal to  
 7  $[\zeta + (\zeta + 1)/2 + (\zeta + 1)/2]/3$ , and we can write:

$$\varepsilon = \frac{1}{3}(2\zeta + 1). \quad (\text{B4})$$

8 Solving for  $\zeta$  from Eq. (B4):

$$\zeta = \frac{(3\varepsilon - 1)}{2}. \quad (\text{B5})$$

9 Let  $A_{cpi}$  be the CPI measurement of projected area. Then, Eq. (B3) represents  $A_{cpi}$ , and it can be  
 10 used to estimate  $a$ :

$$a \approx \left( \frac{3A_{cpi}}{2\zeta + \frac{3^{\frac{3}{2}}}{8}} \right)^{\frac{1}{2}}. \quad (\text{B6})$$



1 Volume of a hexagonal column ( $V_h$ ) is defined as:

$$V_h = \left( \frac{3^{\frac{3}{2}}}{8} \right) a^2 c. \quad (B7)$$

2 The mass of a hexagonal column ( $m$ ) is equal to  $\rho_i V_h$  where  $\rho_i$  is bulk density of ice and is  
3 equal to  $0.917 \text{ g cm}^{-3}$ . Therefore, the ice particle mass can be estimated from  $a$  and  $\zeta$  as:

$$m_{cpi} = \rho_i \left( \frac{3^{\frac{3}{2}}}{8} \right) a^3 \zeta. \quad (B8)$$

4 Since  $\zeta$  and  $a$  are calculated from Eqs. (B5) and (B6), respectively,  $m_{cpi}$  is estimated from  $A_{cpi}$   
5 and  $\varepsilon$ .

6 One benefit of the hexagonal column assumption is consideration of ice particle aspect ratio. The  
7 spherical ice assumption means that the aspect ratio is unity. Assuming that ice particles are  
8 spherical, their mass can be calculated as a function of projected area (e.g.  
9  $m_{sphere} = \rho_i \frac{4}{3\sqrt{\pi}} A_{sphere}^{3/2}$ ). We calculated the percent difference of mass between the spherical  
10 and hexagonal column assumptions (where column aspect ratio = 1.0), and this value is ~ 4%.

Field Code Changed

11

12

Formatted: Subtitle, Left, Line spacing: single

### 13 Appendix C: List of symbols

Formatted: Subtitle, Left, Space Before: 0 pt, Line spacing: single

14  $a$  maximum dimension across the basal face of a hexagonal crystal

15  $a_v$  prefactor in fall speed-dimension power law

Field Code Changed

16  $A$  projected area

Formatted: Font: Not Bold, Italic

Formatted: Font: Not Bold

1  $\langle A \rangle$  average projected area of a hexagonal crystal for all orientations

Field Code Changed

2  $A_{b,max}$  area of the basal face of a hexagonal crystal

Field Code Changed

3  $A_{p,max}$  area of the prism face of a hexagonal crystal

Field Code Changed

4  $A_r$  area ratio

5  $A_t$  total PSD projected area

6  $b_v$  exponent in fall speed-dimension power law

7  $c$  length along the prism face of a hexagonal crystal

Formatted: Font: Not Bold

8  $D$  maximum dimension of ice particle

Formatted: Font: (Default) Times New Roman, Not Bold, Italic

9  $D_e$  characteristic dimension of the ice PSD

Formatted: Font: (Default) Times New Roman, Not Bold

Formatted: Subscript

10  $\bar{D}$  mean maximum dimension of a PSD

Field Code Changed

11  $D_A$  median area dimension

Formatted: Font: Not Bold

12  $D_e$  effective diameter

Formatted: Font: Not Bold, Italic

Formatted: Font: Not Bold, Italic, Subscript

13  $D_i$  dimension of interest

Formatted: Font: Not Bold

Formatted: Font: (Default) Times New Roman, 12 pt

14  $D_m$  median mass dimension

15  $D_N$  number concentration dimension

16  $D_Z$  reflectivity dimension

17  $g$  gravitational constant

18  $IWC$  ice water content

Formatted: Font: Not Bold

19  $m$  mass of ice particle

Formatted: Font: Not Bold, Italic

Formatted: Font: Not Bold

- 1  $N$  number concentration
- 2  $N_o$  prefactor of a gamma PSD
- 3 PSD particle size distribution
- 4  $R$  relative ratio of mass to area
- 5  $R^2$  coefficient of determination
- 6  $T$  temperature
- 7  $V$  terminal fall speed of ice particle
- 8  $V_h$  volume of a hexagonal crystal
- 9  $V_m$  mass-weighted terminal fall speed
- 10  $Z$  radar reflectivity
- 11  $X$  Best number
- 12  $\alpha$  prefactor in mass-dimension power law
- 13  $\beta$  exponent in mass-dimension power law
- 14  $\gamma$  prefactor in projected area-dimension power law
- 15  $\delta$  exponent in projected area-dimension power law
- 16  $\Gamma$  gamma function
- 17  $\varepsilon$  apparent aspect ratio
- 18  $\zeta$  true aspect ratio
- 19  $\eta$  dynamic viscosity of air
- 20  $\lambda$  slope parameter of a gamma PSD

**Formatted:** Font: Italic

**Formatted:** Font: Not Bold

**Formatted:** Font: Not Bold, Italic

**Formatted:** Font: Not Bold

**Formatted:** Font: Not Bold

1  $\nu$  dispersion parameter of a gamma PSD

2  $\sigma$  standard deviation

3  $\rho_{air}$  density of air

4  $\rho_i$  bulk density of ice

5

6

7

8

## 9 Acknowledgements

10 This research was supported by the Office of Science (BER), U.S. Department of Energy. We  
11 are very grateful to Paul Lawson, Sara Lance, Sarah Woods, Ted Fisher, and Qixu Mo for  
12 processing the SPARTICUS 2D-S and CPI data in a manner that best served the needs of this  
13 study. We are also grateful to Brad Baker for providing us with the measurements of ice particle  
14 projected area that were used in BL2006. The first author would like to appreciate Office of  
15 International Students and Scholars at University of Nevada, Reno for awarding an international  
16 student scholarship for two years. Finally, the authors express their gratitude to two anonymous  
17 reviewers for their constructive comments that improved the paper. The SCPP data used in this  
18 study and associated software is freely available to interested researchers; those interested should  
19 contact the second author.

20

## 21 References

22 Avramov, A., and co-authors: Toward ice formation closure in Arctic mixed-phase boundary  
23 layer clouds during ISDAC, J. Geophys. Res.-Atmos., 116, D00T08,  
24 doi:10.1029/2011JD015910, 2011,???

Field Code Changed

Field Code Changed

Formatted: Font: (Default) Arial

Formatted: Space Before: 0 pt

1 Bailey, M. P., and Hallett, J.: Growth Rates and Habits of Ice Crystals between -20° and -70 °C,  
2 J. Atmos. Sci., 61, 514-544, 2004.

3 Bailey, M. P., and Hallett, J.: A Comprehensive Habit Diagram for Atmospheric Ice Crystals:  
4 Confirmation from the Laboratory, AIRS II, and Other Field Studies, J. Atmos. Sci., 66, 2888-  
5 2899, doi:10.1175/2009JAS2883.1, 2009.

6 Baker, B., and Lawson, R. P.: Improvement in determination of ice water content from two-  
7 dimensional particle imagery. Part I: Image-to-mass relationships, J. Appl. Meteorol. & Clim.,  
8 45, 1282-1290, doi:10.1175/jam2398.1, 2006a.

9 [Baker, B. A., and Lawson, R. P.: In Situ Observations of the Microphysical Properties of Wave,](#)  
10 [Cirrus, and Anvil Clouds. Part I: Wave Clouds, J. Atmos. Sci., 63, 3160-3185, 2006.](#) ~~J. Atmos.~~  
11 ~~Sci., 2006~~ ~~2006b.~~

Formatted: Font: Not Bold

Formatted: Font: Not Bold

12 Baran, A. J.: From the single-scattering properties of ice crystals to climate prediction: A way  
13 forward, Atmos. Res., 112, 45-69, doi:10.1016/j.atmosres.2012.04.010, 2012.

14 Brown, P. R. A., and Francis, P. N.: Improved measurements of the ice water content in cirrus  
15 using a total-water probe, J. Atmos. & Ocean. Tech., 12, 410-414, doi:10.1175/1520-  
16 0426(1995)012<0410:imotiw>2.0.co;2, 1995.

17 Cotton, R. J., Field, P. R., Ulanowski, Z., Kaye, P. H., Hirst, E., Greenaway, R. S., Crawford, I.,  
18 Crosier, J., and Dorsey, J.: The effective density of small ice particles obtained from in situ  
19 aircraft observations of mid-latitude cirrus, Q. J. Roy. Meteor. Soc., 139, 1923-1934,  
20 doi:10.1002/qj.2058, 2013.

21 Delanoe, J., and Hogan, R. J.: Combined CloudSat-CALIPSO-MODIS retrievals of the  
22 properties of ice clouds, J. Geophys. Res.-Atmos., 115, D00h29, doi:10.1029/2009jd012346,  
23 2010.

Formatted: Space Before: 0 pt, After: 12 pt

24 [Eidhammer, T., Morrison, H., Mitchell, D. L., Gettelman, A., and Erfani, E.: Improvements in](#)  
25 [the Community Atmosphere Model \(CAM5\) microphysics using a consistent representation of](#)  
26 [ice particle properties. Submitted to J. Climate, 2016.](#)

27 [Fontaine, E., Schwarzenboeck, A., Delanoe, J., Wobrock, W., Leroy, D., Dupuy, R., Gourbeyre,](#)

1 [C., and Protat, A.: Constraining mass-diameter relations from hydrometeor images and cloud](#)  
2 [radar reflectivities in tropical continental and oceanic convective anvils, Atmos. Chem. Phys.,](#)  
3 [14, 11367-11392, doi:10.5194/acp-14-11367-2014, 2014.](#)

4 Foot, J. S.: Some observations of the optical properties of clouds. Part II: Cirrus, Q. J. Roy.  
5 Meteor. Soc., 114, 145-164, 1988.

6 Fu, Q.: An accurate parameterization of the solar radiative properties of cirrus clouds for climate  
7 models, J. Climate, 9, 2058-2082, doi:10.1175/1520-0442(1996)009<2058:aapots>2.0.co;2,  
8 1996.

9 Fu, Q., Yang, P., and Sun, W. B.: An accurate parameterization of the infrared radiative  
10 properties of cirrus clouds for climate models, J. Climate, 11, 2223-2237, doi:10.1175/1520-  
11 0442(1998)011<2223:aapoti>2.0.co;2, 1998.

12 Gettelman, A., Liu, X., Ghan, S. J., Morrison, H., Park, S., Conley, A. J., Klein, S. A., Boyle, J.,  
13 Mitchell, D. L., and Li, J. L. F.: Global simulations of ice nucleation and ice supersaturation with  
14 an improved cloud scheme in the Community Atmosphere Model, J. Geophys. Res.-Atmos., 115,  
15 D18216, doi:10.1029/2009jd013797, 2010.

16 Heymsfield, A. J., Lewis, S., Bansemer, A., Jaquinta, J., Miloshevich, L. M., Kajikawa, M.,  
17 Twohy, C., and Poellot, M. R.: A general approach for deriving the properties of cirrus and  
18 stratiform ice cloud particles, J. Atmos. Sci., 59, 3-29, doi:10.1175/1520-  
19 0469(2002)059<0003:agafdt>2.0.co;2, 2002.

20 Heymsfield, A. J., Bansemer, A., Schmitt, C., Twohy, C., and Poellot, M. R.: Effective ice  
21 particle densities derived from aircraft data, J. Atmos. Sci., 61, 982-1003, doi:10.1175/1520-  
22 0469(2004)061<0982:eipddf>2.0.co;2, 2004.

23 Heymsfield, A. J., Bansemer, A., and Twohy, C. H.: Refinements to ice particle mass  
24 dimensional and terminal velocity relationships for ice clouds. Part I: Temperature dependence,  
25 J. Atmos. Sci., 64, 1047-1067, doi:10.1175/jas3890.1, 2007.

26 Heymsfield, A. J., Schmitt, C., Bansemer, A., and Twohy, C. H.: Improved Representation of Ice  
27 Particle Masses Based on Observations in Natural Clouds, J. Atmos. Sci., 67, 3303-3318,

1 doi:10.1175/2010jas3507.1, 2010.

2 Heymsfield, A. J., and Westbrook, C. D.: Advances in the Estimation of Ice Particle Fall Speeds  
3 Using Laboratory and Field Measurements, *J. Atmos. Sci.*, 67, 2469-2482,  
4 doi:10.1175/2010jas3379.1, 2010.

5 [Jackson, R. C., McFarquhar, G. M., Korolev, A. V., Earle, M. E., Liu, P. S., Lawson, R. P.,  
6 Brooks, S., Wolde, M., Laskin, A., and Freer, M.: The dependence of ice microphysics on  
7 aerosol concentration in arctic mixed-phase stratus clouds during ISDAC and M-PACE, \*J.  
8 Geophys. Res.-Atmos.\*, 117, doi:10.1029/2012JD017668, 2012.](#)

9 [Jensen, E. J., Lawson, R. P., Bergman, J. W., Pfister, L., Bui, T. P., and Schmitt, C. G.: Physical  
10 processes controlling ice concentrations in synoptically forced, midlatitude cirrus, \*J. Geophys.  
11 Res.-Atmos.\*, 118, 5348-5360, doi:10.1002/jgrd.50421, 2013.](#)

12 Korolev, A., Strapp, J. W., and Isaac, G. A.: Evaluation of the accuracy of PMS Optical Array  
13 Probes, *J. Atmos. & Ocean. Tech.*, 15, 708-720, doi:10.1175/1520-  
14 0426(1998)015<0708:eotaop>2.0.co;2, 1998.

15 Korolev, A., and Isaac, G.: Roundness and aspect ratio of particles in ice clouds, *J. Atmos. Sci.*,  
16 60, 1795-1808, doi:10.1175/1520-0469(2003)060<1795:raarop>2.0.co;2, 2003.

17 Korolev, A.: Reconstruction of the sizes of spherical particles from their shadow images. Part I:  
18 Theoretical considerations, *J. Atmos. & Ocean. Tech.*, 24, 376-389, doi:10.1175/jtech1980.1,  
19 2007.

20 Lamb, D., and Verlinde, J.: *Physics and Chemistry of Clouds*, Cambridge University Press, New  
21 York, NY, USA, 2011.

22 Lawson, R. P., Baker, B. A., Schmitt, C. G., and Jensen, T. L.: An overview of microphysical  
23 properties of Arctic clouds observed in May and July 1998 during FIRE ACE, *J. Geophys. Res.-  
24 Atmos.*, 106, 14989-15014, doi:10.1029/2000jd900789, 2001.

25 Lawson, R. P., O'Connor, D., Zmarzly, P., Weaver, K., Baker, B., Mo, Q., and Jonsson, H.: The  
26 2D-S (Stereo) probe: Design and preliminary tests of a new airborne, high-speed, high-resolution  
27 particle Imaging probe, *J. Atmos. & Ocean. Tech.*, 23, 1462-1477, doi:10.1175/jtech1927.1,

1 2006a.

2 [Lawson, R. P., B. A. Baker, B. A., Pilson, B., and Mo, Q.: In situ observations of the](#)  
3 [microphysical properties of wave, cirrus and anvil clouds. Part II: Cirrus clouds. J. Atmos. Sci.,](#)  
4 [63, 3186–3203, 2006b., and Baker, B.: ???, J. Atmos. Sci., ???, ???](#)

Formatted: Font: Not Italic

Formatted: Font: Not Bold

5 Lawson, R. P., Jensen, E., Mitchell, D. L., Baker, B., Mo, Q., and Pilson, B.: Microphysical and  
6 radiative properties of tropical clouds investigated in TC4 and NAMMA, J. Geophys. Res.-  
7 Atmos., 115, D00j08, doi:10.1029/2009jd013017, 2010.

8 Lawson, R. P.: Effects of ice particles shattering on the 2D-S probe, Atmos. Meas. Tech., 4,  
9 1361-1381, doi:10.5194/amt-4-1361-2011, 2011.

10 [Lawson, R. P.: Improvement in Determination of Ice Water Content from Two-Dimensional](#)  
11 [Particle Imagery. Part III: Ice Particles with High a- to c-axis Ratio. Submitted to J. Appl.](#)  
12 [Meteorol. and Climate, 2016,](#)

Formatted: Font color: Custom Color(RGB(0,0,220))

13 [Locatelli, J. d., and Hobbs, P. V.: Fall speeds and masses of solid precipitation particles, J.](#)  
14 [Geophys. Res., 79, 2185-2197, doi:10.1029/JC079i015p02185, 1974.](#)

15 Mace, J., Jensen, E., McFarquhar, G., Comstock, J., Ackerman, T., Mitchell, D., Liu, X., and  
16 Garrett, T.: SPARTICUS: Small Particles in Cirrus, Science and Operations Plan, Tech. Rep.,  
17 DOE/SC-ARM-10-003, The Atmospheric Radiation Measurement Program, U.S. Department of  
18 Energy, <https://www.arm.gov/publications/programdocs/doe-sc-arm-10-003.pdf> (last access: 20  
19 October 2015), 2009.

20 [McFarquhar, G. M., Timlin, M. S., Rauber, R. M., Jewett, B. F., and Grim, J. A.: Vertical](#)  
21 [variability of cloud hydrometeors in the stratiform region of mesoscale convective systems and](#)  
22 [bow echoes, Mon. Wea. Rev., 135, 3405-3428, doi:10.1175/mwr3444.1, 2007.](#)

23 [McFarquhar, G. M., Um, J., and Jackson, R.: Small Cloud Particle Shapes in Mixed-Phase](#)  
24 [Clouds, J. Appl. Meteor. Climatol., 52, 1277–1293, doi: \[http://dx.doi.org/10.1175/JAMC-D-12-\]\(http://dx.doi.org/10.1175/JAMC-D-12-0114.1\)](#)  
25 [0114.1, 2013](#)

26 Mishra, S., Mitchell, D. L., Turner, D. D., and Lawson, R. P.: Parameterization of ice fall speeds



1 in midlatitude cirrus: Results from SPARTICUS, *J. Geophys. Res.-Atmos.*, 119, 3857-3876,  
2 doi:10.1002/2013jd020602, 2014.

3 Mitchell, D. L.: Evolution of snow-size spectra in cyclonic storms .1. snow growth by vapor-  
4 deposition and aggregation, *J. Atmos. Sci.*, 45, 3431-3452, doi:10.1175/1520-  
5 0469(1988)045<3431:eosssi>2.0.co;2, 1988.

6 Mitchell, D. L., Zhang, R., and Pitter, R. L.: Mass-dimensional relationships for ice particles and  
7 the influence of riming on snowfall rates, *J. Appl. Meteorol.*, 29, 153-163, doi:10.1175/1520-  
8 0450(1990)029<0153:mdrfip>2.0.co;2, 1990.

9 Mitchell, D. L.: Evolution of snow-size spectra in cyclonic storms .2. deviations from the  
10 exponential form, *J. Atmos. Sci.*, 48, 1885-1899, doi:10.1175/1520-  
11 0469(1991)048<1885:eosssi>2.0.co;2, 1991.

12 Mitchell, D. L.: Use of mass- and area-dimensional power laws for determining precipitation  
13 particle terminal velocities, *J. Atmos. Sci.*, 53, 1710-1723, doi:10.1175/1520-  
14 0469(1996)053<1710:uomaad>2.0.co;2, 1996.

15 Mitchell, D. L.: Parameterization of the Mie extinction and absorption coefficients for water  
16 clouds, *J. Atmos. Sci.*, 57, 1311-1326, doi:10.1175/1520-0469(2000)057<1311:potmea>2.0.co;2,  
17 2000.

18 Mitchell, D. L.: Effective diameter in radiation transfer: General definition, applications, and  
19 limitations, *J. Atmos. Sci.*, 59, 2330-2346, doi:10.1175/1520-  
20 0469(2002)059<2330:edirtg>2.0.co;2, 2002.

21 Mitchell, D. L., Baran, A. J., Arnott, W. P., and Schmitt, C.: Testing and comparing the modified  
22 anomalous diffraction approximation, *J. Atmos. Sci.*, 63, 2948-2962, doi:10.1175/jas3775.1,  
23 2006.

24 Mitchell, D. L., Rasch, P., Ivanova, D., McFarquhar, G., and Nousiainen, T.: Impact of small ice  
25 crystal assumptions on ice sedimentation rates in cirrus clouds and GCM simulations, *Geophys.*  
26 *Res. Lett.*, 35, L09806, doi:10.1029/2008gl033552, 2008.

1 Mitchell, D. L., d'Entremont, R. P., and Lawson, R. P.: Inferring Cirrus Size Distributions  
2 through Satellite Remote Sensing and Microphysical Databases, *J. Atmos. Sci.*, 67, 1106-1125,  
3 doi:10.1175/2009jas3150.1, 2010.

4 Mitchell, D. L., Mishra, S., and Lawson, R. P.: Representing the ice fall speed in climate models:  
5 Results from Tropical Composition, Cloud and Climate Coupling (TC4) and the Indirect and  
6 Semi-Direct Aerosol Campaign (ISDAC), *J. Geophys. Res.-Atmos.*, 116, D00t03,  
7 doi:10.1029/2010jd015433, 2011.

8 Morrison, H., and Gettelman, A.: A new two-moment bulk stratiform cloud microphysics  
9 scheme in the community atmosphere model, version 3 (CAM3). Part I: Description and  
10 numerical tests, *J. Climate*, 21, 3642-3659, doi:10.1175/2008jcli2105.1, 2008.

11 Pruppacher, H. R., and Klett, J. D.: *Microphysics of clouds and precipitation: 2nd edn*, Kluwer  
12 Academic Publishers, Dordrecht, the Netherlands, 1996.

13 Sanderson, B. M., Piani, C., Ingram, W. J., Stone, D. A., and Allen, M. R.: Towards constraining  
14 climate sensitivity by linear analysis of feedback patterns in thousands of perturbed-physics  
15 GCM simulations, *Clim. Dynam.*, 30, 175-190, doi:10.1007/s00382-007-0280-7, 2008.

16 [Um, J., and McFarquhar, G. M.: Dependence of the single-scattering properties of small ice  
17 crystals on idealized shape models, \*Atmos. Chem. Phys.\*, 11, 3159-3171, doi:10.5194/acp-11-  
18 3159-2011, 2011.](#)

19 Yang, P., Wei, H. L., Huang, H. L., Baum, B. A., Hu, Y. X., Kattawar, G. W., Mishchenko, M.  
20 I., and Fu, Q.: Scattering and absorption property database for nonspherical ice particles in the  
21 near- through far-infrared spectral region, *Appl. Optics*, 44, 5512-5523,  
22 doi:10.1364/ao.44.005512, 2005.

23 Zhao, Y., Mace, G. G., and Comstock, J. M.: The Occurrence of Particle Size Distribution  
24 Bimodality in Midlatitude Cirrus as Inferred from Ground-Based Remote Sensing Data, *J.*  
25 *Atmos. Sci.*, 68, 1162-1177, doi:10.1175/2010jas3354.1, 2011.

26

1 Table 1. Polynomial curve fits of the form  $\ln m = a_0 + a_1 \ln D + a_2 (\ln D)^2$  for synoptic and anvil  
2 cirrus clouds sampled during SPARTICUS, where  $m$  is in grams and  $D$  is in cm. The only  
3 exception is for synoptic cirrus between  $-20$  and  $-40$  °C, where SCPP data was used in lieu of  
4 SPARTICUS data, as shown in Fig. 3. The number of  $m$ - $D$  samples is given by  $N$ , along with the  
5 coefficient of determination ( $R^2$ ) of the curve fit. See Sect. 3 for details.

Temperature Range	$a_0$	$a_1$	$a_2$	$N$	$R^2$
Synoptic Cirrus Clouds					
$-40$ °C < $T \leq -20$ °C	-6.72924	1.17421	-0.15980	201	0.99702
$-55$ °C < $T \leq -40$ °C	-7.21010	1.26123	-0.12184	139	0.99507
$-65$ °C < $T \leq -55$ °C	-11.34570	-0.45436	-0.29627	54	0.99283
Anvil Cirrus Clouds					
$-40$ °C < $T \leq -20$ °C	-6.67252	1.36857	-0.12293	226	0.99773
$-55$ °C < $T \leq -40$ °C	-6.44787	1.64429	-0.07788	160	0.98368
$-65$ °C < $T \leq -55$ °C	-9.24318	0.57189	-0.17865	49	0.98285

6

1 Table 2. Polynomial curve fits of the form  $\ln A = a_0 + a_1 \ln D + a_2 (\ln D)^2$  for synoptic and anvil  
 2 cirrus clouds sampled during SPARTICUS, where  $A$  is in  $\text{cm}^2$  and  $D$  is in cm. The number of  $A$ -  
 3  $D$  samples is given by  $N$ , along with the coefficient of determination ( $R^2$ ) of the curve fit.

Temperature Range	$a_0$	$a_1$	$a_2$	$N$	$R^2$
Synoptic Cirrus Clouds					
$-40^\circ\text{C} < T \leq -20^\circ\text{C}$	-2.46356	1.25892	-0.07845	201	0.99803
$-55^\circ\text{C} < T \leq -40^\circ\text{C}$	-2.60478	1.32260	-0.05957	139	0.99781
$-65^\circ\text{C} < T \leq -55^\circ\text{C}$	-4.63488	0.54233	-0.13260	54	0.99784
Anvil Cirrus Clouds					
$-40^\circ\text{C} < T \leq -20^\circ\text{C}$	-2.40314	1.29749	-0.07233	226	0.99852
$-55^\circ\text{C} < T \leq -40^\circ\text{C}$	-2.38913	1.40166	-0.05219	160	0.99753
$-65^\circ\text{C} < T \leq -55^\circ\text{C}$	-2.43451	1.60639	-0.01164	49	0.98606

4

1 Table 3. Uncertainty estimates for mass-dimension power  $\beta$  for synoptic cirrus clouds.

Temperature Range	Ice Particle Size ( $\mu\text{m}$ )				
	50	150	500	1500	4500
	Power $\beta$				
-25 °C < $T \leq$ -20 °C	2.792	2.455	2.085	1.748	1.411
-30 °C < $T \leq$ -25 °C	2.846	2.449	2.015	1.618	1.221
-35 °C < $T \leq$ -30 °C	2.773	2.429	2.053	1.710	1.367
-40 °C < $T \leq$ -35 °C	2.642	2.371	2.073	1.802	1.530
-45 °C < $T \leq$ -40 °C	2.556	2.254	1.923	1.621	1.320
-50 °C < $T \leq$ -45 °C	2.549	2.276	1.977	1.704	1.431
-55 °C < $T \leq$ -50 °C	2.495	2.322	2.133	1.960	1.787
-60 °C < $T \leq$ -55 °C	2.686	2.064	1.382	----	----
-65 °C < $T \leq$ -60 °C	2.863	1.732	----	----	----
Mean $\beta$	2.689	2.261	1.955	1.738	1.438
Standard Deviation of $\beta$	0.129	0.220	0.225	0.109	0.168
Mean Uncertainty (%)	9.031				

2

1 Table 4. Same as Table 3, but for anvil cirrus clouds.

Temperature Range	Ice Particle Size ( $\mu\text{m}$ )				
	50	150	500	1500	4500
	Power $\beta$				
$-25\text{ }^{\circ}\text{C} < T \leq -20\text{ }^{\circ}\text{C}$	2.614	2.387	2.138	1.911	1.683
$-30\text{ }^{\circ}\text{C} < T \leq -25\text{ }^{\circ}\text{C}$	2.726	2.426	2.098	1.799	1.499
$-35\text{ }^{\circ}\text{C} < T \leq -30\text{ }^{\circ}\text{C}$	2.653	2.394	2.110	1.850	1.591
$-40\text{ }^{\circ}\text{C} < T \leq -35\text{ }^{\circ}\text{C}$	2.679	2.394	2.083	1.798	1.513
$-45\text{ }^{\circ}\text{C} < T \leq -40\text{ }^{\circ}\text{C}$	2.655	2.370	2.058	1.773	1.488
$-50\text{ }^{\circ}\text{C} < T \leq -45\text{ }^{\circ}\text{C}$	2.531	2.302	2.051	1.822	1.593
$-55\text{ }^{\circ}\text{C} < T \leq -50\text{ }^{\circ}\text{C}$	2.432	2.273	2.100	1.941	1.782
$-60\text{ }^{\circ}\text{C} < T \leq -55\text{ }^{\circ}\text{C}$	2.533	2.105	1.637	----	----
$-65\text{ }^{\circ}\text{C} < T \leq -60\text{ }^{\circ}\text{C}$	2.446	1.956	1.419	----	----
Mean $\beta$	2.585	2.290	1.966	1.842	1.593
Standard Deviation of $\beta$	0.105	0.159	0.255	0.063	0.108
Mean Uncertainty (%)	6.715				

2

1 Table 5. Uncertainty estimates for area-dimension power  $\delta$  for synoptic cirrus clouds.

Temperature Range	Ice Particle Size ( $\mu\text{m}$ )				
	50	150	500	1500	4500
	Power $\delta$				
-25 °C < T ≤ -20 °C	2.133	1.938	1.725	1.531	1.337
-30 °C < T ≤ -25 °C	2.170	1.932	1.671	1.432	1.194
-35 °C < T ≤ -30 °C	2.140	1.927	1.693	1.480	1.267
-40 °C < T ≤ -35 °C	2.027	1.882	1.722	1.576	1.431
-45 °C < T ≤ -40 °C	2.011	1.821	1.612	1.422	1.232
-50 °C < T ≤ -45 °C	1.941	1.810	1.666	1.534	1.403
-55 °C < T ≤ -50 °C	1.861	1.842	1.821	1.801	1.782
-60 °C < T ≤ -55 °C	1.960	1.669	1.350	----	----
-65 °C < T ≤ -60 °C	2.018	1.509	----	----	----
Mean $\delta$	2.029	1.814	1.658	1.540	1.378
Standard Deviation of $\delta$	0.103	0.142	0.138	0.128	0.198
Mean Uncertainty (%)	8.428				

2

1 Table 6. Same as Table 5, but for anvil cirrus clouds.

Temperature Range	Ice Particle Size ( $\mu\text{m}$ )				
	50	150	500	1500	4500
	Power $\delta$				
$-25\text{ }^\circ\text{C} < T \leq -20\text{ }^\circ\text{C}$	2.023	1.899	1.763	1.639	1.515
$-30\text{ }^\circ\text{C} < T \leq -25\text{ }^\circ\text{C}$	2.108	1.925	1.724	1.541	1.357
$-35\text{ }^\circ\text{C} < T \leq -30\text{ }^\circ\text{C}$	2.051	1.900	1.735	1.584	1.434
$-40\text{ }^\circ\text{C} < T \leq -35\text{ }^\circ\text{C}$	2.063	1.894	1.708	1.539	1.370
$-45\text{ }^\circ\text{C} < T \leq -40\text{ }^\circ\text{C}$	2.055	1.885	1.698	1.528	1.358
$-50\text{ }^\circ\text{C} < T \leq -45\text{ }^\circ\text{C}$	1.943	1.828	1.701	1.586	1.470
$-55\text{ }^\circ\text{C} < T \leq -50\text{ }^\circ\text{C}$	1.869	1.808	1.740	1.679	1.618
$-60\text{ }^\circ\text{C} < T \leq -55\text{ }^\circ\text{C}$	1.760	1.753	1.746	----	----
$-65\text{ }^\circ\text{C} < T \leq -60\text{ }^\circ\text{C}$	1.754	1.561	1.350	----	----
Mean $\delta$	1.959	1.828	1.685	1.585	1.446
Standard Deviation of $\delta$	0.135	0.114	0.128	0.056	0.097
Mean Uncertainty (%)	6.233				

2



1 **Figure Captions**

2 Figure 1. Dependence of ice particle mass ( $m$ ) on ice particle maximum dimension ( $D$ ), based on  
3 a variety of power law relationships in the literature (see text for details). Ice spheres indicate an  
4 upper limit for  $m$  at a given  $D$ . P1b, P1c and P1d denote planar crystals with sectorlike branches,  
5 broad branches and stellar dendrites, respectively, as described in Mitchell (1996).Figure 1.  
6 Dependence of ice particle mass ( $m$ ) on ice particle maximum dimension ( $D$ ), based on a variety  
7 of power law relationships in the literature (see text for details). Ice spheres indicate an upper  
8 limit for  $m$  at a given  $D$ . P1b, P1c and P1d denote planar crystals with sectorlike branches, broad  
9 branches and stellar dendrites, respectively, as described in Mitchell (1996).

- Formatted: Font: Not Italic
- Formatted: Font: Italic
- Formatted: Font: Italic
- Formatted: Font: Italic
- Formatted: Font: Italic
- Formatted: Font: Italic
- Formatted: Font: Italic
- Formatted: Font: Italic

10 Figure 2. SPARTICUS PSD sampling statistics for synoptic and anvil cirrus clouds where the  
11 PSDs have been grouped into temperature intervals of 5 °C.Figure 2. SPARTICUS PSD  
12 sampling statistics for synoptic and anvil cirrus clouds where the PSDs have been grouped into  
13 temperature intervals of 5 °C.

- Formatted: Font: Not Italic

14 Figure 3. Dependence of ice particle mass on  $D$  for mean PSDs sampled from synoptic cirrus  
15 clouds during SPARTICUS for  $-40^{\circ}\text{C} < T \leq -20^{\circ}\text{C}$  (blue curve fit based on CPI and 2D-S data),  
16 where a single mean PSD is the mean of all PSD contained within a 5 °C temperature interval,  
17 Also shown are CPI and SCPP data that are grouped into size-bins for the indicated temperature  
18 ranges and the black curve fit based on these data (see Table 1 for equation). The grey line for  
19 ice spheres gives the maximum possible mass for a given  $D$ .Figure 3. Dependence of ice particle  
20 mass on  $D$  for mean PSDs sampled from synoptic cirrus clouds during SPARTICUS for  $-40^{\circ}\text{C} <$   
21  $T \leq -20^{\circ}\text{C}$  (blue curve fit based on CPI and 2D-S data), where a single mean PSD is the mean of  
22 all PSD contained within a 5 °C temperature interval. Also shown are CPI and SCPP data that  
23 are grouped into size-bins for the indicated temperature ranges and the black curve fit based on  
24 these data (see Table 1 for equation). The grey line for ice spheres gives the maximum possible  
25 mass for a given  $D$ .

- Formatted: Font: Not Italic
- Formatted: Font: Italic
- Formatted: Font: Italic
- Formatted: Font: Italic
- Formatted: Font: Italic
- Formatted: Font: Italic
- Formatted: Font: Italic

26 Figure 4. Comparison of all the curve fits in Table 1 for each temperature regime (indicated by  
27 color) and cloud type (indicated by line type; solid or dashed). The anvil and synoptic curve fits  
28 are very similar.Figure 4. Comparison of all the curve fits in Table 1 for each temperature regime

- Formatted: Font: (Default) Times New Roman
- Formatted: Font: Not Italic

1 (indicated by color) and cloud type (indicated by line type; solid or dashed). The anvil and  
2 synoptic curve fits are very similar.

3 Figure 5. Dependence of ice particle projected area ( $A$ ) on  $D$  based on mean PSD within the  
4 indicated temperature regime. The CPI and 2D-S data have been grouped into size-bins, and the  
5 black solid curve is a fit to these datasets (see Table 2 for equation).  
6 Figure 5. Dependence of ice  
7 particle projected area ( $A$ ) on  $D$  based on mean PSD within the indicated temperature regime.  
8 The CPI and 2D-S data have been grouped into size bins, and the black solid curve is a fit to  
9 these datasets (see Table 2 for equation).

9 Figure 6. Fractional uncertainties (standard deviation/mean) for the mean ice particle projected  
10 area in each bin of the measured PSDs. Only temperature intervals having more than two PSDs  
11 are considered.  
12 Figure 6. Fractional uncertainties (standard deviation/mean) for the mean ice  
13 particle projected area in each bin of the measured PSDs. Only temperature intervals having  
14 more than two PSDs are considered.

14 Figure 7. The  $m/A$  ratio for ice particles normalized by the corresponding  $m/A$  ratio for ice  
15 spheres using the  $m-D$  and  $A-D$  curve fits appropriate for the indicated temperature regime. Blue  
16 curve is based on Tables 1 and 2, but black curve is only based on 2D-S data.  
17 Figure 7. The  $m/A$   
18 ratio for ice particles normalized by the corresponding  $m/A$  ratio for ice spheres using the  $m-D$   
19 and  $A-D$  curve fits appropriate for the indicated temperature regime. Blue curve is based on  
20 Tables 1 and 2, but black curve is only based on 2D-S data.

20 Figure 8. The  $m-D$  curve fit based on SCPP and CPI data (for indicated temperature regime) is  
21 compared with individual ice particle  $m-D$  measurements from SCPP, corresponding to ice  
22 particle shapes originating from similar temperatures. The number of ice particles sampled in  
23 each shape category is indicated. Also shown are comparisons with two other studies that  
24 derived  $m-D$  power laws from ice cloud field data.  
25 Figure 8. The  $m-D$  curve fit based on SCPP  
26 and CPI data (for indicated temperature regime) is compared with individual ice particle  $m-D$   
27 measurements from SCPP, corresponding to ice particle shapes originating from similar  
28 temperatures. The number of ice particles sampled in each shape category is indicated. Also  
29 shown are comparisons with two other studies that derived  $m-D$  power laws from ice cloud field  
30 data.

Formatted: Font: (Default) Times New Roman  
Formatted: Font: Not Italic  
Formatted: Font: Italic  
Formatted: Font: Italic

Formatted: Font: (Default) Times New Roman  
Formatted: Font: Not Italic  
Formatted: Font: Italic  
Formatted: Font: Italic  
Formatted: Font: Italic  
Formatted: Font: Italic  
Formatted: Font: Italic  
Formatted: Font: Italic

Formatted: Font: (Default) Times New Roman  
Formatted: Font: Not Italic

1 Figure 9. Same as Fig. 8, except the  $m$ - $D$  curve fit is based on SPARTICUS (2D-S & CPI) data  
2 and the SCPP field data have been grouped into size-bins; shown are the standard deviations ( $\sigma$ )  
3 in  $m$  and  $D$  for each size-bin. Mean values for  $m$  and  $D$  are shown by the intersection of the  $\sigma$ -  
4 bars. Figure 9. Same as Fig. 8, except the  $m$ - $D$  curve fit is based on SPARTICUS (2D-S & CPI)  
5 data and the SCPP field data have been grouped into size-bins; shown are the standard deviations  
6 ( $\sigma$ ) in  $m$  and  $D$  for each size-bin. Mean values for  $m$  and  $D$  are shown by the intersection of the  $\sigma$ -  
7 bars.

Formatted: Font: Not Italic

Formatted: Font: Not Italic

Formatted: Font: Not Italic

Formatted: Font: Not Italic

Formatted: Font: Not Italic

Formatted: Font: Italic

8 Figure 10. Mean area ratios for each mean PSD size-bin are shown as a proxy for ice particle  
9 shape. Temperature intervals corresponding to each mean PSD are indicated for synoptic ice  
10 clouds. Figure 10. Mean area ratios for each mean PSD size-bin are shown as a proxy for ice  
11 particle shape. Temperature intervals corresponding to each mean PSD are indicated for synoptic  
12 ice clouds.

Formatted: Font: (Default) Times New Roman

Formatted: Font: Not Italic

13 Figure 11. Same as Fig. 10, but for anvil ice clouds. Figure 11. Same as Fig. 10, but for anvil ice  
14 clouds.

Formatted: Font: (Default) Times New Roman

Formatted: Font: Not Italic

Formatted: Font: (Default) Times New Roman

15 Figure 12. Dependence of the ice particle  $N$  on  $\bar{D}$  using the 4 methods indicated for determining  
16  $\alpha$  and  $\beta$ . The black and blue curves use the  $m$ - $D$  curve fit based on Table 1 for the indicated  
17 temperature range, with the black curve  $\alpha$  and  $\beta$  evaluated at  $D = 500 \mu\text{m}$ . Figure 12. Dependence  
18 of the ice particle  $N$  on  $\bar{D}$  using the 4 methods indicated for determining  $\alpha$  and  $\beta$ . The black and  
19 blue curves use the  $m$ - $D$  curve fit based on Table 1 for the indicated temperature range, with the  
20 black curve  $\alpha$  and  $\beta$  evaluated at  $D = 500 \mu\text{m}$ .

21 Figure 13. Dependence of the  $De$  on  $\bar{D}$  using the 3 methods indicated for determining  $\alpha$ ,  $\beta$ ,  $\gamma$  and  
22  $\delta$ . The black and blue curves use the  $m$ - $D$  curve fit based on Table 1 and  $A$ - $D$  curve fit based on  
23 Table 2 for the indicated temperature range, with the black curve  $\alpha$ ,  $\beta$ ,  $\gamma$  and  $\delta$  evaluated at  $D =$   
24  $500 \mu\text{m}$ . Figure 13. Dependence of the  $De$  on  $\bar{D}$  using the 3 methods indicated for determining  $\alpha$ ,  
25  $\beta$ ,  $\gamma$  and  $\delta$ . The black and blue curves use the  $m$ - $D$  curve fit based on Table 1 and  $A$ - $D$  curve fit  
26 based on Table 2 for the indicated temperature range, with the black curve  $\alpha$ ,  $\beta$ ,  $\gamma$  and  $\delta$  evaluated  
27 at  $D = 500 \mu\text{m}$ .

Formatted: Font: (Default) Times New Roman

Formatted: Font: Not Italic

Formatted: Font: Italic

Formatted: Font: Italic, Not Superscript/ Subscript

Formatted: Font: Italic

Formatted: Font: Italic

Formatted: Font: Italic

Formatted: Font: Italic

Formatted: Font: Italic

Formatted: Font: Italic

Formatted: Font: Italic

Formatted: Font: Italic

Formatted: Font: Italic

28 Figure 14. Same as Fig. 13, but for the dependence of  $V_m$  on  $\bar{D}$ .

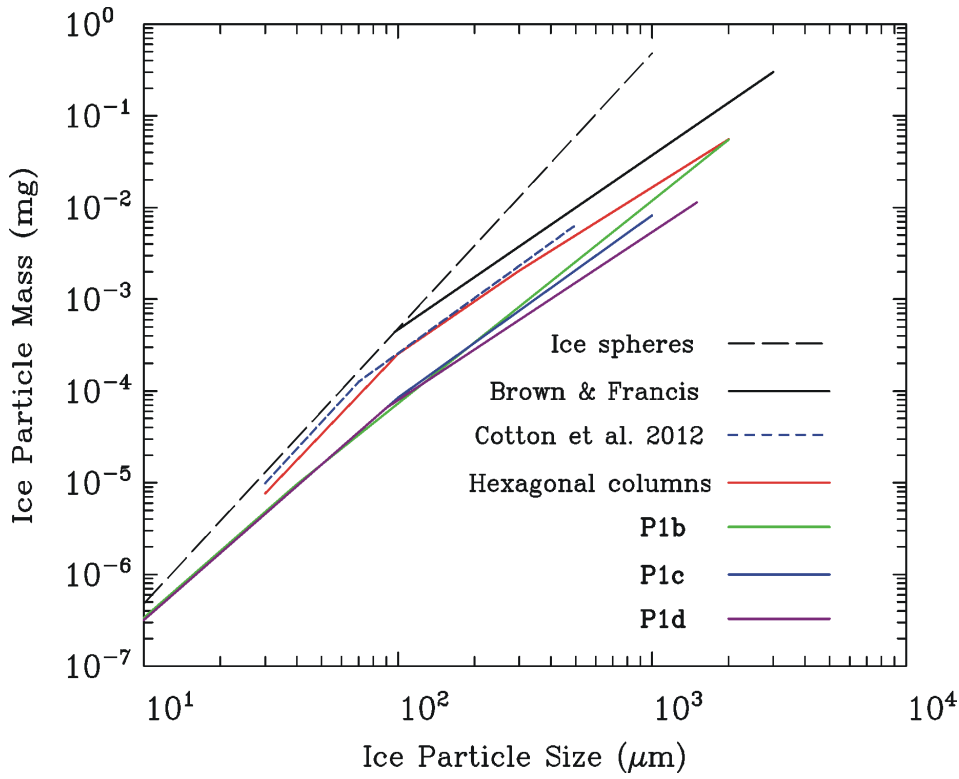
1 Figure A1. Geometry of dimension measurements showing length scales for the M1 method (*LI*)  
2 and the M7 method (MaxLength) for two different ice particle shapes. Courtesy of Paul Lawson  
3 and Sara Lance.

4 [Figure B1. a\) 3-D geometry of a hexagonal prism, representative of small ice crystals. Assuming](#)  
5 [that the direction of view \(beam direction\) is along the x axis, P1 is orthogonal to x axis, P2 is](#)  
6 [orthogonal to y axis, and P3 is orthogonal to z axis. Also shown is the projection of a hexagonal](#)  
7 [prism for three extremes, when its c-axis is parallel to b\) P1, c\) P2, and d\) P3. See text for the](#)  
8 [definition of various symbols.](#)

9 ~~Figure B1. Geometry of hexagonal prism, representative of small ice crystals. See text for the~~  
10 ~~definition of various symbols.~~

11

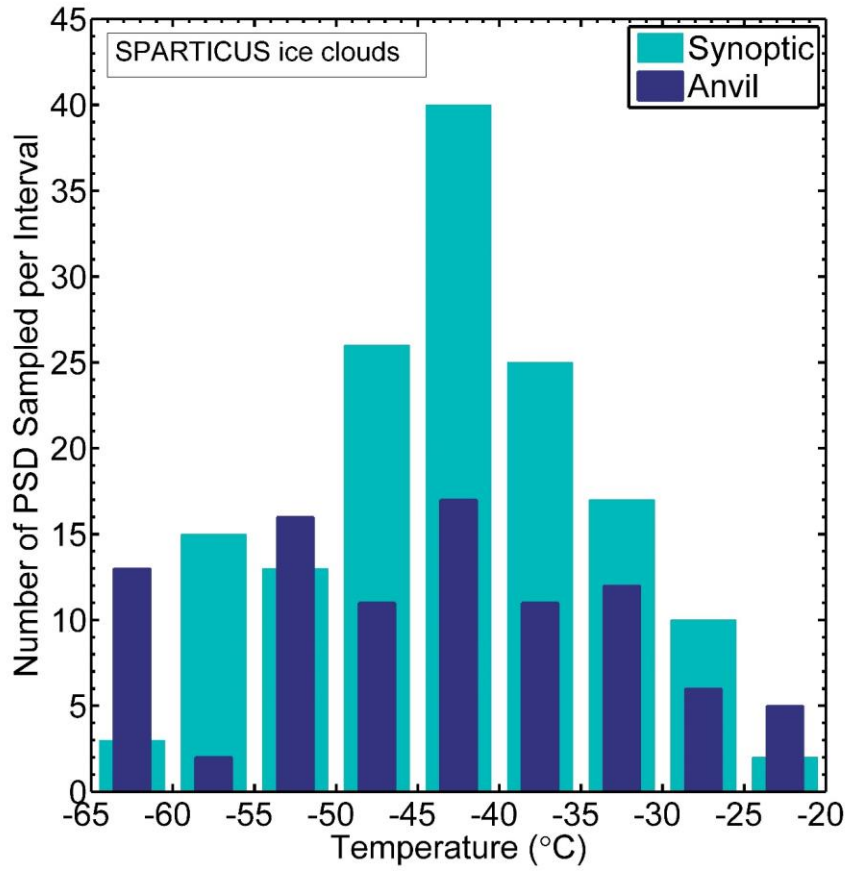
1



2

3 Figure 1. Dependence of ice particle mass ( $m$ ) on ice particle maximum dimension ( $D$ ), based on  
4 a variety of power law relationships in the literature (see text for details). Ice spheres indicate an  
5 upper limit for  $m$  at a given  $D$ . P1b, P1c and P1d denote planar crystals with sectorlike branches,  
6 broad branches and stellar dendrites, respectively, as described in Mitchell (1996).

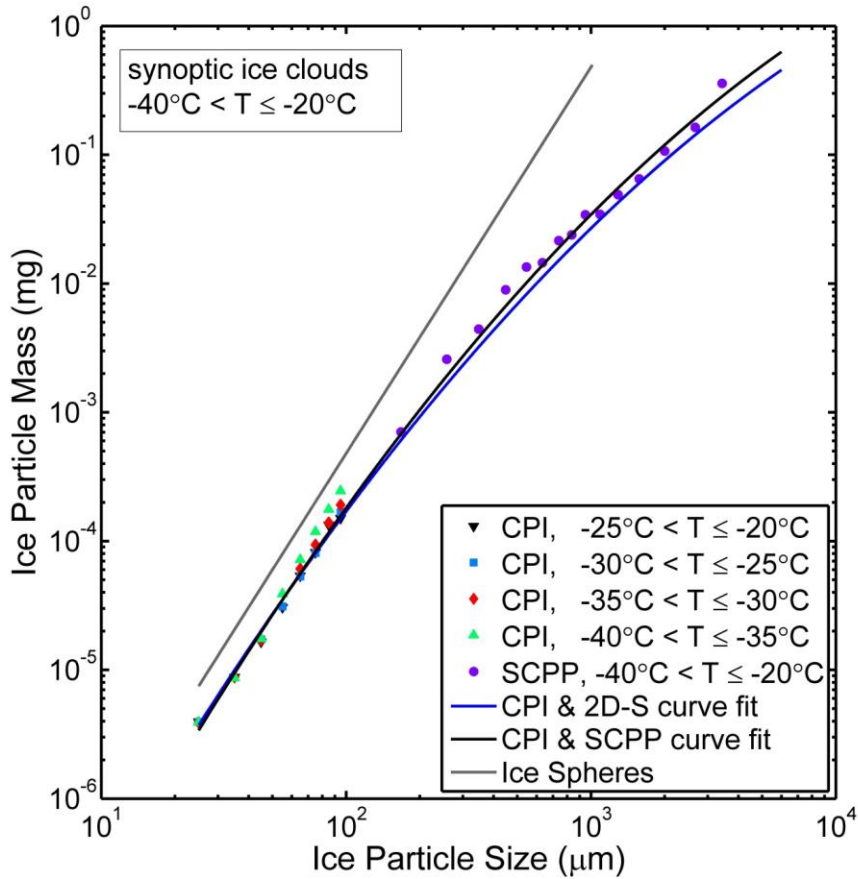
1



2

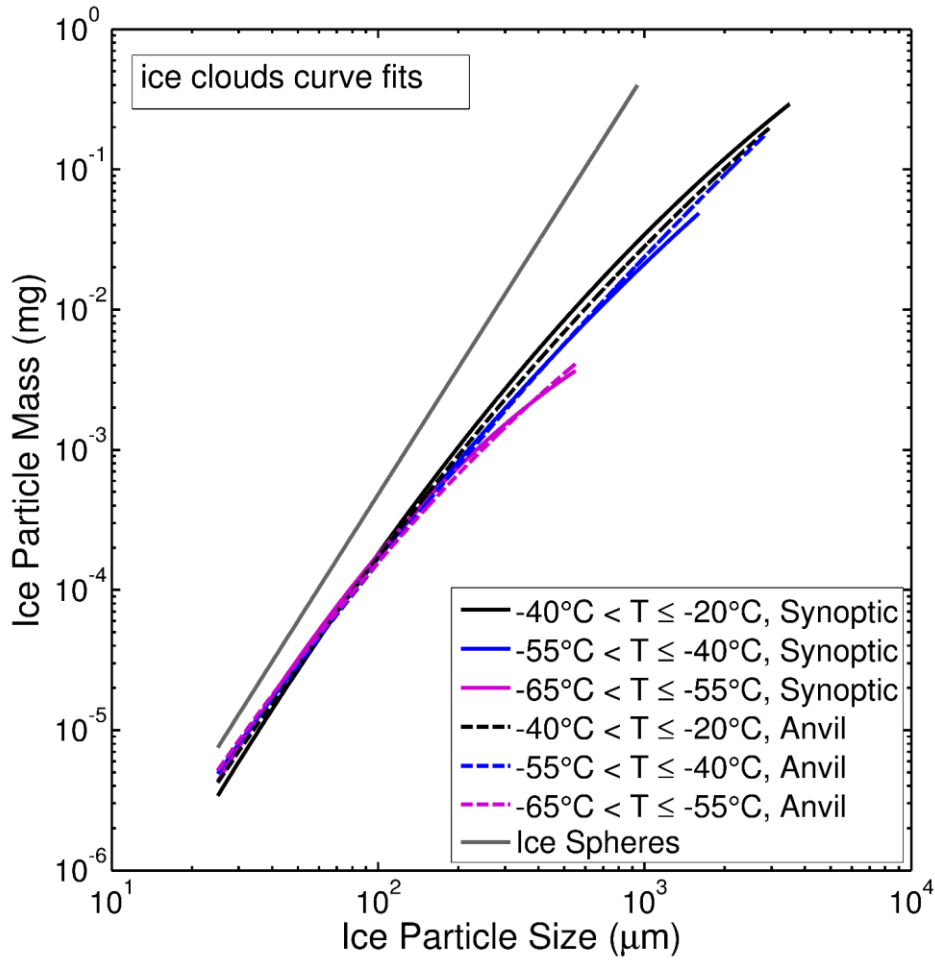
3 Figure 2. SPARTICUS PSD sampling statistics for synoptic and anvil cirrus clouds where the  
4 PSDs have been grouped into temperature intervals of 5 °C.

5



1  
 2 Figure 3. Dependence of ice particle mass on  $D$  for mean PSDs sampled from synoptic cirrus  
 3 clouds during SPARTICUS for  $-40^{\circ}\text{C} < T \leq -20^{\circ}\text{C}$  (blue curve fit based on CPI and 2D-S data),  
 4 where a single mean PSD is the mean of all PSD contained within a  $5^{\circ}\text{C}$  temperature interval.  
 5 Also shown are CPI and SCPP data that are grouped into size-bins for the indicated temperature  
 6 ranges and the black curve fit based on these data (see Table 1 for equation). The grey line for  
 7 ice spheres gives the maximum possible mass for a given  $D$ .

1



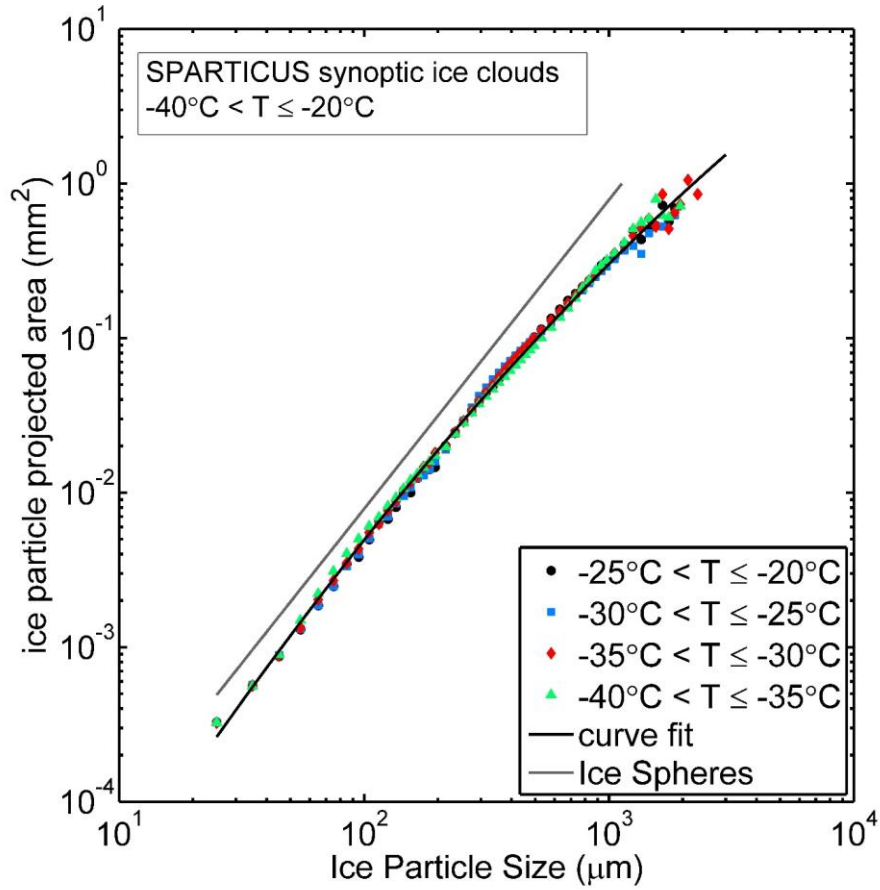
2

3 Figure 4. Comparison of all the curve fits in Table 1 for each temperature regime (indicated by  
4 color) and cloud type (indicated by line type; solid or dashed). The anvil and synoptic curve fits  
5 are very similar.

6



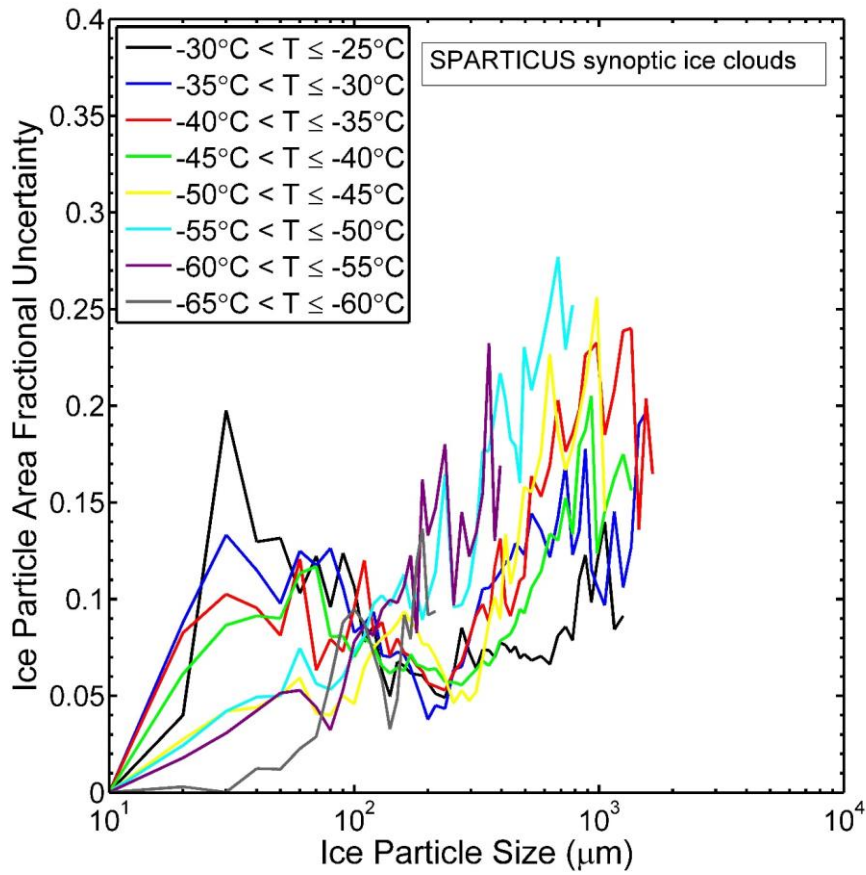
1



2

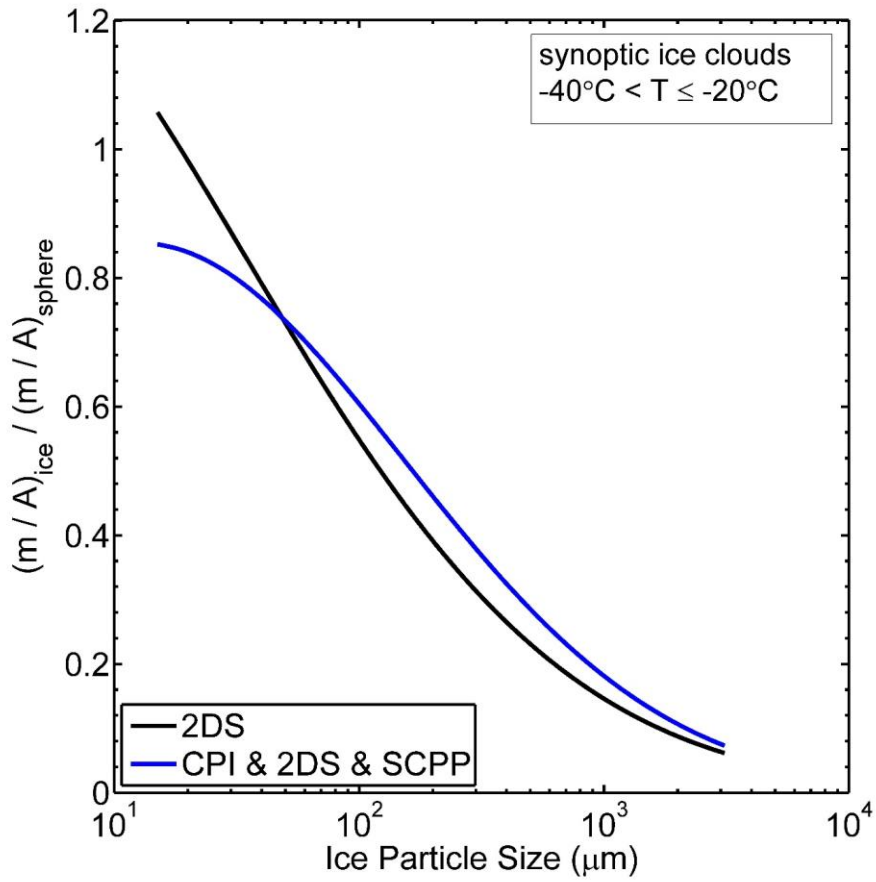
3 Figure 5. Dependence of ice particle projected area ( $A$ ) on  $D$  based on mean PSD within the  
4 indicated temperature regime. The CPI and 2D-S data have been grouped into size-bins, and the  
5 black solid curve is a fit to these datasets (see Table 2 for equation).

6



1  
 2 Figure 6. Fractional uncertainties (standard deviation/mean) for the mean ice particle projected  
 3 area in each bin of the measured PSDs. Only temperature intervals having more than two PSDs  
 4 are considered.

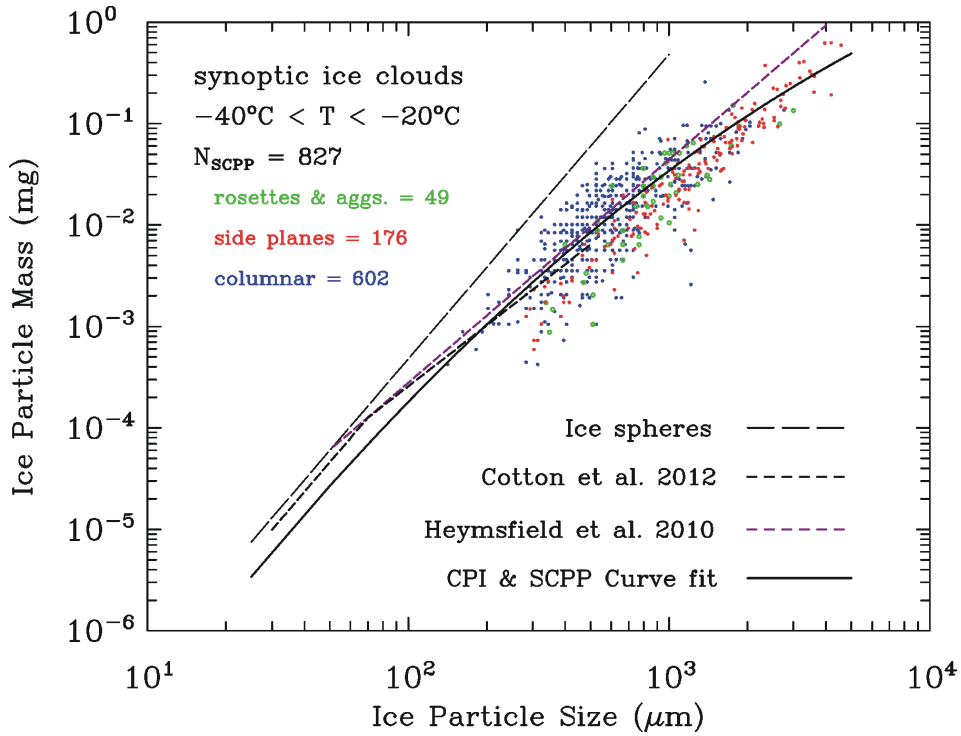
1



2

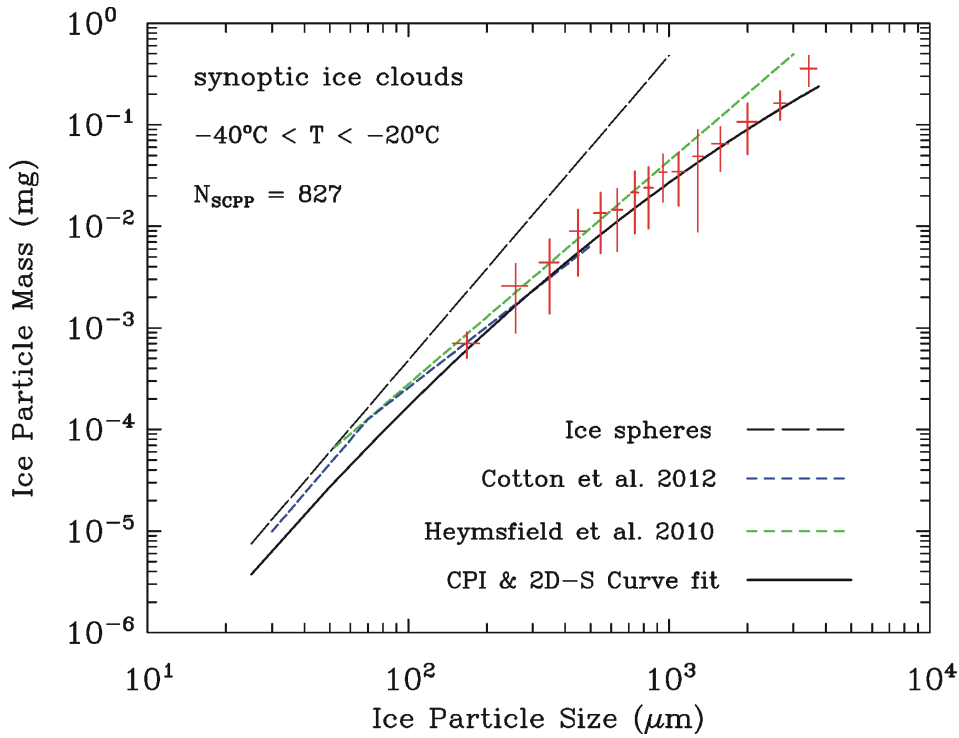
3 Figure 7. The  $m/A$  ratio for ice particles normalized by the corresponding  $m/A$  ratio for ice  
4 spheres using the  $m-D$  and  $A-D$  curve fits appropriate for the indicated temperature regime. Blue  
5 curve is based on Tables 1 and 2, but black curve is only based on 2D-S data.

6



1  
 2 Figure 8. The  $m$ - $D$  curve fit based on SCPP and CPI data (for indicated temperature regime) is  
 3 compared with individual ice particle  $m$ - $D$  measurements from SCPP, corresponding to ice  
 4 particle shapes originating from similar temperatures. The number of ice particles sampled in  
 5 each shape category is indicated. Also shown are comparisons with two other studies that  
 6 derived  $m$ - $D$  power laws from ice cloud field data.

1

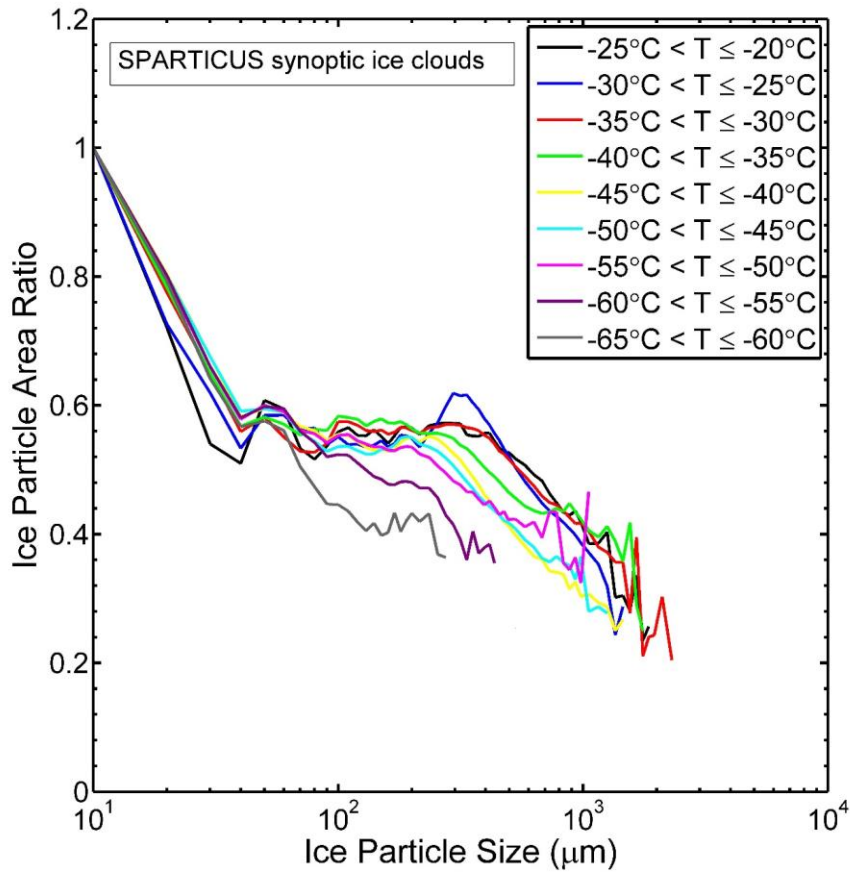


2

3 Figure 9. Same as Fig. 8, except the  $m$ - $D$  curve fit is based on SPARTICUS (2D-S & CPI) data  
4 and the SCPP field data have been grouped into size-bins; shown are the standard deviations ( $\sigma$ )  
5 in  $m$  and  $D$  for each size-bin. Mean values for  $m$  and  $D$  are shown by the intersection of the  $\sigma$ -  
6 bars.

7

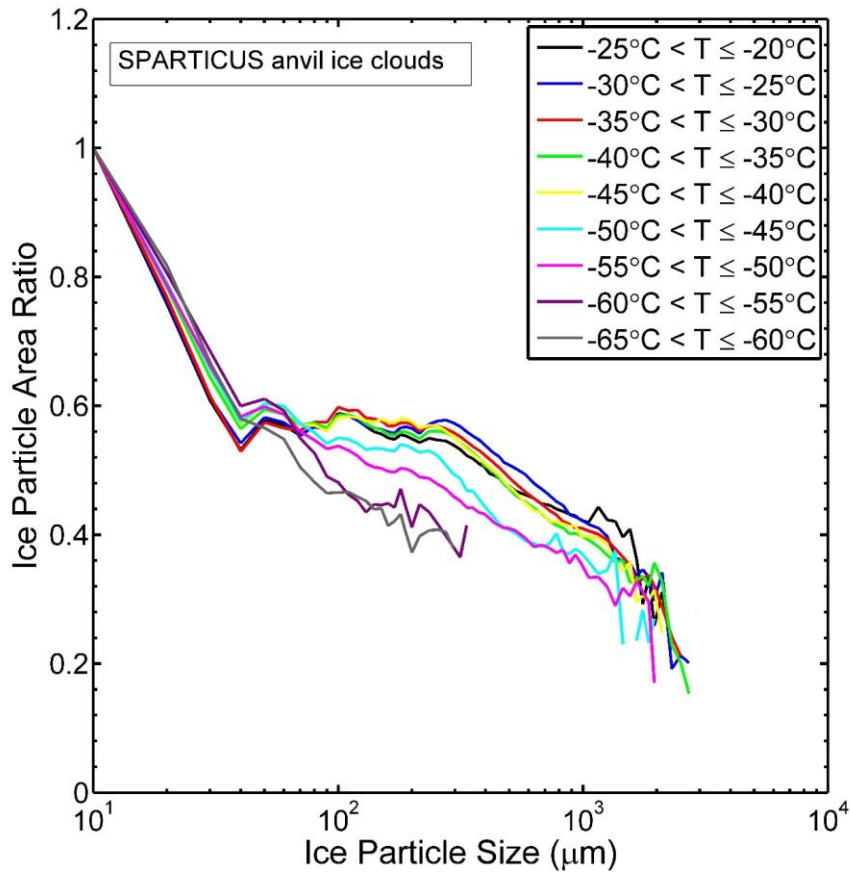
1



2

3 Figure 10. Mean area ratios for each mean PSD size-bin are shown as a proxy for ice particle  
4 shape. Temperature intervals corresponding to each mean PSD are indicated for synoptic ice  
5 clouds.

6

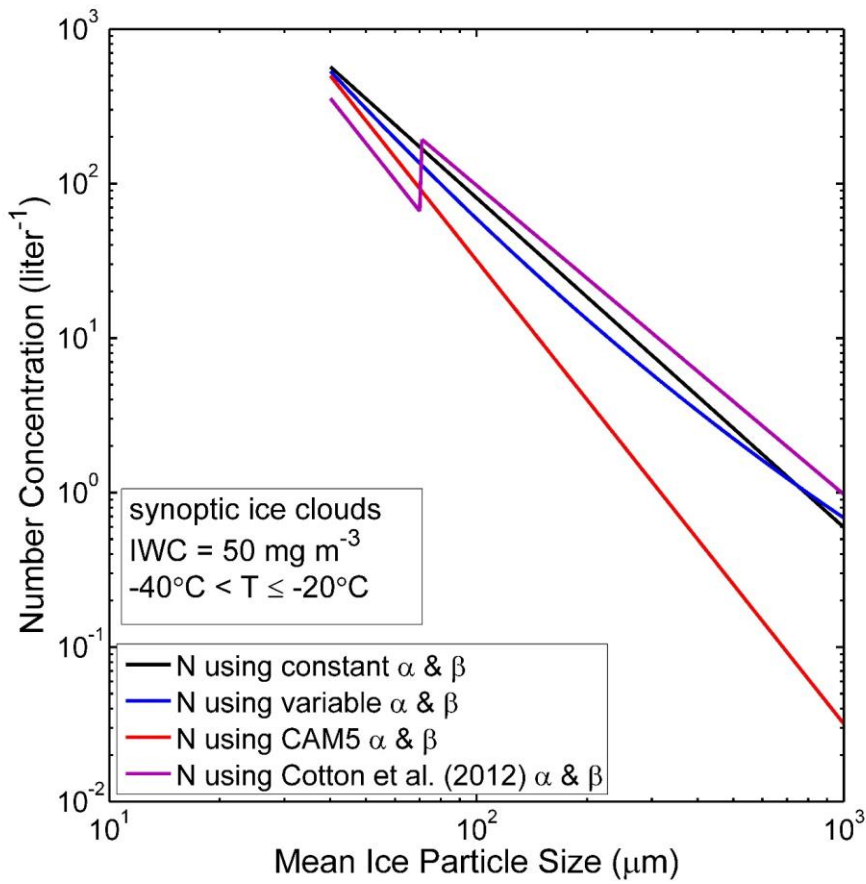


1

2 Figure 11. Same as Fig. 10, but for anvil ice clouds.

3

1



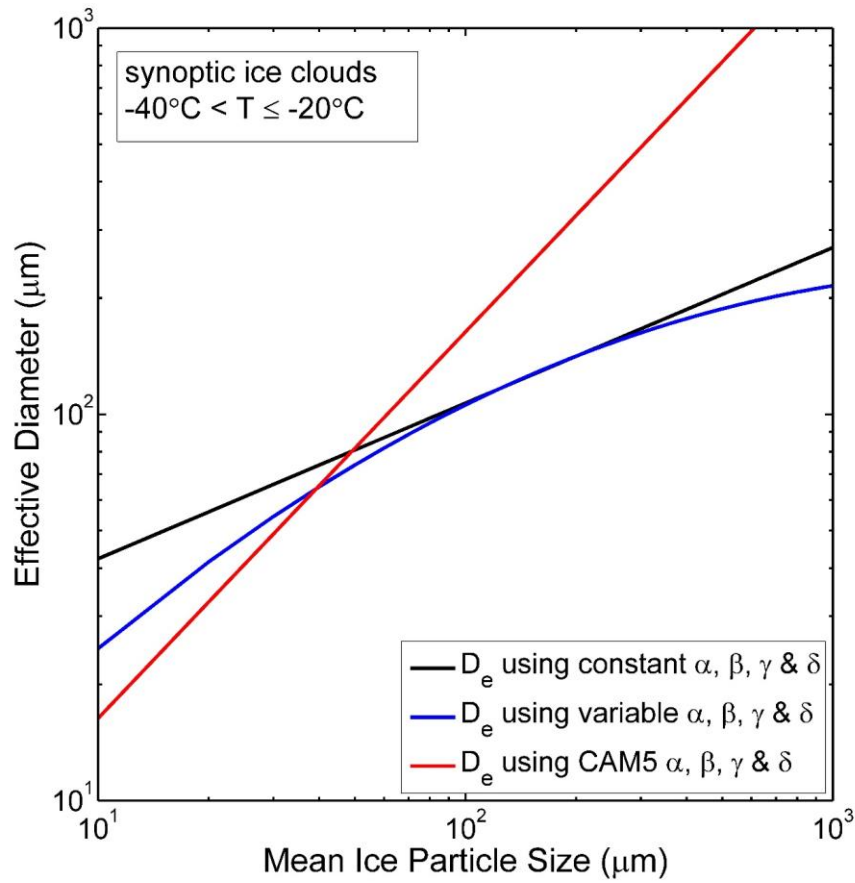
2

3 Figure 12. Dependence of the ice particle  $N$  on  $\bar{D}$  using the 4 methods indicated for determining  
4  $\alpha$  and  $\beta$ . The black and blue curves use the  $m$ - $D$  curve fit based on Table 1 for the indicated  
5 temperature range, with the black curve  $\alpha$  and  $\beta$  evaluated at  $D = 500 \mu\text{m}$ .

6



1

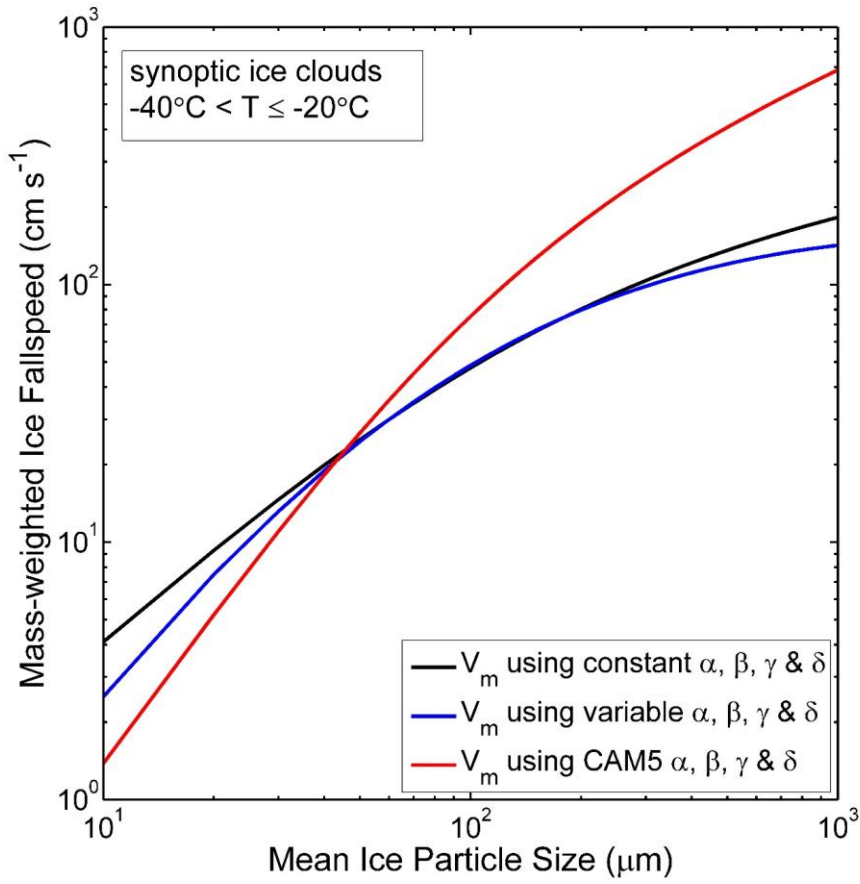


2

3 Figure 13. Dependence of the  $D_e$  on  $\bar{D}$  using the 3 methods indicated for determining  $\alpha, \beta, \gamma$  and  
4  $\delta$ . The black and blue curves use the  $m$ - $D$  curve fit based on Table 1 and  $A$ - $D$  curve fit based on  
5 Table 2 for the indicated temperature range, with the black curve  $\alpha, \beta, \gamma$  and  $\delta$  evaluated at  $D =$   
6  $500 \mu\text{m}$ .

7

1

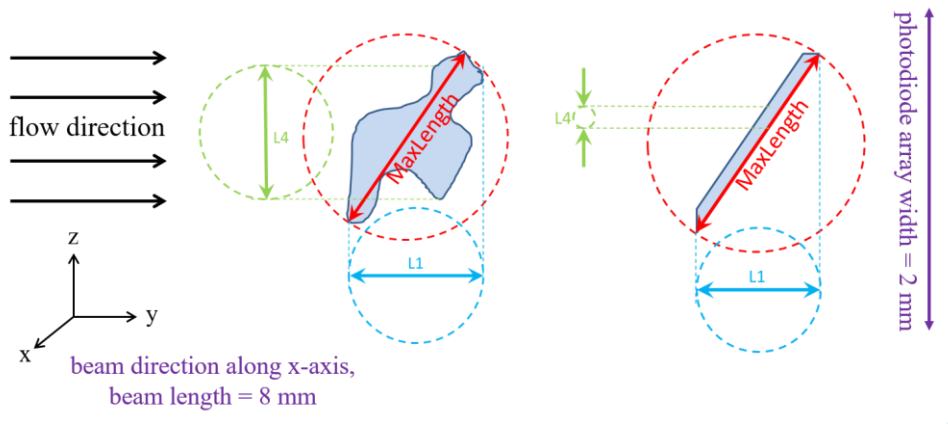


2

3 Figure 14. Same as Fig. 13, but for the dependence of  $V_m$  on  $\bar{D}$ .

4

1



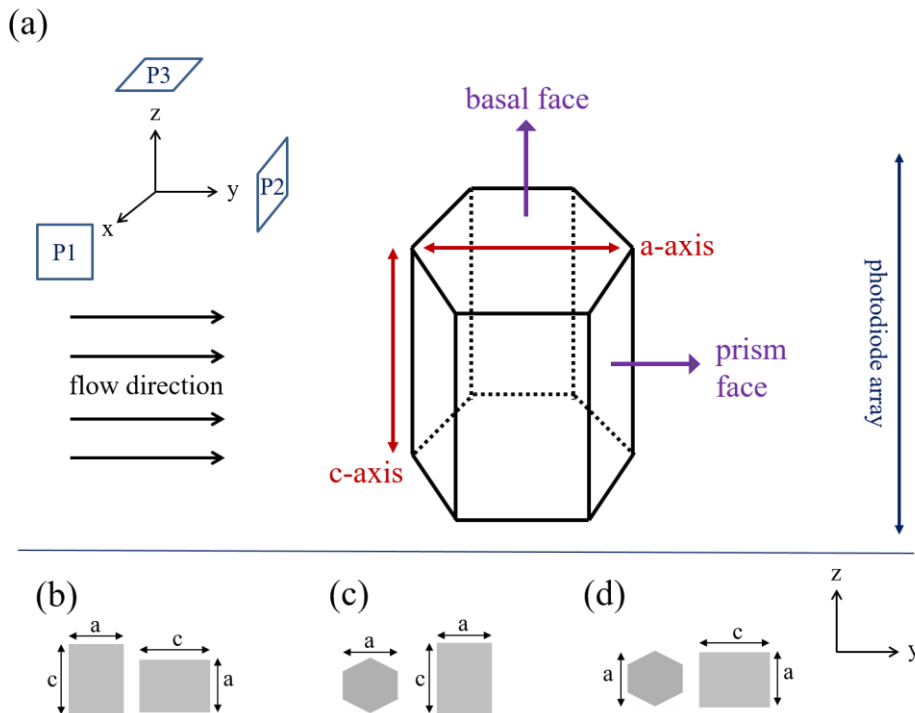
2

3 Figure A1. Geometry of dimension measurements showing length scales for the M1 method ( $L1$ )  
4 and the M7 method (MaxLength) for two ice particles with different shapes. Courtesy of Paul  
5 Lawson and Sara Lance.

Formatted: Font: (Default) Times New Roman, 12 pt, Bold

1

Formatted: Font: 12 pt



Formatted: Font: 12 pt

2

3 Figure B1. a) 3-D geometry of a hexagonal prism, representative of small ice crystals.  
 4 Assuming that the direction of view (beam direction) is along the x axis, P1 is orthogonal to x  
 5 axis, P2 is orthogonal to y axis, and P3 is orthogonal to z axis. Also shown is the projection of a  
 6 hexagonal prism for three extremes, when its c-axis is parallel to b) P1, c) P2, and d) P3. -See  
 7 text for the definition of various symbols.

8